Lagrangian transport evaluation of atmospheric chemistry in the Mediterranean region

Dissertation
zur Erlangung des Grades
"Doktor der Naturwissenschaften"

am Fachbereich Physik der
Johannes Gutenberg-Universität
in Mainz

Michael Andreas Traub

geboren in
Mainz

Mainz, den 02.08.2004

Tag der mündlichen Prüfung: 18.11.2004

Abstract

Global observations of the chemical composition of the atmosphere are essential for understanding and studying the present and future state of the earth's atmosphere. However, by analyzing field experiments the consideration of the atmospheric motion is indispensable, because transport enables different chemical species, with different local natural and anthropogenic sources, to interact chemically and so consequently influences the chemical composition of the atmosphere. The distance over which that transport occurs is highly dependent upon meteorological conditions (e.g., wind speed, precipitation) and the properties of chemical species itself (e.g., solubility, reactivity). This interaction between chemistry and dynamics makes the study of atmospheric chemistry both difficult and challenging, and also demonstrates the relevance of including the atmospheric motions in that context.

In this doctoral thesis the large-scale transport of air over the eastern Mediterranean region during summer 2001, with a focus on August during the Mediterranean Intensive Oxidant Study (MINOS) measurement campaign, was investigated from a lagrangian perspective.

Analysis of back trajectories demonstrated transport of polluted air masses from western and eastern Europe in the boundary layer, from the North Atlantic/North American area in the middle end upper troposphere and additionally from South Asia in the upper troposphere towards the eastern Mediterranean. Investigation of air mass transport near the tropopause indicated enhanced cross-tropopause transport relative to the surrounding area over the eastern Mediterranean region in summer. A large band of air mass transport across the dynamical tropopause develops in June, and is shifted toward higher latitudes in July and August. This shifting is associated with the development and the intensification of the Arabian and South Asian upper-level anticyclones and consequential with areas of maximum clear-air turbulence, hypothesizing quasi-permanent areas with turbulent mixing of tropospheric and stratospheric air during summer over the eastern Mediterranean as a result of large-scale synoptic circulation. In context with the latex knowledge about the transport of polluted air masses towards the Mediterranean and with increasing emissions, especially in developing countries like India, this likely gains in importance.

Zusammenfassung

Globale Beobachtungen der chemischen Zusammensetzung der Atmosphäre sind wichtig für das Verstehen und Untersuchen des Zustandes der Erdatmosphäre in Gegenwart und Zukunft. Bei der Analyse von Feldexperimenten ist es jedoch unabkömmlich, die Luftbewegungen in der Atmosphäre zu berücksichtigen, da der Transport die Wechselwirkung verschiedener chemischer Spezies mit voneinander entfernten natürlichen und anthropogenen Quellen ermöglicht und so die chemische Zusammensetzung der Atmosphäre beeinflußt. Die Transportentfernung ist dabei von den meteorologischen Bedingungen (z.B. Windgeschwindigkeit, Niederschlag) und den Eigenschaften der chemischen Spezies selber (z.B. Löslichkeit, Reaktivität) abhängig. Diese Wechselwirkung zwischen Chemie und Dynamik macht das Studium der Atmosphärenchemie kompliziert, zeigt aber auch die Wichtigkeit der Berücksichtigung der Dynamik in diesem Kontext.
Diese Arbeit befaßt sich mit dem großräumigen Luftmassentransport über dem östlichen Mittelmeer im Sommer 2001, mit besonderem Blick auf den Zeitraum der MINOS Meßkampagne im August, aus lagranger Sichtweise.
Eine Trajektorienanalyse zeigte, daß in der planetaren Grenzschicht verschmutzte Luftmassen aus West- und Osteuropa, in der freien und oberen Troposphäre vom Nord Atlantik und aus Nord Amerika in Richtung der östlichen Mittelmeerregion während des Sommers transportiert wurden. In der oberen Troposphäre wurde zusätzlich noch der Einfluß von Luft aus Südasien festgestellt. Die Untersuchung des Luftmassentransports nahe der Tropopause wies den östlichen Mittelmeerraum im Vergleich zu den umliegenden Gebieten als Region mit erhöhtem Troposphären - Stratosphären Transport während des Sommers aus. So entsteht ein großräumiges Gebiet mit verstärktem Luftmassentransport durch die Tropopause im Juni, und verlagert sich nordwärts im Juli und August. Diese Verschiebung wird mit der Entwicklung und Verstärkung der Arabischen und Südasiatischen Antizyklonen in der oberen Troposphäre und als Folge dessen mit starken Turbulenzen in Verbindung gebracht. Dies führt zur Annahme der Existenz von quasipermanenten Regionen mit turbulenter Mischung von troposphärischer und stratosphärischer Luft in Folge der großräumigen Zirkulation über dem östlichen Mittelmeerraum während des Sommers. Diese Erkenntnis gewinnt im Zusammenhang mit dem Wissen über den Transport verschmutzter Luftmassen in Richtung des Mittelmeerraumes und dem Anstieg der Emissionen, insbesondere in Entwicklungsländern wie Indien, an Bedeutung.

Contents

[1]This chapter is based on: Traub, M., Fischer, H., de Reus, M., Kormann, R., Heland, J., Ziereis, H., Schlager, H., Holzinger, R., Williams, J., Warneke, C., de Gouw, J. and Lelieveld, J. (2003), *Atmos. Chem. Phys.*, Vol.3 :459–468

[2]This chapter is based on: Traub, M. and Lelieveld, J. (2003), *J. Geophys. Res.*, Vol.108, No:D23, 4712, 10.1029/2003JD003754

Chapter 1

Introduction

In recent years atmospheric chemistry has become an important part of the study of the earth's atmosphere. It has become clear that the composition of the atmosphere changes as a result of human activity (*Baede*, 2001). The amount of carbon dioxide, for example, has increased by more than 30% since pre-industrial times and is still increasing at an unprecedented rate of on average 0.4% per year, mainly due to the combustion of fossil fuels and deforestation. The level of methane has more than doubled due to the influence of man, e.g. through agricultural activity and fossil fuel use. Research on the causes and effects of these changes has achieved a prominent role in modern science.

Global observations of the chemical composition of the atmosphere are essential for understanding and studying the present and future state of the earth's atmosphere. However, by analyzing field experiments the consideration of atmospheric motions is indispensable, because transport enables different chemical species, with different local natural and anthropogenic sources, to interact and consequently influence the chemical composition of the atmosphere. The distance over which that transport occurs is highly dependent upon meteorological conditions (e.g., wind speed, precipitation, frontal activity) and the properties of the chemical species itself (e.g., solubility, reactivity). Emissions from Asia, for instance, influence the chemical composition over the northwest Pacific (*Hoell et al.*, 1997) and sources in North America dominate the ozone distribution over the North Atlantic Ocean during the summer (*Parrish et al.*, 1993). This interaction between chemistry and dynamics makes the study of atmospheric chemistry both difficult and challenging, and also demonstrates the relevance of including the atmospheric motions in that context.

Two frameworks are commonly used to describe the dynamical atmospheric behavior, namely the *Eulerian* and the *Lagrangian* perspectives (*Byers*, 1974; *Dutton*, 1986). The *Eulerian* approach focuses on points fixed in space through which the air flows, while in the *Lagrangian* approach the focus is on the individual air parcels as they move in time and space. The path of each air parcel is known as a trajectory. So called "trajectory models", simulating the paths of many virtual air parcels and therefore allowing classification of different air streams, provide a useful tool for describing and analyzing transport of air masses both on global and also on regional scales, and they have been used widely to study dynamical processes in the atmosphere for several decades now. Applications vary from synoptic meteorology, for instance to investigate airmass flows around mountains (*Steinacker*, 1984), to climatology, for instance to identify pathways of desert dust (*Chiapello et al.*, 1997) or water vapor transport (*D'Abreton and Tyson*, 1996), to the environmental sciences, for instance to establish source-receptor relationships of

air pollutants (*Stohl*, 1996). Lagrangian methods can also be used to obtain climatologies of stratosphere-troposphere transport in both a qualitative way by describing spatial distributions of the mass exchange, but also in a quantitative way by estimating mass fluxes crossing the tropopause (*James et al.*, 2003).

This thesis mainly deals with the investigation of air mass transport in August 2001 during the MINOS campaign, with a focus on the eastern Mediterranean based on a lagrangian perspective. In the following chapter the theory and also potential error sources for the calculation of trajectories are given. Chapter 3 comprises a detailed introduction and a definition of the tropopause and also the processes causing air mass transport across that iso-surface. In chapter 4 the investigation of one of the major objectives of the MINOS campaign, the analysis of intercontinental transport of trace species, is presented. For this purpose, calculated backward trajectories were combined with measured trace gas concentrations and analyzed on their origin and their chemical composition. Chapter 5 deals with the increased troposphere-stratosphere transport over the eastern Mediterranean relative to the surrounding area, which is associated with convergence of air transported by the upper-level anticyclone over the Arabian and South Asian heat lows as well as by the Polar Front Jet toward the eastern Mediterranean. In chapter 6 first results of the lagrangian transport scheme ATTILA (*Reithmeier and Sausen*, 2000), being coupled to the chemistry-climate model ECHAM5/MESSy, are presented. In addition to the validation of the accurate coupling to ECHAM5/MESSy by simulation of a Warm Conveyor Belt over the Atlantic Ocean and the determination of the average travel time from the Asian boundary layer to the upper-level Mediterranean area, sensitivity studies on the transport characteristics at synoptic-scale by changing the horizontal resolution of ECHAM5/MESSy are shown. Furthermore in addition to the qualitative investigation of the cross-tropopause transport over the eastern Mediterranean presented in chapter 5, a quantitative analysis by calculation of mass fluxes for May to August 2001 with ATTILA is presented in chapter 7. In the final chapter the main results of this thesis are summarized and an outlook is given.

Chapter 2

Trajectory calculations

Two frameworks are commonly used to describe the dynamical behaviour of atmospheric parcels; namely the *Eulerian* and the *Lagrangian* perspectives (*Byers*, 1974; *Dutton*, 1986). The *Eulerian* approach focuses on locations fixed in space through which the air flows, while in the *Lagrangian* approach the focus is on the individual air parcels as they move in time and space. The path of each air parcel is known as a trajectory. This chapter addresses the theory and the computational background of trajectory calculations and additionally summarizes error sources.

2.1 Trajectory equation

The trajectory of an infinitesimally small air parcel is defined by the differential trajectory equation

$$\frac{d\mathbf{X}}{dt} = \dot{\mathbf{X}}[\mathbf{X}(t)] \tag{2.1}$$

with t being time, $\mathbf{X}$ the position vector and $\dot{\mathbf{X}}$ the wind velocity vector. If the initial position $\mathbf{X}_0$ at time t_0 of the parcel is known, its path is completely determined through equation (2.1). Therefore

$$\mathbf{X}(t) = \mathbf{X}(\mathbf{X}_0, t) \tag{2.2}$$

The inverse transformation giving the initial coordinates of the parcel, which at time t is at position $\mathbf{X}$, is

$$\mathbf{X}_0(t = t_0) = \mathbf{X}_0(\mathbf{X}, t) \tag{2.3}$$

Thus, air parcels may be followed either forward (i.e. *forward trajectories*) or backward (i.e. *backward trajectories*) in time. The spatial coordinates $\mathbf{X}_0$ at time t_0 provide a means of identifying each air parcel during subsequent time periods. These initial coordinates are called *material* or *Lagrangian coordinates* (*Dutton*, 1986).

The idealized concept discussed above is not fully applicable in the real atmosphere. With the limited information available, it is not possible to select an infinitesimal air parcel and follow its path with infinite accuracy. Real air parcels are being deformed by inhomogeneities of the wind, by convective and turbulent motions and by precipitation processes. Owing to the combination of these processes one single trajectory is not sufficient to represent the path of an air

parcel (*Pflügler et al.*, 1990). Hence, a computed trajectory is representative for the path of an air parcel only for a limited period.
Equation (2.1) can be solved analytically only for simple flow fields. For meteorological applications, a finite-difference approximation of equation (2.1) must be used (*Walmsley and Mailhot*, 1983). Expanding $\mathbf{X}(t)$ in a Taylor series about t = t_0 and evaluating at $t_1 = t_0 + \Delta t$, one obtains

$$\mathbf{X}(t_1) = \mathbf{X}(t_0) + (\Delta t)\frac{d\mathbf{X}}{dt}|_{t_0} + \frac{1}{2}(\Delta t)^2\frac{d^2\mathbf{X}}{dt^2}|_{t_0} + ... \tag{2.4}$$

The first approximation of equation (2.4) is

$$\mathbf{X}(t_1)\approx\mathbf{X}(t_0) + \Delta(t)\dot{\mathbf{X}}(t_0) \tag{2.5}$$

a *zero acceleration* of equation (2.4) that is computationally cheap since it involves no iteration. It is accurate to the first order, which means that the difference between the real and the numerical solution follows from the omission of the second- and higher-order terms. If trajectories are calculated using very short integration time steps, equation (2.5) might be of sufficient accuracy. However, more accurate approximations at acceptable computational costs exist. Expanding $\mathbf{X}(t)$ in a Taylor series about t=t_1 and evaluating at t=t_0, one obtains

$$\mathbf{X}(t_0) = \mathbf{X}(t_1) - (\Delta t)\frac{d\mathbf{X}}{dt}|_{t_1} + \frac{1}{2}(\Delta t)^2\frac{d^2\mathbf{X}}{dt^2}|_{t_1} - ... \tag{2.6}$$

Combining equations (2.5) and (2.6), we can write

$$\mathbf{X}(t_1) = \mathbf{X}(t_0) + \frac{1}{2}(\Delta t)[\dot{\mathbf{X}}(t_0) + \dot{\mathbf{X}}(t_1)] + \frac{1}{4}(\Delta t)^2[\frac{d\dot{\mathbf{X}}}{dt}|_{t_0} - \frac{d\dot{\mathbf{X}}}{dt}|_{t_1}] + ... \tag{2.7}$$

If only the first two terms on the right-hand side of (2.7) are retained, the *constant acceleration solution*

$$\mathbf{X}(t_1) \approx \mathbf{X}(t_0) + \frac{1}{2}(\Delta t)[\dot{\mathbf{X}}(t_0) + \dot{\mathbf{X}}(t_1)] \tag{2.8}$$

results (*Walmsley and Mailhot*, 1983). This approximation is known as Petterssen's scheme (*Petterssen*, 1940). Equation (2.8) is accurate to the second order. It has to be solved by iteration starting with equation (2.5), since $\dot{\mathbf{X}}(t_1)$ is not a priori known.

$$\begin{aligned}
\mathbf{X}^1(t_1) &\approx \mathbf{X}(t_0) + (\Delta t)\dot{\mathbf{X}}(t_0) \\
\mathbf{X}^2(t_1) &\approx \mathbf{X}(t_0) + \frac{1}{2}(\Delta t)[\dot{\mathbf{X}}(t_0) + \dot{\mathbf{X}}^1(t_1)] \\
&\vdots \\
\mathbf{X}^i(t_1) &\approx \mathbf{X}(t_0) + \frac{1}{2}(\Delta t)[\dot{\mathbf{X}}(t_0) + \dot{\mathbf{X}}^{i-1}(t_1)]
\end{aligned} \tag{2.9}$$

The superscripts indicate the number of iterations, and $\dot{\mathbf{X}}^i(t_1)$ is taken at position $\mathbf{X}^i(t_1)$.
Sometimes the third term on the right-hand side of equation (2.7) is retained, too (*variable acceleration method*). In principle, this solution gives higher accuracy at the cost of increased computing time, but it has the disadvantage that the accelerations at two times must be evaluated. This can be inaccurate because wind fields are often available only at large temporal intervals. Hence, the variable acceleration method may even be less accurate than the constant acceleration method. If linear interpolation of the wind is used, the third term on the right-hand side of equation (2.7) vanishes, and the variable acceleration method reduces to the constant acceleration method.

2.2 Error sources

Various steps in the trajectory calculations can produce errors, which can lead to misinterpretations of flow situations. Trajectory errors are caused by truncation errors which occur in the numerical solution of the trajectory equation (*Walmsley and Mailhot*, 1983; *Seibert*, 1993), when equation (2.1) is approximated by a finite-difference scheme that neglects the higher order terms of the Taylor series.
But also the underlying wind fields can be a source of inaccuracies. Wind field errors can be due to either analysis errors or forecast errors, depending on the type of wind fields used (*Stohl*, 1998a). Trajectory errors caused by erroneous forecasts are relatively straightforward to evaluate by comparing forecasts with analysis trajectories. But also the temporal and the spatial resolution of the underlying wind fields and the associated interpolation in time and space is a significant error source for trajectory computations (*Stohl et al.*, 1995). The growth of trajectory position errors with travel time caused by interpolation is approximately linear. However, an increase in spatial resolution alone only marginally improves the accuracy of trajectories when the temporal resolution is low. On the other hand, increasing the temporal resolution alone is not very effective when the spatial resolution is low (*Kuo et al.*, 1985; *Doty and Perkey*, 1993; *Rolph and Draxler*, 1990; *Stohl et al.*, 1995). In any case, a minimum resolution of 6 hours is necessary if any diurnal variations in the flow field are to be resolved (*Stohl*, 1998a).
A further source of accuracies is convective motion. While, for instance, the European Centre for Medium-Range Weather Forecasts (ECMWF) data reproduce large-scale effects of convection (e.g., strong ascent in the Intertropical Convergence Zone or within Warm Conveyor Belts), smaller scale convective cells are not resolved (*Stohl et al.*, 2002).
Trajectory errors are also related to different assumptions regarding the vertical wind component w. In contrast to the horizontal wind, there are no routine observations of w. Fields of w are a sole product of meteorological models, and hence are less accurate than the fields of the horizontal wind. Since w is balanced by the vertically integrated horizontal wind divergence, this leads to large uncertainty of w at low latitudes, mainly caused by difficulties in the parameterization of cumulus convection, which is also significant at higher latitudes during summer (*Stohl*, 1998a). Nevertheless, if accurate fields of w are available, three-dimensional trajectories are more accurate than isobaric or isentropic trajectories (*Stohl and Seibert*, 1998b).
Inaccurate knowledge of the starting position (*Merril et al.*, 1985) can cause additional inaccuracies. Although the initial trajectory position error may be rather small, it can strongly amplify in divergent (forward trajectories) or convergent (backward trajectories) flow. Determination of

air mass origin by the analysis of only one trajectory is therefore highly uncertain. A widely used possibility for assessing trajectory uncertainty is the ensemble method (*Merril et al.*, 1985; *Seibert*, 1993): the calculation and analysis of an ensemble of trajectories with slightly different initial positions gives a reliable estimation of the sensitivity of the trajectories to initial conditions and errors.

A survey of results from previous studies employing different techniques suggests that average trajectory errors are of the order of about 20 % of the traveled distance over a few days (*Stohl*, 1998a).

Nevertheless, backward trajectory analysis has become a widely used method for interpretation of trace gas measurements in relation to large scale air mass transports (e.g., *Moody et al.*, 1995).

Chapter 3

Tropopause definition and cross-tropopause transport

The troposphere and stratosphere have several fundamentally different properties, e.g. the static stability and chemical composition. Therefore, transport of air from the stratosphere to the troposphere and in the opposite direction plays an important role in both the dynamics and composition of the atmosphere. Of special significance is the transport of chemical trace species, natural and anthropogenic, between these two regions. For instance, anthropogenic halocarbons transported from the troposphere to the stratosphere initiate much of the chemistry responsible for stratospheric ozone depletion (*WMO*, 1995). In addition, chemical effects from cross-tropopause transport can influence the radiative flux balance in the troposphere and lower stratosphere (*Ramaswamy et al.*, 1992; *Toumi et al.*, 1994) and can therefore play a significant role in the radiative forcing that causes global climate change (*Holton et al.*, 1995).

A main focus of this thesis is the transport of air from the stratosphere to the troposphere and vice versa. Even though only one single criterion to distinguish between stratospheric and tropospheric air is used through this study, a detailed introduction and the different definitions of the tropopause, the "boundary" between the stratosphere and the troposphere, and also the processes causing air mass transport across that iso-surface are presented in this chapter.

3.1 Thermal tropopause

The simplest criterion to distinguish between the stratosphere and the troposphere is the so-called *thermal tropopause* criterion by the *WMO* (1957), based on a first underestimate of the vertical stratification. The thermal tropopause is taken to be the lowest level at which the temperature gradient ($\frac{\partial T}{\partial z}$) exceeds -2 K k$m^{-1}$, provided that the average ($\frac{\partial T}{\partial z}$) between this level and all higher levels within 2 km does not fall below this value.

3.2 Dynamical tropopause

Another widely used criterion, first proposed by *Reed* (1955), is based on the Potential Vorticity (PV), also accounting for dynamical properties of the atmosphere. The PV is defined as the

absolute vorticity of an air parcel, ζ_θ + f, times its thermal stability, $\frac{\delta\theta}{\delta p}$, i.e.,

$$PV = -g(\zeta_\theta + f)\frac{\delta\theta}{\delta p} \tag{3.1}$$

with ζ_θ the relative isentropic vorticity, f the Coriolis parameter, both in units of s^{-1}, θ the potential temperature in K, g the gravitational acceleration in ms^{-2} and p the pressure in Pa. If one neglects the effects from diabatic and turbulent mixing processes, the potential vorticity of an air parcel is conserved along its three-dimensional trajectory. Within the troposphere, the PV is usually low. However, the PV increases rapidly from the troposphere to the stratosphere due to the significant change of the static stability. While the *WMO* (1986) defines the so-called *dynamical tropopause* by the 1.6 PVU (Potential Vorticity Units = 10^{-6} m^2 s^{-1} K kg^{-1}) iso-surface, *Hoerling et al.* (1991) point out that 3.5 PVU represents an optimal value for the definition of the tropopause outside the tropics. In the tropics, the PV criterion is inappropriate to distinguish between the troposphere and the stratosphere.

It should be noted that because of the difference between stratospheric and tropospheric PV, potential vorticity generation and destruction processes (e.g., *Wirth*, 1995*b*) are essential for the exchange of air and its chemical constituents between the stratosphere and troposphere.

3.3 Overworld, middleworld and underworld

An additional classification to distinguish between troposphere and stratosphere is given by *Holton et al.* (1995). Stratosphere and troposphere are subdivided into the overworld, the middleworld and the underworld (Figure 3.1). The overworld is the part of the stratosphere where isentropic surfaces lie entirely within the stratosphere, while in the underworld all isentropic surfaces lie within the troposphere. In the middleworld isentropic surfaces lie partly in the stratosphere and partly in the troposphere. The stratospheric part of the middleworld is called the lowermost stratosphere. The lower boundary of the overworld coincides approximately with the 380 K isentropic surface. Air in the overworld cannot reach the troposphere without descending across isentropic surfaces, a process that must be accompanied by adiabatic cooling, which takes place on a time scale of the order of months. Air in the underworld cannot reach the stratosphere without rising across isentropic surfaces, a process that takes place on a time scale ranging from hours to days. In the middleworld, air can be transported from the troposphere to the lowermost stratosphere and in the opposite direction by transport along isentropic surfaces.
While transport from the overworld to the lowermost stratosphere, depending on global-scale dynamical aspects, defines the total amount of air and tracers that will be exchanged, transport from the lowermost stratosphere to the troposphere requires consideration of the details of processes at the tropopause and defines the temporal and spatial distribution of the mass exchange.

3.4 Dynamical aspects of the air mass transport

The circulation in the upper troposphere and the stratosphere, known as Brewer-Dobson circulation, can be described by upward motion to the tropical stratosphere and poleward transport with a downward mass flux from the stratosphere to the troposphere in middle and high lati-

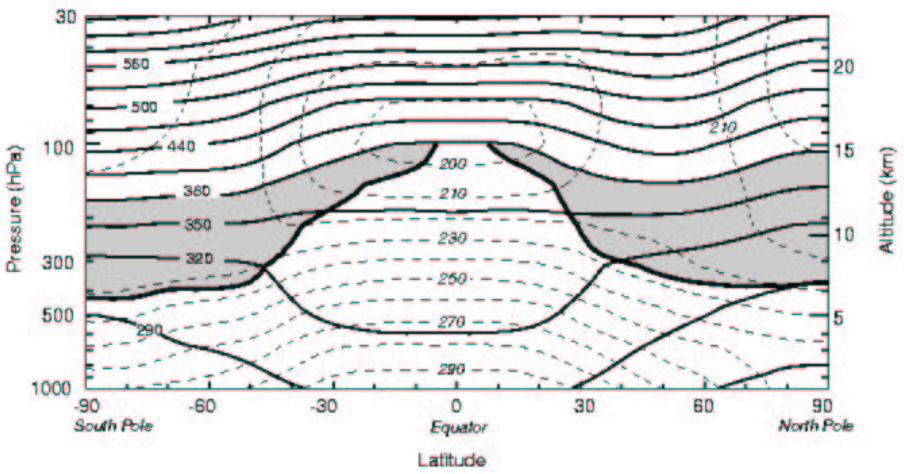

Figure 3.1: Latitude-altitude cross section for January 1993 showing longitudinally averaged potential temperature (solid contours) and temperature (dashed contours). The heavy solid contour (cutoff at the 380 K isentrope) denotes the 2 PVU potential vorticity contour, which approximates the tropopause outside the tropics. Shaded areas denote the lowermost stratosphere whose potential temperature surfaces span the tropopause [from *Holton et al.* (1995)].

tudes. As described in *Holton et al.* (1995), this circulation is driven by westward moving Rossby and gravity waves breaking in the extra-tropical middle atmosphere. This breaking induces a persistent drag, which can be seen as a force that decelerates air parcels towards the east. In the extratropics this force destroys the balance between the poleward pressure gradient force and the equator-ward Coriolis force, because the Coriolis force decreases accordingly to the slower moving air parcels. The air parcels will therefore be forced poleward. Because of mass conservation this poleward movement, acting as a "suction pump" on air in the tropics, causes upward motion in the tropics and downward transport in the extratropics and the polar regions.

The global scale circulation is the process that determines the total amount of air that is exchanged between the stratosphere and the troposphere. On long enough time scales fluxes across the 380 K surface and the tropopause must be the same, assuming that there is no source or sink in the lowermost stratosphere, while there is no uniformity of the fluxes at short time scales, because of the seasonal variability of the mass of the extra-tropical lowermost stratosphere (*Appenzeller et al.*, 1996b) and the dependence of local exchange across the tropopause on the temporal and spatial distribution of processes like tropopause folds.

3.5 Processes near the tropopause

There are several processes causing air mass transport from the stratosphere to the troposphere and in the opposite direction. These processes are responsible for the temporal and spatial distribution of the mass transport.

The pumping action of the Brewer-Dobson circulation causes large-scale upward transport

from the tropical troposphere to the tropical stratosphere, at a rate that is largely independent of local conditions near the tropical tropopause (*Meloen*, 2002). This pumping promotes the formation of deep cumulonimbus clouds and produces higher and colder tropopauses. Air from the lower troposphere is injected into the upper troposphere by the cumulonimbus clouds and from there slowly ascends into the tropical tropopause (*Folkins et al.*, 1999; *Lamarque and Hess*, 1994).

The mass of the lowermost stratosphere has a seasonal cycle. *Appenzeller et al.* (1996b) found that the net mass variation of the lowermost stratosphere substantially contributes to the net mass flux across the tropopause. This mass flux in the northern hemisphere has a maximum in late spring and a distinct minimum in autumn. For the southern hemisphere the seasonal cycle of the net mass transport is weaker. Measurements of tracers near the tropopause confirm this result.

As the isentropes intersect the tropopause in the extratropics, transport across the tropopause can occur in both directions (*Chen*, 1995) and plays a critical role in transporting and mixing trace constituents between the stratosphere and the troposphere. Observational studies have shown that air masses, water vapor and chemical species are transported bidirectionally along isentropic surfaces crossing the subtropical or midlatitudal tropopause (e.g., *Appenzeller et al.*, 1996b; *Lelieveld et al.*, 1997). This transport is assumed to be much faster than the meridional diabatic circulation (*Holton et al.*, 1995).

Transport of air from the stratosphere to the troposphere across the extratropical tropopause has been observed to occur with tropopause folds at both the Polar Front Jet (*Danielsen*, 1968; *Vaughan*, 1988; *Lamarque and Hess*, 1994; *Vaughan and Timmis*, 1994; *Langford et al.*, 1996) and at the Subtropical Jet (*Baray et al.*, 2000; *Kowol-Santen and Ancellet*, 2000).

Midlatitude transport from the troposphere to the stratosphere has been observed less frequently than in the opposite direction. Nevertheless, the existence of relatively moist layers containing tracers that unambiguously were transported from the Earth's surface to the lowermost stratosphere can be seen as evidence for the occurrence of such processes (*Ray et al.*, 1999). Aircraft measurements suggest that extratropical troposphere to stratosphere transport occurs in shear zones pole ward of the Subtropical (*Hintsa and et al.*, 1998) and Subpolar Jet stream (*Fischer et al.*, 2000; *Zahn and et al.*, 2000). The idealized study of *Zierl and Wirth* (1997) considered the radiative effects on moist anomalies below an elevated tropopause and found significant transport from the troposphere to the stratosphere. *Stohl* (2001) and *Wernli and Bourqui* (2002) emphasized the role of Warm Conveyor Belts for transport of tropospheric air to the stratosphere.

Cut-off lows, being created by equator-ward extrusions of stratospheric air on isentropic surfaces, being isolated from the stratospheric reservoir, are characterized by a low tropopause and a reduction of the tropospheric stability and are also a cause of cross-tropopause transport (*Bamber et al.*, 1984; *Price and Vaughan*, 1993; *Wirth*, 1995*b*). Tropopause folds and cut-off lows are especially important, because they are associated with large latitudinal displacements of the tropopause on isentropic surfaces, which facilitate the transport of large amounts of air (*Stohl et al.*, 2003).

Shapiro (1976, 1978) presented evidence for clear-air turbulence at jet stream levels as a first-order process in modifying potential vorticity, thus permitting air parcel exchange across the tropopause. *Bertin et al.* (2001), observing a tropopause folding by a network of radars and lidars, concluded that mixing processes between stratospheric and tropospheric air masses are closely associated with wind shear generated at the jet stream.

Chapter 4

Chemical characteristics assigned to trajectory clusters during the MINOS campaign[1]

Abstract

During the Mediterranean Intensive Oxidant Study in August 2001 a total of 14 measurement flights were performed with the DLR Falcon aircraft from Heraklion, Crete. A major objective of this campaign was the investigation of the role of long-range transport of pollutants into the Mediterranean area. An analysis of 5-day back trajectories indicates that in the lower troposphere (0 - 4 km) air masses originated from eastern and western Europe, in the mid-troposphere (4 - 8 km) from the North Atlantic Ocean region and in the upper troposphere (8 - 14 km) from North Atlantic Ocean /North America (NAONA) as well as South Asia. All back trajectories were allocated to clusters based on their ending height and source region. The mixing ratios of ozone, nitrogen oxide, total reactive oxidized nitrogen (NO_y), formaldehyde, methanol, acetonitrile, acetone, peroxyacetyl nitrate (PAN), carbon dioxide, carbon monoxide and methane measured along the flight tracks are examined in relation to the different cluster trajectories. In the lower troposphere the mean trace gas mixing ratios of the eastern Europe cluster trajectories were significantly higher than those from western Europe. In the upper troposphere relatively high concentrations of O_3 and NO_y, combined with low CO of the NAONA trajectories indicate mixing with stratospheric air masses.

4.1 Introduction

A large number of chemical measurements was made on the DLR Falcon aircraft during the Mediterranean Intensive Oxidant Study (MINOS) flights in August 2001. The flight tracks of this experiment are shown in Figure 4.1. The measurements were designed to explore the role of long-range transport of pollutants into the Mediterranean basin. As a result of the regional meteorological conditions (cloud-free, high temperatures and intense solar radiation),

[1]This chapter is based on: Traub, M., Fischer, H., de Reus, M., Kormann, R., Heland, J., Ziereis, H., Schlager, H., Holzinger, R., Williams, J., Warneke, C., de Gouw, J. and Lelieveld, J. (2003), *Atmos. Chem. Phys.*, Vol.3 :459–468

photochemistry can be very active (*Kouvarakis et al.*, 2000), and the area is sensitive to air pollution. An overview is given by *Lelieveld et al.* (2002)
Backward trajectory analysis has become a widely used method for interpretation of trace gas measurements in relation to large scale air mass transport (*Moody et al.*, 1995). The trajectories can be categorized into particular clusters to characterize different types of air masses. In most cases, the origin of the air masses and their transport routes have been used as the main criteria for clustering. By assuming that the chemical composition changes at the same rate along all transport paths, the variability in the measured trace gas concentrations can be explained in terms of the trajectory origin and emission influences along the route (*Pochanart et al.*, 2001).
It should be mentioned, however, that the implicit assumption that the trajectories accurately represent transport pathways may sometimes be incorrect. As already mentioned in section 2.2, there are many uncertainties involved in the measurements of the meteorological conditions, the generation of reanalysis data with help of the observed parameters and assimilation methods, the interpolation of the wind in time and space, and also the representation of small-scale effects (e.g. convection) in the meteorological data. Nevertheless, trajectories provide a useful tool to characterize patterns in the large-scale atmospheric motion.

After a short overview of the measurement technique on board the Falcon in section 4.2, a general overview of the large-scale circulation over the Mediterranean area is presented in section 4.3. Section 4.4 subsequently describes the model used and the setup for analysis of trajectory clusters, while section 4.5 presents the three-dimensional trajectory analysis and the chemical characteristics of the different trajectory clusters. Section 4.6 concludes by summarizing the relative importance of different source regions.

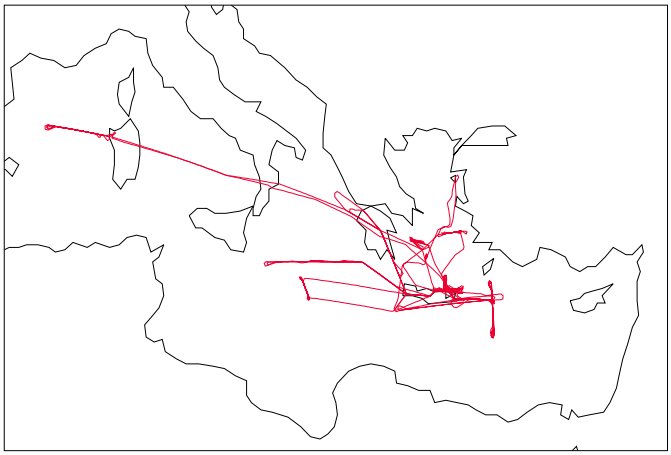

Figure 4.1: Flight tracks of the DLR Falcon aircraft over the central and eastern Mediterranean Sea during MINOS in August 2001.

4.2 Measurement techniques

CO, CO_2 , CH_4 , CH_3OH , CH_3COCH_3 , CH_3CN , PAN and HCHO were measured by the Max Planck Institute for Chemistry, Mainz, Germany.

For CO, CO_2 and CH_4 a Tunable Diode Laser Absorption Spectrometer (TDLAS), with a time resolution of 6 s, was used. The precision was 1.5 ppm for CO_2, 1.5 ppbv for CO and 16.5 ppb for CH_4 and the average accuracy was 1% for all species. A detailed description of the instrument can be found in *Wienhold et al.* (1998).
The mixing ratios of CH_3OH , CH_3CN , CH_3COCH_3 and PAN were measured using proton-transfer reaction mass spectrometry (PTR-MS). The accuracy for CH_3OH was 20%, for CH_3CN and CH_3COCH_3 15%. The measurement technique is described in detail by *Lindinger et al.* (1998).
The measurement of HCHO was based on the fluorimetric detection of the Hantzsch reaction product, as originally described by *Belman* (1963). The instrument's noise is about 1.5% of the concentration reading up to concentrations of about 20 ppbv. A detailed description of these measurements is given by *Kormann et al.* (2003).
NO, NO_y and O_3 were measured by the DLR Oberpfaffenhofen, Germany. For NO and NO_y a chemiluminescence detector was used. The accuracy of the NO and NO_y measurements is 5% and 15%, respectively, for concentration levels of 1 ppbv. O_3 is measured with the UV absorption technique with an accuracy of 5%. Details of the instruments are given in *Schlager et al.* (1997) and *Ziereis et al.* (2000).

4.3 Meteorological situation

The mean flow in the extratropics is characterized by the westerlies. The geographical position of the Azores High and the Icelandic Low can modify the zonal flow and therefore have a great impact on the weather in Central Europe and the Mediterranean region. When the High and Low are strongly developed and therefore the pressure gradient is relatively high, relatively moist air masses from the Atlantic Ocean are transported to Europe. In the alternate case, the zonal air flow is weak and meridional and blocking weather systems over Central Europe prevail. The interannually varying pressure gradient between the Icelandic Low and Azores High is generally known as the North Atlantic Oscillation (NAO). It is linked to the general atmospheric and the oceanic circulation systems, the latter being affected by the formation of cold bottom waters in the Arctic ocean and the influx of salty water from the Mediterranean Sea through the Strait of Gibraltar (*Bolle*, 2003). By definition, a relatively high pressure gradient between the Azores High and the Icelandic Low yields a positive NAO index, a low gradient to a negative NAO index. Although its influence has been studied primarily for the winter season, the NAO is associated with considerable monthly and interannual variability and effects have been identified for all seasons. During August 2001, the mean NAO index was about 0.5 (*National Oceanic and Atmospheric Administration*, URL: *www.cpc.ncep.noaa.gov/products/precip/CWlink/daily_ao_index/history/all.index*.2001.*gif* (14 July 2004)).
In summer the Intertropical Convergence Zone (ITCZ) and the Azores High shift toward higher latitudes. This anticyclone in combination with eastward moving low pressure systems over Central Europe lead to westerly flow in the lower and middle atmosphere toward the eastern Mediterranean area. Spreading of the high pressure across Central Europe diminishes the westerly flow and mostly air from easterly or northerly directions respectively is transported into the Mediterranean region. In the upper troposphere air masses are transported by the upper level

westerlies toward the Mediterranean.
During spring and summer the Asian continent begins to heat up, developing a heat low over northern India, Pakistan and Iran that causes the ITCZ to move north, generating the Indian monsoon, with intense deep convection. A semi-permanent anticyclone is located over the surface heat low, the Tibetan High. The Tropical Easterly Jet (TEJ) stream is an inherent feature of the Indian summer monsoon. It is a belt of strong easterly winds, which is part of the southern periphery of this upper tropospheric anticyclone. This TEJ between 200 and 100 hPa transports air from Asia over North Africa and, aided by the upper tropospheric anticyclone over the Arabian Peninsula, toward the eastern Mediterranean. Under the influence of the Subtropical Jet Stream and the westerlies the air is subsequently transported back east over the Asian continent.
During the summer months the Mediterranean area is directly under the descending branch of the Hadley circulation, which is driven by deep convection in the ITCZ. In the upper troposphere, poleward moving air from the ITCZ is deflected by the Coriolis force. The resulting eastward flow reaches a maximum strength in the Subtropical Jet Stream at about 40° in summer, north of the Mediterranean. As a result of subsidence, the region is characterized by cloud-free conditions with high solar radiation intensity. Over land, convection can develop, which is generally not very deep at coastal locations. The air near the surface returns to the equatorial region in the trade winds, gathering moisture over the sea.
In summer teleconnections are found between the Mediterranean region and the South-Asian monsoon and Sahel rainfall regimes on an interannual time-scale (*Ward*, 1992). The sea level pressure over the eastern Mediterranean is anticorrelated with that in the Indian monsoon, mainly in the July-September period, while that in the western Mediterranean is positively correlated with a maximum during September-November. The meridional wind component is anticorrelated with the Indian monsoon over the central and eastern Mediterranean basin. This means that a more active monsoon is connected with lower sea level pressure over the eastern basin and higher over the western basin, and stronger northerly wind over most of the Mediterranean.

4.4 Modeling tools

4.4.1 The FLEXTRA trajectory model

The trajectories have been computed with the FLEXTRA trajectory model (*Stohl et al.*, 1995; *Stohl and Seibert*, 1998)), that was developed at the Institute of Meteorology and Geophysics in Vienna by Andreas Stohl, Gerhard Wotawa and Petra Seibert. Recent updates were made by Andreas Stohl at the Technical University of Munich. The FLEXTRA code is freely available (*Stohl, A.*, *The FLEXTRA homepage* (2 November 2001)., URL: http://www.forst.tu-muenchen.de/EXT/LST/METEO/stohl/flextra.html (14 July 2004)).
Stohl and Seibert (1998), studying potential vorticity conservation, have shown that three-dimensional trajectories are more accurate than all other types, including isentropic trajectories. Thus three-dimensional trajectories were used throughout this study. In addition to the trajectory positions, FLEXTRA also provides other information, such as PV, which is interpolated from grid point values. The positions of all parcels are given every 30 minutes.
As input data, three-dimensional wind fields from the ECMWF analyses are used. For this study a horizontal resolution of 2.0° and a nested domain (latitude range: 15° to 75°, longitude range: -30° to 70°) of 0.5° were employed. It has to be mentioned that the computed position of the tra-

jectories, especially of those trajectories that have a temporal range of several days, is dependent on the resolution of the wind data. This results from the fact that the wind fields are archived every 6 hours and consequently this data has to be interpolated in time and in space.
The calculations are sensitive to initial conditions in the sense that a trajectory can separate rapidly from another trajectory starting nearby (in time or space). As a consequence, uncertainties in the origin of 5-day back trajectories can add up to several hundreds of kilometers, even using the latest high-resolution global meteorological analyses (*Stohl*, 1998a). However, calculation and analysis of an ensemble of trajectories with slightly different initial positions gives a reliable estimation of the sensitivity of the trajectories to initial conditions and errors (*Merril et al.*, 1985; *Seibert*, 1993).
To determine the source regions of the air masses which were sampled during the MINOS campaign, 5-day backward-trajectories were computed. Trajectories were initialized at every minute along the Falcon flight tracks.

The atmosphere was divided into four different height intervals: level one from the surface up to 2 km, level two from 2 to 4 km, level 3 from 4 to 8 km and level 4 from 8 to about 14 km. These levels refer to the flight altitude of the Falcon aircraft during the measurements, i.e., the initialization points of the back trajectories. This implies, for example, that all trajectories with initialization points between 4 and 8 km are attributed to one height level regardless of altitude 5 days earlier.

4.4.2 Mean trace gas mixing ratios

The temporal resolution of the measurement of the different gases was not unique. To compute mean concentrations for the trajectory clusters, the measured values were converted to one minute averages. Hence the gas concentrations could be assigned to the corresponding trajectories, which also have a temporal resolution of one minute.

4.4.3 Source regions

On first inspection of all back trajectories computed for the MINOS campaign period four main clusters of trajectories could be identified. Therefore each of these clusters was defined as representing a source region. These are: 1) western Europe; 2) eastern Europe; 3) the North Atlantic region and North America; and 4) South Asia. These regions are depicted in Figure 4.2. It should be mentioned that especially for the middle and upper tropospheric trajectories the expression "source region" is debatable. Often the trace gases in these air parcels do not have their origin in the particular region depending on whether the trace gas life time exceeds that of the trajectory. Some trace gases are chemically formed from precursor gases that are emitted elsewhere. Nevertheless, in this study this expression is adopted to distinguish the different clusters. For the approximate lifetimes of the sampled trace gases see Table 4.1.

By definition, if an air parcel trajectory resides over a defined region it is added to the particular cluster. Often it appears that the back trajectories reside over two or more defined regions. In this case the residence time of the air parcel above the regions is the decisive point. In this study a minimum residence time of 2.75 days is used to assign such trajectories to their source region. It is thus assumed that during this period the air mass has adopted the chemical characteristics of this region. If a trajectory does not fulfill this criterion for any region it is declared as 'non-defined' and is not further considered. As a result, 184 of the 2690 computed

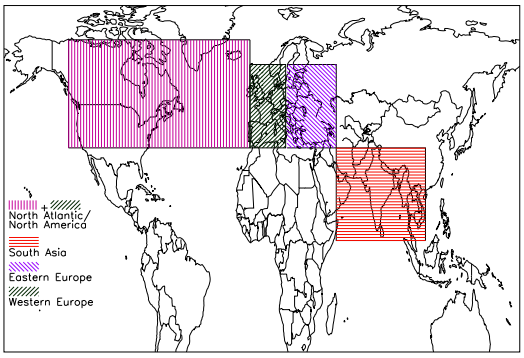

Figure 4.2: Source regions of the trajectories during the MINOS campaign.

HCHO	hours
NO_x	days
NO_y	days to weeks
O_3	days to weeks
CH_3COCH_3	weeks to months
PAN	weeks to months
CO	weeks to months
CH_3OH	months
CH_3CN	months
CH_4	years
CO_2	years

Table 4.1: Approximate lifetime of the sampled trace gases during summer

back trajectories (6.8%) were therefore disregarded.

4.5 Trajectory clusters

4.5.1 Surface - 2 km

Using the criteria described in section 4.4.3 it can be distinguished between air masses from western Europe, notably France, Germany and northern Italy, and from eastern Europe. These two clusters are shown in Figures 4.3a and 4.3b. 176 trajectories were counted for the western region. That is about 22% of all trajectories at this height level. 595 trajectories (about 74%) from the eastern area were registered. The remaining 4% was ignored as being "non-defined". The mean gas concentrations of the eastern and western Europe trajectories are listed in Table 4.2.
It can be seen that all trajectories with source regions in eastern Europe are associated with higher mean concentrations than those from westerly directions, except for CO_2. In particular the mean value of PAN is nearly twice as high (627±224 and 324±99 pptv). The values of acetone (2755±435 and 1953±276 pptv), acetonitrile (203±31 and 136±25 pptv), especially methanol (3169±808 and 1426±411 pptv) but also O_3 (70±6 and 58± 5 ppbv) and CO (156±23

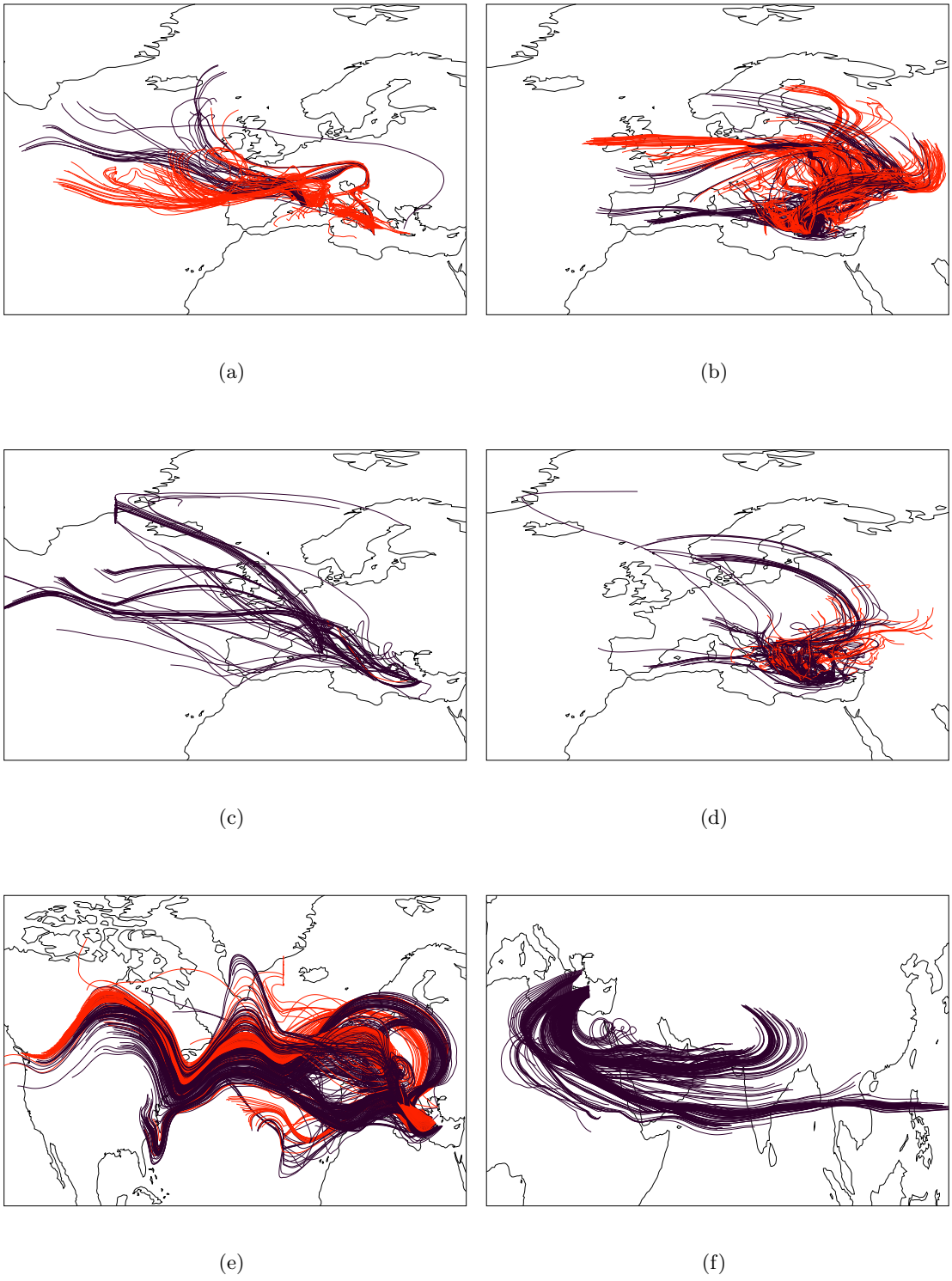

(a) (b)

(c) (d)

(e) (f)

Figure 4.3: Clusters of 5-day back trajectories for different height levels. (a) Western Europe trajectories between the surface and 2 km, (b) same height level for eastern Europe trajectories, (c) same as (a) but between 2 and 4 km, (d) same as (b) but between 2 and 4 km, (e) North Atlantic/North American trajectories between 8 and 14 km, (f) same as (e) but for the South Asian cluster. The red trajectories in (a) to (d) indicate trajectories passing through the planetary boundary layer, in (e) stratospheric trajectories.

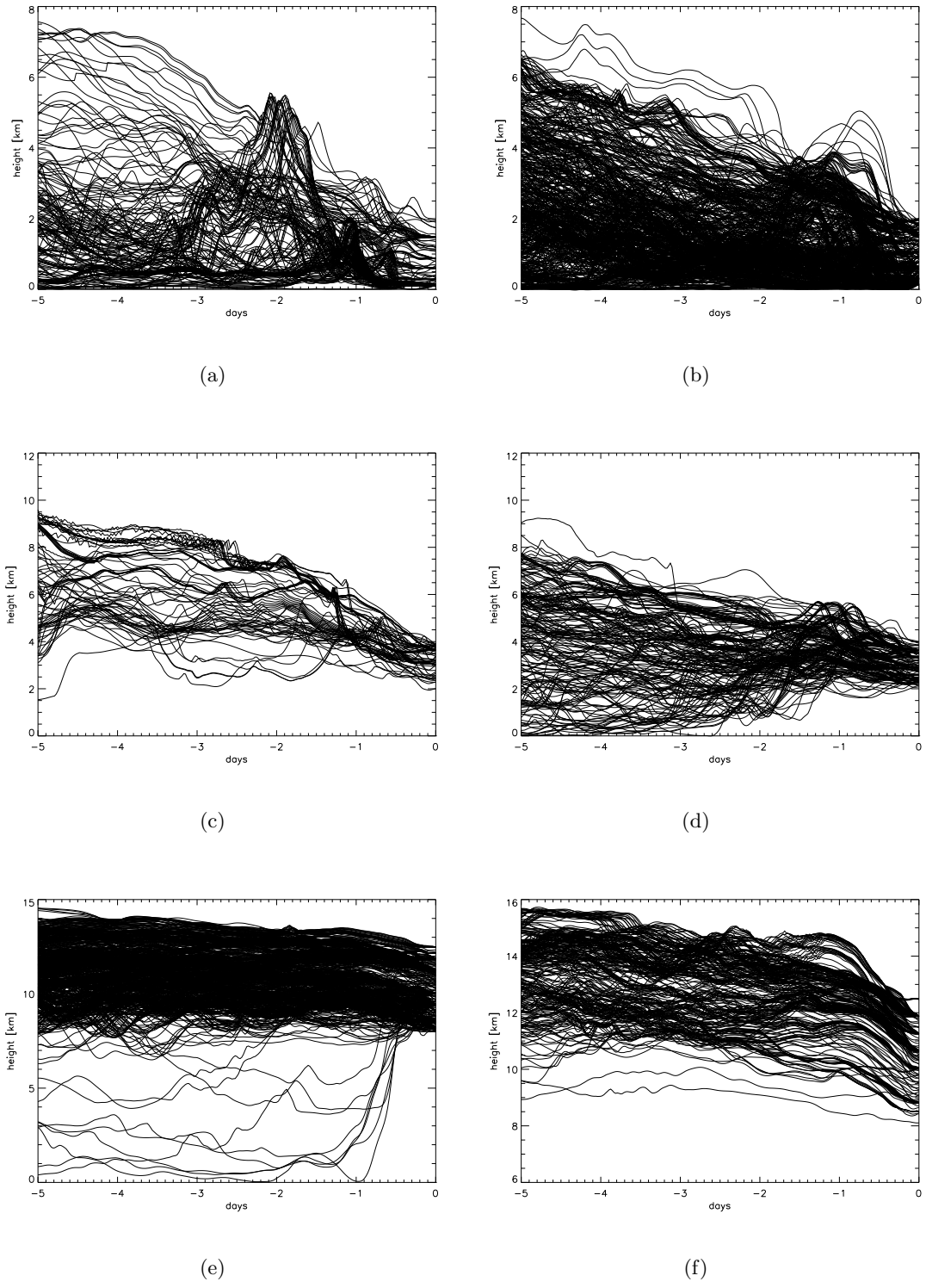

Figure 4.4: Altitude versus time of the 5-day cluster back trajectories. (a) Western Europe trajectories between the surface and 2 km, (b) same height level for eastern Europe trajectories, (c) same as (a) but between 2 and 4 km, (d) same as (b) but between 2 and 4 km, (e) North Atlantic/North American trajectories between 8 and 14 km, (f) same as (e) but for the South Asian cluster.

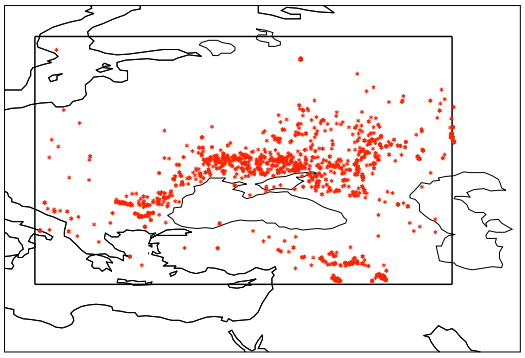

Figure 4.5: Fires detected during nighttime for eastern Europe in August 2001. The defined region of eastern Europe is outlined with a box.

and 126±17 ppbv) are significantly higher in eastern European air.
Figure 4.4 depicts the temporal height development of the western European trajectories. Two thirds originate at altitudes lower than 2 km and mostly do not change altitude much toward the Mediterranean, except a few which are uplifted by low pressure systems over the Atlantic. The remaining one third of these trajectories originates in the free troposphere and descends in the following days toward the Mediterranean region. Likewise about one third of the eastern Europe trajectories originates in the free troposphere (see Figure 4.4b). In Tables 4.3 and 4.4, mean concentrations for eastern Europe and western Europe, respectively, are listed, differentiating between trajectories originating in the free troposphere and in the boundary layer.
Although for both western and eastern Europe the boundary layer trajectories are mostly associated with higher concentrations, the differences are generally small, which is hypothesized by generally well mixing in the lower about 4 km by shallow convection over southern Europe, as evident from satellite images during MINOS. While the ECMWF data being used to calculate the trajectories reproduce the large-scale effects of convection (e.g., strong ascent in the intertropical convergence zone or within Warm Conveyor Belts), smaller-scale convective cells are not resolved (*Stohl et al.*, 2002).
Acetonitrile can be used as a unique tracer for biomass burning (*Holzinger et al.*, 1999). Accordingly the mean gas concentrations suggest more biomass burning in eastern compared to western Europe during MINOS. Figure 4.5 shows a map with the registered nighttime fires in eastern Europe in August 2001 (source: *ATSR World Fire Atlas*, URL: http://shark1.esrin.esa.it/ionia/FIRE/AF/ATSR/DATA/ALGO1/2001/MAPS/0108ESA01.gif (14 July 2004)). In western Europe no fires have been registered for this period. Many of the computed trajectories of the eastern Europe cluster moved over the region with a high density of fires north of the Black Sea (see Figure 4.3b), explaining the enhanced concentration of biomass burning tracers.

4.5.2 2 - 4 km

The situation for the height interval between 2 and 4 km is very similar to the first level. There are also two main regions from where the air was transported toward the Mediterranean area, one from westerly and one from easterly directions. From the west 75 trajectories (23%) were counted,

	western Europe		eastern Europe	
	Mean	Std Dev	Mean	Std Dev
NO	0.04	0.01	0.05	0.02
NO_y	1.1	0.5	1.4	0.4
HCHO	0.9	0.2	1.3	0.4
O_3	58	5	70	6
CH_3OH	1426	411	3169	808
CH_3CN	136	25	203	31
CH_3COCH_3	1953	276	2755	435
PAN	324	99	627	224
CO_2	359	3	358	3
CO	126	17	156	23
CH_4	1873	21	1883	29

NO, NO_y, HCHO, O_3, CO, CH_4 in ppbv, CO_2 in ppmv, CH_3OH, CH_3CN, CH_3COCH_3, PAN in pptv

Table 4.2: Comparison of mean concentrations for height level 1 (0–2 km) for western Europe and eastern Europe trajectories

	free troposphere		boundary layer	
	Mean	Std Dev	Mean	Std Dev
NO	0.05	0.04	0.04	0.03
NO_y	1.4	0.4	1.4	0.5
HCHO	1.3	0.4	1.2	0.3
O_3	70	5	69	5
CH_3OH	3089	782	3460	828
CH_3CN	199	31	216	24
CH_3COCH_3	2680	386	3024	512
PAN	632	230	593	178
CO_2	358	3	359	4
CO	161	20	167	17
CH_4	1880	31	1894	30

NO, NO_y, HCHO, O_3, CO, CH_4 in ppbv, CO_2 in ppmv, CH_3OH, CH_3CN, CH_3COCH_3, PAN in pptv

Table 4.3: Comparison of eastern Europe mean concentrations at height level 1 (0-2 km) of trajectories originating in the free troposphere and in the boundary layer.

	free troposphere		boundary layer	
	Mean	Std Dev	Mean	Std Dev
NO	0.03	0.02	0.08	0.07
NO_y	1.0	0.4	1.4	0.6
HCHO	0.9	0.3	1.0	0.1
O_3	59	5	61	6
CH_3OH	1462	469	1365	322
CH_3CN	129	24	147	23
CH_3COCH_3	1896	234	2046	317
PAN	315	109	340	74
CO_2	358	3	359	3
CO	124	15	133	19
CH_4	1862	19	1881	28

NO, NO_y, HCHO, O_3, CO, CH_4 in ppbv, CO_2 in ppmv,
CH_3OH, CH_3CN, CH_3COCH_3, PAN in pptv

Table 4.4: Same as Table 4.3, but for western Europe trajectories

from the east 201 (62%). The remaining 15% was associated with other regions. Figures 4.3c and 4.3d show the associated 5-day back trajectories. It is notable that the eastern trajectories at this height level 5 days previously do not originate as far north as at the height level below. In this case they originate especially over Turkey, Greece, Bulgaria and the Ukraine. Whereas nearly all western Europe trajectories originate in the free troposphere between about 4 and 9 km, at least about 25% of the eastern Europe trajectories originate in the boundary layer (see Figure 4.4c and Figure 4.4d). The remaining 75% associated with altitudes up to 8 km descend during transport toward the Mediterranean.

Nevertheless the difference in the mean gas concentrations (see Table 4.5) of the western and eastern Europe trajectories is qualitatively similar to level 1 with higher mean gas concentrations for the eastern Europe cluster, with the exception of CH_4 (west: 1837±18 ppbv, east: 1839±20 ppbv), CO_2 (west: 361±3 ppmv, east: 360±4 ppmv) and O_3 (west: 73±13 ppbv, east: 73±8 ppbv). Only the mean NO concentration is higher for the western Europe air masses (west: 0.04±0.03 ppbv, east: 0.02±0.01 ppbv).

As mentioned in section 4.5.1 the enhanced mean concentration of the biomass burning tracer acetonitrile, as well as methanol, acetone and CO, can be traced to the large number of fires north of the Black Sea.

In Table 4.6 the differences of the mean concentrations in the eastern Europe air mass according to their height are shown. Comparable to the level below the lowest layer is most strongly affected by fresh emissions, although the differences are generally small.

4.5.3 4 - 8 km

A large fraction, i.e. 406 of the total number of 509 computed trajectories ending between 4 and 8 km altitude, originates from the North Atlantic/North America region (80%). The remaining

	western Europe		eastern Europe	
	Mean	Std Dev	Mean	Std Dev
NO	0.04	0.03	0.02	0.01
NO_y	0.7	0.3	0.9	0.2
HCHO	0.4	0.2	0.7	0.2
O_3	73	13	73	8
CH_3OH	1614	602	2195	586
CH_3CN	176	33	180	26
CH_3COCH_3	1862	469	2206	433
PAN	537	129	744	149
CO_2	361	3	360	4
CO	99	11	112	15
CH_4	1837	18	1839	20

NO, NO_y, HCHO, O_3, CO, CH_4 in ppbv, CO_2 in ppmv, CH_3OH, CH_3CN, CH_3COCH_3, PAN in pptv

Table 4.5: Comparison of western and eastern Europe trajectories at height level 2 (2-4 km)

20 % is associated with other source regions. Because the low number of trajectories from these regions, a comparison of the trace gas concentrations of the different clusters at this height was not performed. Nevertheless, in Table 4.7 the mean concentrations for the trace gas concentrations of the NAONA cluster are listed to compare these with the NAONA region values of the height interval aloft.

4.5.4 8 - 14 km

At this height interval two main directions appear from where the air is transported toward the Mediterranean area. Most of the air originates from the west. For these trajectories (see Figure 4.3e), there seems to be a coherent cluster at the west of Africa. By computing these back trajectories for more than 5 days it can be shown that they also have their source region over North America. A separate analysis of the gas concentrations of this cluster moreover shows no significant differences with the rest of the trajectories shown in Figure 4.3e. Therefore all these trajectories are treated as one cluster. On the other hand, Figure 4.3f consistently shows 5-day back trajectories originating over South Asia. Consequently these two very different clusters can be analyzed and compared. The number of the NAONA trajectories is 645, which is 61% of all trajectories at this height level. For the Asian cluster 271 trajectories were counted (26%). 13% were associated with other source regions.
The North American trajectories mainly start 5 days back at heights above 8 up to 14 km (Figure 4.4e), decreasing with altitude in time due to subsidence. Only a few trajectories originating in the lower troposphere are apparent. The geographical position of many upper tropospheric trajectories is further north, close to the jet stream, so there may be an enhanced possibility of mixing with stratospheric air. In Figure 4.6 the PV values along a representative selection of

	free troposphere		boundary layer	
	Mean	Std Dev	Mean	Std Dev
NO	0.02	0.01	0.02	0.01
NO_y	0.9	0.3	0.9	0.2
HCHO	0.7	0.3	0.7	0.1
O_3	72	8	75	9
CH_3OH	2143	561	2439	694
CH_3CN	176	25	198	23
CH_3COCH_3	2190	432	2284	428
PAN	749	155	718	104
CO_2	361	4	360	4
CO	109	12	121	19
CH_4	1839	20	1838	21

NO, NO_y, HCHO, O_3, CO, CH_4 in ppbv, CO_2 in ppmv,
CH_3OH, CH_3CN, CH_3COCH_3, PAN in pptv

Table 4.6: Comparison of eastern Europe mean concentrations at height level 2 (2-4 km) of trajectories originating in the free troposphere and in the boundary layer

all NAONA trajectories is depicted, showing stratospheric influence along the transport paths and also over the Mediterranean, indicating that some measurements onboard the aircraft took place in the lowermost stratosphere. The Asian trajectories, starting between 9 and 16 km (Figure 4.4f), furthermore decrease with altitude in time associated with subsidence deeper into the troposphere especially near North Africa. The position of these trajectories is more toward the south where the tropopause is relatively high (about 16 km). PV analyses of these trajectories indicates no stratospheric influence (not shown).

For comparison with the Asian air masses all NAONA trajectories being directly influenced by the stratosphere (about 50%) were removed. The mean gas concentrations for these two clusters are listed in Table 4.8. It appears that the standard deviations of the NAONA cluster trace gas concentrations are partly much higher than that for South Asia, notably of acetone, methanol and PAN, signifying a much higher variability of the sources in this region, associated with a much higher geographical spread of the NAONA trajectories.

In contrast to the lower height levels, none of these two clusters is clearly characterized by enhanced mean concentrations of all trace gases. Whereas NO_y, O_3 and CH_3COCH_3 of the NAONA sector are higher, the values of HCHO, CO, methanol and CH_4 are higher for the South Asian cluster. The mean PAN concentration for that cluster is low compared with NAONA . It has to be emphasized, however, that the number of trajectories associated with PAN concentrations for the Asian cluster is very limited (16). Therefore the comparison of the PAN concentrations is of limited value.

Although the stratospheric trajectories are excluded, the mean NAONA ozone concentration is still higher than the Asian value. This may be caused by strong upward transport from the polluted boundary layer previous to the simulated five days, associated with photochemical production along the transport paths. Warm Conveyor Belts, for instance, are an important

	Mean	Std Dev
NO	0.03	0.02
NO_y	0.6	0.2
HCHO	0.3	0.1
O_3	72	12
CH_3OH	1014	441
CH_3CN	159	26
CH_3COCH_3	1549	376
PAN	447	146
CO_2	366	3
CO	83	11
CH_4	1833	21

NO, NO_y, HCHO, O_3, CO, CH_4 in ppbv, CO_2 in ppmv,
CH_3OH, CH_3CN, CH_3COCH_3, PAN in pptv

Table 4.7: Mean concentrations of the North Atlantic region between 4 and 8 km

	North Atl.region		South Asia	
	Mean	Std Dev	Mean	Std Dev
NO	0.1	0.1	0.1	0.1
NO_y	1.0	0.3	0.6	0.1
HCHO	0.4	0.1	0.6	0.3
O_3	81	16	57	6
CH_3OH	946	413	1002	218
CH_3CN	149	14	147	44
CH_3COCH_3	1299	371	1101	126
PAN	324	114	148	44
CO_2	368	3	364	3
CO	77	11	98	7
CH_4	1831	20	1867	20

NO, NO_y, HCHO, O_3, CO, CH_4 in ppbv, CO_2 in ppmv,
CH_3OH, CH_3CN, CH_3COCH_3, PAN in pptv

Table 4.8: Comparison of North Atlantic region and South Asian mean concentrations between 8 and 14 km. For the NAONA cluster only tropospheric trajectories are considered.

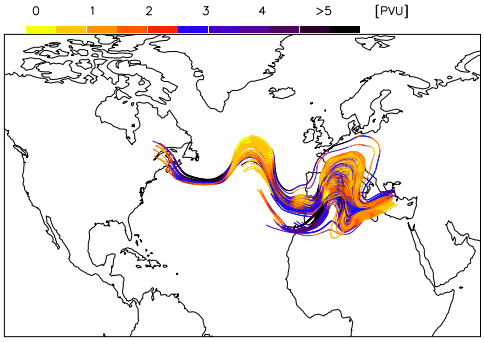

Figure 4.6: Potential vorticity of a subset of the North Atlantic region trajectories. Some air parcels temporarily have potential vorticity values higher than 3.5 PVU, indicating stratospheric influence.

mechanism to transport pollution from the North American boundary layer to the upper troposphere (*Stohl and Trickl*, 1999).

Mean CO mixing ratios exceeding 80 ppbv in the middle and upper troposphere suggest a direct continental influence (*Board et al.*, 1999). CH_4 is also enhanced in the South Asian cluster, possibly from rice cultivation. Therefore, it is likely that South Asian air pollution is transported within a few days through the Asian monsoon convection to the upper troposphere, after which it follows the upper-level anticyclone toward the eastern Mediterranean. A selection of 20-day forward trajectories, initialized each day in July 2001, with starting points in two West Indian cities (Madras, Patna) in Figure 4.7 support this assumption. Figures 4.7a and 4.7c clearly show the anticyclonic circulation, while in Figures 4.7b and 4.7d the fast upward transport of the trajectories up to about 15 km in the monsoon convection is depicted. The duration of transport from the Indian cities to the upper troposphere over the eastern Mediterranean is about 10 - 15 days. Even if the uncertainties in the origin of 20-day back-trajectories can add up to several hundreds of kilometers, these trajectories seem to be representative of transport from Indian boundary layer air. Once being transported by the strong monsoon convection into the upper troposphere (2 - 7 days), the Tibetan High transports the air toward the Mediterranean area.
The calculated travel times are in good agreement with the estimated chemical age of the Asian monsoon outflow measured during the MINOS campaign over the eastern Mediterranean by *Scheeren et al.* (2003).

4.6 Conclusions

In this chapter an analysis of back trajectories for the MINOS campaign in August 2001 combined with measured trace gas concentrations is presented. The goal was the investigation of long-range transport of pollutants into the Mediterranean area and the determination of a relationship between the origin of trajectories and the observed concentration at the time of their arrival.
As determined by the large-scale atmospheric circulation, "typical" flow patterns at different height levels could be identified. Between the surface and 2 km altitude strong influences from

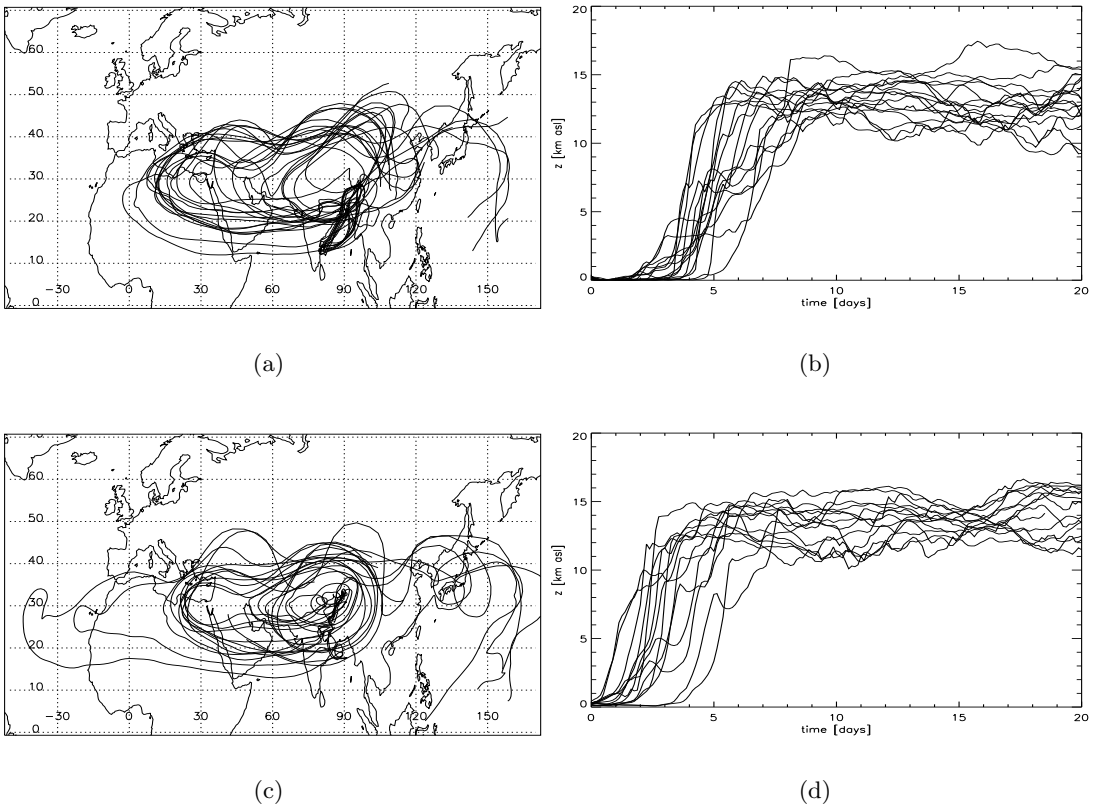

(a) (b)

(c) (d)

Figure 4.7: 20-day forward trajectories for two big Indian cities a) Madras (80.76E / 13.85N, southeast India) and c) Patna (85.72E / 26.01N, northeast India) in July, 2001. Figure b) shows the temporal development of the trajectory height above sea level for the Madras trajectories and d) for those from Patna.

western and eastern Europe is inferred. The same applies to the height level of 2 to 4 km. About 74% of the computed trajectories at the lowest level was associated with the eastern European cluster, whereas 22% was western European. The remaining 4% was ignored as being "non-defined". At the height of 2 to 4 km these values changed to about 62%, 23% and 15%, respectively. Whereas the air between 4 and 8 km mainly originated from the North Atlantic region (80%), there was an additional strong influence above 8 km from South Asia. At this level about 61% of the trajectories came from the west, and 26% from South Asia. The remaining 13% was associated with other source regions.

In spite that the definition of the "source regions" is somewhat subjective and therefore open to discussion, substantial differences in the mean gas concentrations between the different clusters and hence source regions are evident.

This is especially true for the lowest two height levels. The trace gas concentrations with the eastern European 5-day back trajectories were significantly higher than with the western European trajectories, signifying a higher level of air pollution. By differentiating between trajectories in the boundary layer and in the lower free troposphere, the differences in the mean gas concentrations are generally small, which can be explained by mixing in shallow convection over southern Europe.

Generally speaking the concentrations of the trace gases at the highest level (between 8 and 14 km), originating from the NAONA region and from South Asia, do not differ as much as at the levels below, indicating a relatively higher level of uniformity in upper tropospheric air pollution in the northern hemisphere. Nevertheless these air masses did show typical chemical characteristics. Air from the NAONA source region seems to be directly influenced by the stratosphere, while air from South Asia, on the other hand, did not show these influences. Since CO and CH_4 were enhanced in these air masses, relatively rapid transport from the surface by strong convection in the Indian monsoon is inferred.

Chapter 5

Cross-tropopause transport over the eastern Mediterranean[2]

Abstract

The transport of air between the troposphere and the stratosphere over the eastern Mediterranean Sea and the neighbouring countries up to the Black Sea is investigated, using a trajectory model and analyzed winds from the European Centre for Medium-Range Weather Forecasts. It is found that in summer the upper troposphere in this region is influenced by both westerly winds in the Polar Front Jet and southerly winds at the western flank of the upper-level anticyclones over the Arabian and Asian heat lows. The convergence of these air-flows accelerates the horizontal wind and increases the horizontal and vertical wind shear, creating a jet streak within the Subtropical Jet Stream and deep tropopause folds. Clear-air turbulence, caused by horizontal deformation and the vertical wind shear along the Subtropical Jet Stream, and consequently turbulent mixing of tropospheric and stratospheric air near the tropopause region appears to contribute strongly to the cross-tropopause transport over the eastern Mediterranean in summer.

5.1 Introduction

Transport of air from the stratosphere to the troposphere and in the opposite direction is important for the dynamics and the chemical composition of the atmosphere.
As already summarized in chapter 3, there are many processes causing cross-tropopause transport and being responsible for the temporal and spatial distribution of air mass transport. A 15-year climatology of cross-tropopause transport is presented by *Sprenger and Wernli* (2003), for instance. While in middle to high latitudes nearly the whole year troposphere to stratosphere transport occurs in association with low pressure systems, additionally during summer troposphere to stratosphere transport intensifies over the eastern Mediterranean and the area westward up to the Black Sea.

In summer the displacement of the Intertropical Convergence Zone with the Indian monsoon is associated with intense deep convection. In the upper-level a high pressure system over the Asian surface Low is formed, the Tibetan High. The Tropical Easterly Jet (TEJ) stream is

[2]This chapter is based on: Traub, M. and Lelieveld, J. (2003), *J. Geophys. Res.*, Vol.108, No:D23, 4712, 10.1029/2003JD003754

an inherent feature of the Indian summer monsoon. It is a belt of strong easterly winds at the southern flank of the upper tropospheric anticyclone. As shown in chapter 4, this TEJ between 200 and 100 hPa transports air from Asia over North Africa and, aided by the upper tropospheric anticyclone over the Arabian Peninsula, toward the eastern Mediterranean. *Chen* (1995) has shown that troposphere to stratosphere transport is intensified in regions at the west side of the Asian-Arabian upper level anticyclones.
Considering the trajectory analysis of the MINOS campaign in chapter 4, which underscored the convergence of anthropogenic polluted air masses from Europe, America and South Asia during summer over the eastern Mediterranean, the cause of the intensified cross-tropopause transport over that region has special significance.

In the present study cross-tropopause transport over the eastern Mediterranean region being associated with clear-air turbulence in a jet streak is investigated. In section 5.2 trajectory model output is presented and compared with European Centre for Medium-Range Weather Forecasts analyses. In section 5.3 an operational turbulence index for diagnosis and prediction of clear-air turbulence is introduced and applied to the ECMWF wind fields. In section 7.4 the areas of clear-air turbulence are associated with the locations of cross-tropopause transport computed with a trajectory model. Finally, section 5.5 concludes by summarizing the main facts.

5.2 Methodology and data

Analyzing trajectories for the MINOS campaign (chapter 4) relatively high PV values toward the eastern part of the Mediterranean region and lower values at the same height levels toward the west were found.

Three-dimensional trajectories have been computed with the FLEXTRA model (*Stohl et al.*, 1995; *Stohl and Seibert*, 1998), which was already introduced in section 4.4.1.
As input data for the trajectory model, three-dimensional meteorological fields from the ECMWF analyses at six-hourly intervals with 1° x 1° horizontal resolution and 60 vertical hybrid levels were used. The vertical resolution of the analyses data around the tropopause is about 30 hPa. In the ECMWF model subgrid-scale mixing of air is implicitly taken into account by parameterization. To analyze the clear-air turbulence at the dynamical tropopause, 1° x 1° ECMWF analyses at constant pressure levels (700, 500, 400, 300, 250, 200 hPa) were used.

To determine the positions of the trajectory's transition from the troposphere to the stratosphere PV values along each trajectory were analyzed. Having a PV value lower than 3.5 PVU at the beginning of the computation, the geographical position where the PV value first exceeds this value during the next 24 hours was declared as transition point. Figure 5.1 shows the transition points for a starting heights of 300 hPa and the corresponding initialization points. The trajectories were initialized once a day in August 2001. Even though the total number of computed trajectories that cross the tropopause is low (about 3%), the eastern Mediterranean seems to be a location with favoured troposphere to stratosphere transport relative to the surrounding area. The cross-tropopause transport north of the eastern Mediterranean can be associated with the subpolar jet stream (*Fischer et al.*, 2000; *Zahn and et al.*, 2000) and the frequent occurrences of cyclones (*Sprenger and Wernli*, 2003). It was further found that the residence time of these trajectories in the stratosphere is of relatively short duration. Only about 25% resides more than a day in the lower stratosphere before crossing the tropopause again.

The analysis of the mean PV distribution at different height levels for August 2001 shows a

decreased tropopause height over the eastern Mediterranean in comparison to the surrounding area. Figure 5.2 shows the mean ECMWF PV distribution at 250 hPa. A tongue shaped area with PV values higher than 2 PVU extends from higher latitudes to the eastern part of the Mediterranean. Comparison of the locations of transition over the eastern Mediterranean during August 2001 (Figure 5.1) shows a significant correlation with the location of the area with increased tropopause height.

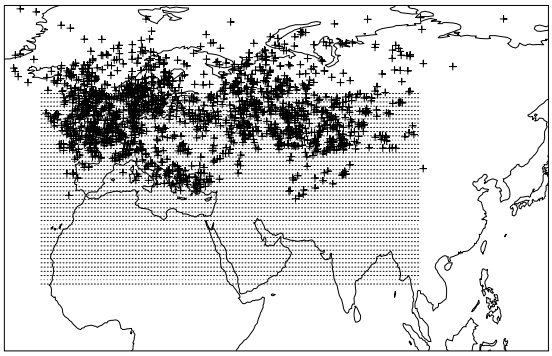

Figure 5.1: Locations of the transitions from the troposphere to stratosphere within 24 hours along trajectories that have started at about 300 hPa. The starting points of all computed trajectories are indicated by the hatched area (20° E to 100° W longitude, 15° N to 60° N latitude).

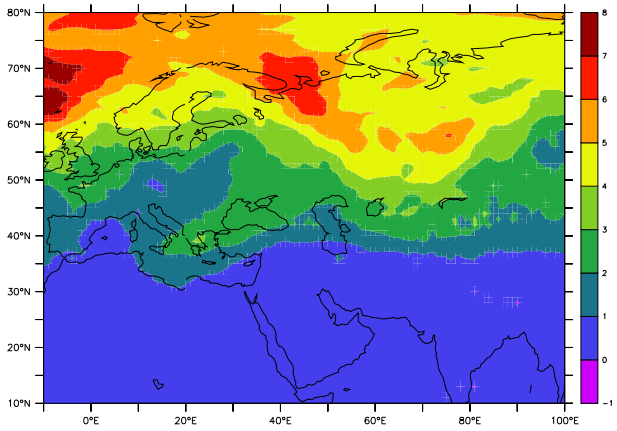

Figure 5.2: Mean PV distribution in PVU from ECMWF analyses for August 2001 at 250 hPa.

The upper troposphere over the eastern Mediterranean is on the one hand influenced by the upper-level anticyclone over the Arabian Peninsula and the Tibetan Plateau. On the other hand air masses are transported from the west, either directly by the midlatitude westerlies or by the meandering Polar Front Jet (PFJ), in the latter case having a stronger northly component. In the convergence zone of these air flows the wind speed is increased. Figure 5.3 shows the mean ECMWF horizontal wind at 250 hPa and highlights the regions with flow velocities larger than 16 ms^{-1}. An area with relatively high wind speeds marks the PFJ, and a strong jet streak is located within the Subtropical Jet (STJ) Stream from the Mediterranean eastward, converging

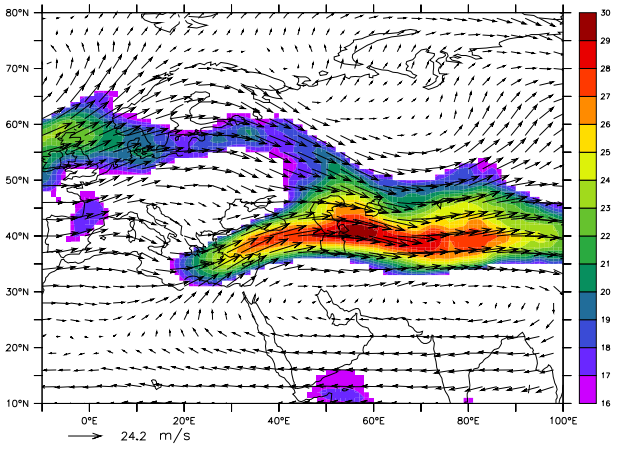

Figure 5.3: Mean ECMWF wind field in August 2001 at 250 hPa. Regions with flow velocities in excess of 16 ms^{-1} are highlighted.

at about 40° N.

5.3 Clear-air turbulence

Clear-air turbulence (CAT) is non-convective turbulence typically outside the planetary boundary layer, often in the upper troposphere. CAT areas have horizontal dimensions of 80 - 500 km along the wind direction and 20 - 100 km across (*Overeem*, 2002). Vertical dimensions are 500 - 1000 m, and the lifespan of CAT is between half an hour and a day. Generally two mechanisms can cause CAT: Kelvin-Helmholtz instabilities and mountain-waves. Kelvin-Helmholtz instabilities occur when vertical wind shear within a stable layer exceeds a critical value. The breaking of the Kelvin-Helmholtz waves causes turbulence.

Ellrod and Knapp (1992) describe an operational turbulence index (TI) for diagnosis and prediction of CAT. The TI is based on the product of horizontal deformation and vertical wind shear at the particular height level.

$$TI = [(\frac{\partial u}{\partial x} - \frac{\partial v}{\partial y})^2 + (\frac{\partial v}{\partial x} + \frac{\partial u}{\partial y})^2]^{0.5} \cdot \frac{\partial \vec{V}}{\partial z} \tag{5.1}$$

where u and v are east-west and north-south wind components in ms^{-1}, $\vec{V}$ is the vector wind and z the height of a standard pressure surface in m. The partial derivatives can be approximated from the differences between grid-points, and ∂z is the height difference in meters between two adjacent height levels. The probability of the occurrence of turbulence increases with TI. The TI values are in units of 10^{-7} sec^{-2}.

5.4 Association of CAT areas with cross-tropopause transport

For further analysis the focus is on the 250 hPa level, because it is typically beneath the tropopause in the tropics and subtropics, whereas it is above the tropopause in high latitudes. The result of applying equation (5.1) to the mean ECMWF horizontal wind at 250 hPa is shown in Figure 5.4. Coincident with the locations of transition from the troposphere to the stratosphere

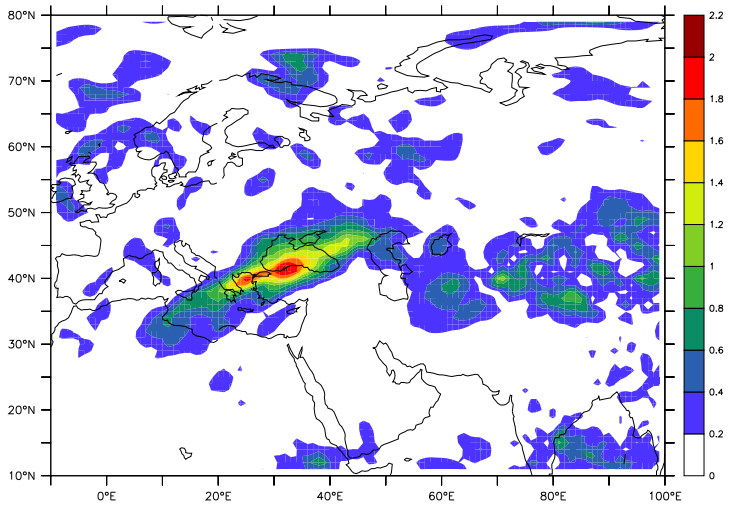

Figure 5.4: Mean TI index in 10^{-7} sec^{-2} in August 2001 at 250 hPa.

(Figure 5.1) and PV (Figure 5.2) a tongue shaped area with enhanced TI values can be seen over the eastern Mediterranean. Maximum TI index values up to about 2.2 south of the Black Sea indicate areas with an enhanced probability of turbulence. It is suggested that this turbulence, induced by upper-level convergence near the tropopause and consequential strong wind shear, causes mixing of tropospheric and stratospheric air near the tropopause and therefore plays an important role in the cross-tropopause transport. *Shapiro* (1976, 1978) presented evidence for clear-air turbulence at jet stream levels as a first-order process in modifying potential vorticity, thus permitting air parcel exchange across the tropopause.

Additionally single day events were analyzed to ensure that the averaging of meteorological parameters does not cause an ambiguous correlation. It was found that the STJ is typically being located at about 35°- 40° N. Depending on the location of the PFJ a jet streak with entrance over the eastern Mediterranean is formed and, especially as a result of strong vertical wind shear, high TI values occur at about 30° N, north of the jet core. The single day analyses indicate that enhanced wind speeds at the PFJ and STJ are associated with descent of the tropopause within that region and also with high TI values. For a better understanding two days with different flow patterns are presented.

Figure 5.5a shows the TI index and the wind field on 2 August at 250 hPa. Between 50 and 70° N the meandering PFJ with wind speed maxima up to 55 ms^{-1} is associated with high TI values especially at its poleward flank. At about 40° N a jet streak occurs with a center south of the Black Sea. Highest TI values occur at about 22° to 35° E along the northern side of this jet streak, where air masses from the south-west, transported by the upper-level anticyclone, and the north-west, transported by a strong jet at the western side of a weak trough over western Russia, converge. The corresponding PV distribution at 250 hPa, with the locations of cross-tropopause transport overlayed, is shown in Figure 5.5b. At this height the course of the tropopause in the higher latitudes matches the course of the PFJ. Further south regions with stratospheric PV values coincide with enhanced TI values over the south of the Black Sea. The locations of transition from the troposphere to the stratosphere on August 2 coincide with the areas of stratospheric PV values at 250 hPa, i.e. along the PFJ and over the eastern Mediterranean region. In Figure 5.5c the cross section at 30° E of the TI value, the wind speed, the 2 and 4

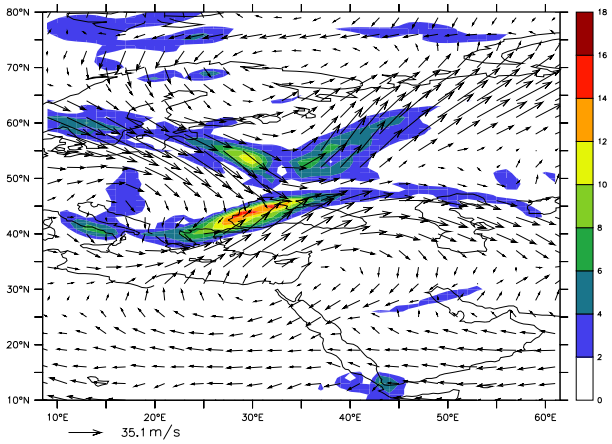

(a)

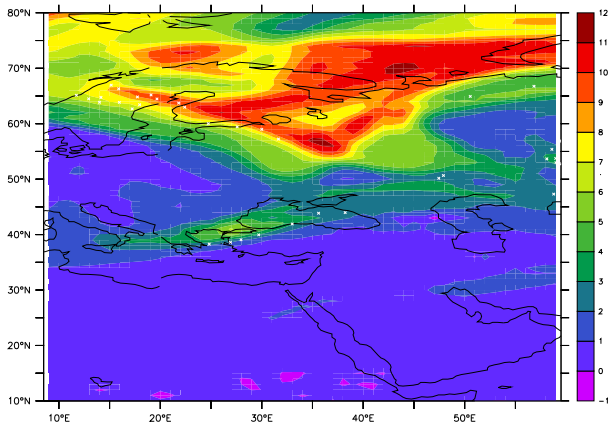

(b)

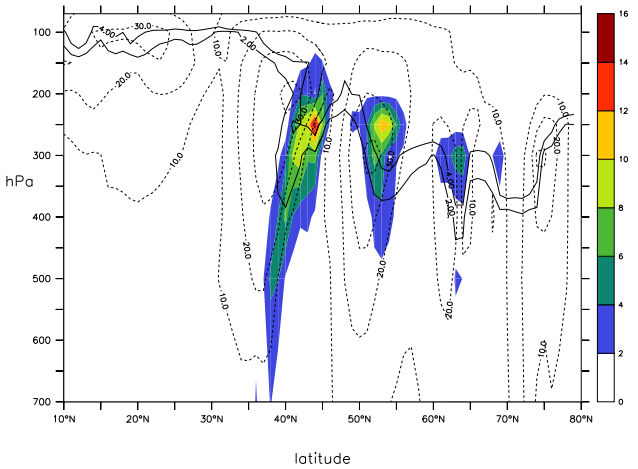

(c)

Figure 5.5: a) TI index in 10^{-7} sec^{-2} and the associated wind field at 250 hPa, b) PV distribution at 250 hPa and locations of cross-tropopause transport (white crosses) and c) cross section of TI index, wind speed in ms^{-1} (dotted lines) and the 2 and 4 PVU iso-surfaces (solid lines) for 30° E on 2 August 2001.

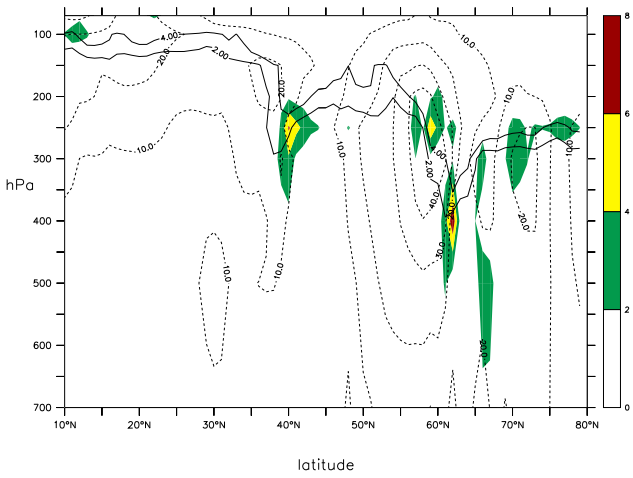

Figure 5.6: Same as Fig. 5.5c) but for 15° E.

PVU iso-surfaces are depicted. The height of the tropopause decreases with increasing latitude, however, not continuously. Three tropopause anomalies can be detected, at about 40°, 53° and 63° N. The first is associated with the jet streak within the STJ, the two others with the PFJ. At the poleward side of the jet cores high TI values within the tropopause anomalies occur. Especially the fold at about 40° N, reaching the 380 hPa level, is remarkably deep. In Figure 5.4 the corresponding cross section at 15° E outside the jet streak is depicted, which again shows a tropopause depression of the STJ at about 40° N, although the TI values and the wind speed are significantly lower and the tropopause does not descend as far as in the jet streak further west.

On 11 August the overall flow pattern is slightly different. As can be seen in Figure 5.4a the amplitude of the baroclinic wave has increased. While a trough was located over central Europe, a strong ridge has formed over western Russia that is associated with a strong southwesterly jet. As a result the influence of the PFJ over the eastern Mediterranean has decreased. Air masses transported from the west and by the upper level anticyclone converge in the eastern Mediterranean region without formation of a jet streak. Enhanced TI values again can be found at the poleward side of the PFJ, but not over the eastern Mediterranean. The PV distribution in Figure 5.4b shows stratospheric values especially at the higher latitudes with the tropopause at 250 hPa. Coinciding with the areas of stratospheric PV, there was no cross-tropopause transport over the eastern Mediterranean simulated on August 11. The cross section in Figure 5.4c shows two minor tropopause depressions, one at about 43° N and a second at about 64° N, being associated to the STJ and the PFJ, respectively. In contrast to 2 August the wind speed at the southern tropopause break was less and no enhanced TI values occurred.

The analyses of the locations of cross-tropopause transport from the stratosphere to the troposphere, which showed good overall agreement with the locations of cross-tropopause transport from the troposphere to the stratosphere (not shown), and additional analysis of the potential temperature along each trajectory (also not shown), confirm the assumption of mixing of air masses being located near the tropopause. The computed values, which change only slightly during transport, lie between 330 and 360 K, being characteristic for the uppermost troposphere and lowermost stratosphere.

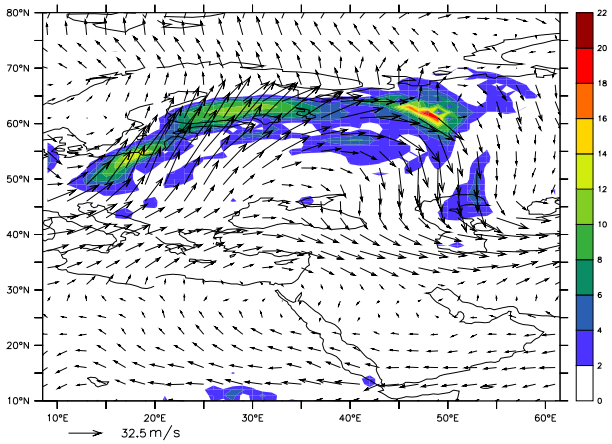

(a)

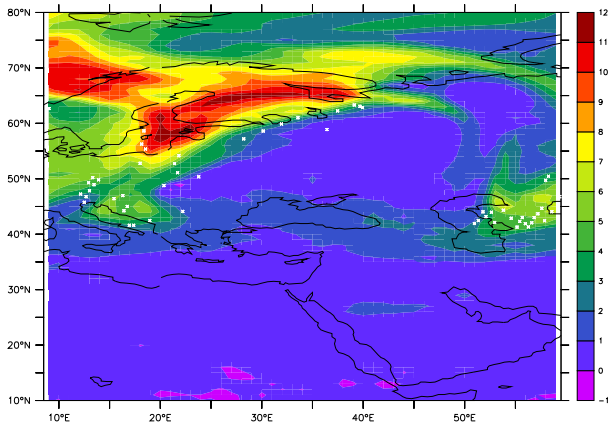

(b)

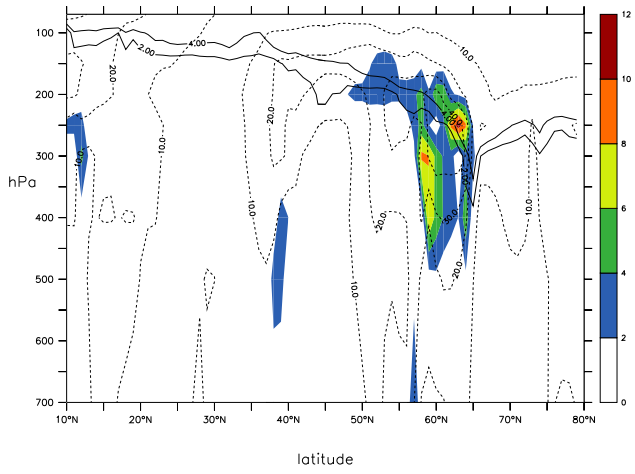

(c)

Figure 5.7: Same as Figure 5.5, but on 11 August 2001.

5.5 Conclusions

In this chapter cross-tropopause transport over the eastern Mediterranean is investigated. Associated with the convergence of air transported by the upper-level anticyclone over the Arabian and Asian heat lows as well as by the Polar Front Jet toward the eastern Mediterranean, a jet streak with entrance over the implied region within the Subtropical Jet Stream is formed. At the cyclonic side of this jet streak the tropopause descents to lower height levels, depending on the wind speed within the jet. As a result of horizontal and vertical wind shear along that jet streak, clear-air turbulence causes mixing of tropospheric and stratospheric air near the tropopause, mainly at the cyclonic side of the jet axis. Analysis of the potential temperature along the trajectory's path after crossing the tropopause, indicates that mixing of air masses is largely confined to the tropopause region, whereas deep transport of tropospheric air to the stratosphere and vice versa does not seem to occur. Being in the end the result of large-scale synoptic flow systems, the Polar Front Jet and the Arabian and Asian heat lows, the latter two being quasi-permanent only during summer, turbulent mixing of air near the tropopause is suggested to play an important role in cross-tropopause transport during summer.

As indicated by the MINOS campaign, anthropogenic polluted air masses converge over the upper tropospheric eastern Mediterranean during summer, and influence the chemical composition of the tropopause region.

Chapter 6

Evaluation of the lagrangian transport model ATTILA

Abstract

First results of the lagrangian transport model ATTILA being coupled to the chemistry-climate model ECHAM5/MESSy are presented. For validation of the accurate coupling, trajectories within an Warm Conveyor Belt over the North Atlantic Ocean are calculated with ATTILA and compared to the results of the frequently used off-line trajectory model FLEXTRA. A second test consists of the simulation of Asian monsoon trajectories. Both tests validate the accuracy of ATTILA in combination with ECHAM5/MESSy.
Sensitivity runs by changing the horizontal resolution of ECHAM5/MESSy indicate that the scientific goal rather than a general conclusion about the accuracy of the calculations should be the determining factor for the choice of the horizontal resolution of ECHAM5/MESSy and ATTILA. In case of a survey of the air flows in a specific region, ATTILA in combination with a coarse resolution provides much of the necessary information. For all analyses that require the information of the path of single trajectories (e.g., origin of air masses at discrete positions and small horizontal and vertical dimensioning, calculations of mass fluxes) it is recommended to run ECHAM5/MESSy with ATTILA at relatively high horizontal resolutions (T63 - T106), whereas the differences between T106 and T159 are expected to be small.

6.1 Introduction

As stated in section 2.2, various steps in the trajectory calculations can be associated with errors, which can lead to misinterpretations of flow situations. Apart from truncation errors approximating equation (2.1) by a finite-difference scheme and different interpolation schemes, the quality but also the temporal and spatial resolution of the underlying wind fields strongly influence the accuracy of the calculated trajectories (*Stohl*, 1998a). *Stohl et al.* (2001) point out that the use of wind fields every three hours, instead of the more usual six hours, represents a significant improvement for trajectory calculations, resulting e.g. in stronger vertical motions. Generally, the availability of temporally and spatially highly resolved meteorological data is a limiting factor for off-line trajectory models.

Analyzing measurement campaigns often involves not only the different pathways and the origin of the measured air masses of interest, but often also chemical compositions. Traditional approaches to represent the evolution of trace species concentrations on a global scale have been Eulerian, using grids and finite differences, or pseudospectral. These models work quite well when applied to smoothly varying meteorological fields, but they can lead to several problems when advecting highly inhomogeneous tracer distributions. In the presence of sharp gradients, many numerical schemes tend to produce negative concentrations, or result in considerable numerical diffusion. Spectral techniques suffer from truncation errors and from the so called Gibbs phenomenon, producing regions of over- and undershoots when gradients are sharp. While undershooting often results in negative concentrations and can therefore be corrected a posteriori, it is not so easy to detect regions of overshoots. In the case of water vapor, for example, overshooting can lead to super-saturation and, consequently, to production of spurious precipitation (*Williamson and Rasch*, 1989).

A lagrangian approach does not suffer from these problems. By this method, the model atmosphere is divided into a large number of air parcels, of which the centroids are advected by the wind. Each trace constituent is thereby represented by a mass mixing ratio in each parcel. Not the tracer concentrations are altered by the advection scheme, but the locations of the concentrations, i.e., the locations of the centroids of the parcels. Such a scheme is strictly mass conserving and does not exhibit numerical diffusion. Moreover, all trace constituents are advected simultaneously, and therefore the computational cost of the advection scheme is independent of the number of tracers transported. For this reason lagrangian methods are preferred when the transport of a large number of trace species is involved.

Furthermore, lagrangian climatologies yield new insights into many types of atmospheric transport problems. They allow classification of air flows and examination of their different properties, and they can be used to obtain estimates of the fluxes between different layers in the atmosphere (e.g., troposphere and stratosphere), which are more robust than values obtained with Eulerian methods.

For these purposes, the lagrangian transport model ATTILA (**A**tmospheric **T**racer **T**ransport in a **L**agrangian **M**odel) was developed at the Institute of Atmospheric Physics, DLR, Oberpfaffenhofen, Germany, and coupled to the general circulation model ECHAM4 (*Roeckner et al.*, 1996). Many simulations on a climatological time scale have been performed and discussed extensively by *Reithmeier and Sausen* (2000).

So far, ATTILA has been used only for simulations on a climatological time scale. Being coupled to a chemistry-climate model, ATTILA also provides a powerful tool for the analysis, and even atmospheric chemical forecasts for measurement campaigns, combining the information of spatially and temporally highly resolved three-dimensional and consistent wind fields, and the transport of different trace species for the classification of air flows and their different properties. Therefore, it has to be ensured that ATTILA resolves air flows in meso- and synoptic-scale weather systems on the time scale of a few days with realistic travel times.

The intention of this study is the validation of the accurate coupling of the lagrangian advection scheme ATTILA with ECHAM5/MESSy and the evaluation of its transport characteristics on a time scale of a few days by simulation of synoptic-scale events in a pure dynamical sense.

After the description of the chemistry-climate model ECHAM5 in section 6.2 and the so called nudging technique (section 6.2.1), the interface structure MESSy is briefly introduced in section 6.3, followed by section 6.4 that deals with a criterion for the comparison of trajectories.

In section 6.5 a short description of the main features of ATTILA is presented. Section 6.6 presents first results of ATTILA in combination with ECHAM5/MESSy. In a first test, referring to an intercomparison of three off-line trajectory models, trajectories along strong ascent within a warm conveyer belt are simulated with ATTILA and compared to the results of the frequently used off-line trajectory model FLEXTRA (section 6.6.1). In the second test a set of trajectories, starting in the Indian boundary layer throughout a time period of a month, are calculated and analyzed for their travel time from Asia to the upper-level Mediterranean (section 6.6.2). Finally, the influence of different horizontal resolutions of ECHAM5/MESSy on the lagrangian transport is presented in section 6.6.3. Section 6.7 concludes by summarizing the most important statements.

6.2 The general circulation model ECHAM5

The spectral atmospheric general circulation model ECHAM5 is the fifth generation of the Hamburg climate model. The model is based on the weather forecast model of the ECMWF. Numerous modifications have been applied to this model at the Max Planck Institute for Meteorology and the German Climate Computing Centre (DKRZ), both in Hamburg, Germany, to make it more suitable for climate simulations, and it is now a model used by a large research community.
ECHAM5 is available at different horizontal resolutions from T21 to T159 triangular truncation, which determines the number of waves explicitly resolved on the globe. In the standard model version a 19-level hybrid sigma-pressure coordinate system reaching up to a height of 10 hPa is used. The model is based on the primitive equations and calculates vorticity, divergence, temperature, (logarithm of) surface pressure, humidity and cloud water content (ice and water phase) as prognostic variables.
ECHAM5 is the successor of ECHAM4 (*Roeckner et al.*, 1996), which has been established as a powerful tool for global climate variability and change simulations (e.g., *Roeckner et al.*, 1996b; *Sausen et al.*, 1997; *Roeckner et al.*, 1999), for climate sensitivity experiments (e.g., *Cubasch et al.*, 1992; *Ponater et al.*, 1994; *Feichter et al.*, 1997; *Lohmann and Feichter*, 1997), for tracer transport studies (e.g., *Kjellström et al.*, 1999a; *Timmreck et al.*, 1999; *Kjellström et al.*, 1999b) and for chemistry-climate applications (*Roelofs and Lelieveld*, 1995, 2000).
Compared to the previous version, ECHAM4, a number of changes have been introduced. This includes a flux-form semi-lagrangian transport scheme for positive definite variables like water components and chemical tracers, a new longwave radiation scheme, separate prognostic equations for cloud liquid water and cloud ice, a prognostic-statistical cloud cover parameterization, a new cloud microphysical scheme, and a change of the representation of land surface processes. A detailed description of ECHAM5 and the changes compared to ECHAM4 is given in *Roeckner et al.* (2003).

6.2.1 Newtonian relaxation

For all studies a four-dimensional assimilation technique (nudging) is used to relax the ECHAM5 model atmosphere towards an observed state, in this case ECMWF analysis data. Originally, this technique was used to improve numerical weather prediction by nudging the model towards observations during a spin-up period, after which the model produced a prediction. Nowadays, nudging is a very useful technique for validation of cloud and chemistry schemes in General

Circulation Models (GCMs) for which long time series of measurements are not available. The technique can be used to adjust the ECHAM5 model towards actual meteorological conditions for a longer period of time. Observations made during that period, for example during an atmospheric chemistry measurement campaign, can then be directly compared with the model. A more detailed description of this nudging procedure, applied in the ECHAM4 model, is given by *Jeuken et al.* (1996).
Essentially, the model is nudged toward the observed state by adding a non-physical tendency to the overall tendency of a prognostic model variable:

$$\frac{dX}{dt} = F_m(X) + G(X)[X_{obs} - X] \tag{6.1}$$

where X can be any prognostic variable (in this study we nudge surface pressure, divergence, vorticity, and temperature). F_m(X) is the model forcing for variable X, G(X) the relaxation coefficient (s^{-1}), and [X_{obs}-X] the difference between model and the observations. To some extent, the relaxation coefficient G can be chosen freely. However, if G is too small, the model will not be influenced by the observations. On the other hand, if G is chosen too large, the model may deviate too far from its own balanced state, leading to artificial responses to these unbalanced tendencies.
The prognostic variables are relaxed toward the operational ECMWF data, which are produced for weather forecasting purposes. Horizontally, the data from ECMWF from its original resolution of T159 is truncated to the resolution of the different runs. Finally, the ECMWF data, which are available on a 6-hourly basis, were interpolated in time to match ECHAM5/MESSy's time steps. The spin-up time for the nudged model to reach a balanced state corresponding to a particular meteorological episode has been shown to be at most a few days (*Jeuken et al.*, 1996). However, it is emphasized that this simple Newtonian relaxation technique is not used for forecasting purposes, for which more sophisticated data assimilation methods are available, but rather to "nudge" the model towards the actual meteorological conditions, while allowing the model to internally consistently simulate the atmospheric conditions.

6.3 MESSy - the Modular Earth Submodel System

The lagrangian transport model ATTILA has been coupled via the MESSy interface to ECHAM5. MESSy, the "**M**odular **E**arth **S**ubmodel **Sy**stem" provides a generalized interface structure, which allows unique new possibilities to study feedback mechanisms between various bio-geo-chemical processes. Data are exchanged between a base model, in this case ECHAM5, and several submodels within one comprehensive model, whereby the internal complexity of the submodels is controllable in a transparent and user friendly way. A detailed description of MESSy is given by *Jöckel and Sander* (2004).

6.4 Comparison of trajectories

To determine the influence of the horizontal resolution of ECHAM5/MESSy on the ATTILA trajectories, the resolution-sensitivity of the trajectories has to be tested.
A measure for the differences between single trajectories is the absolute horizontal and vertical transport displacement, adopted by many authors in recent years (e.g., *Kuo et al.*, 1985; *Rolph*

and Draxler, 1990). The absolute horizontal transport deviation (AHTD) at the time step t is the spherical distance (in kilometers) between the calculated discrete points of two trajectories starting at the same location, while the absolute vertical transport deviation (AVTD) (in hPa) only considers their pressure difference.

$$ATEH(t) = \frac{1}{N}\sum_{n=1}^{N}\{[x_1^n(t) - x_2^n(t)]^2 + [y_1^n(t) - y_2^n(t)]^2\}^{0.5} \tag{6.2}$$

$$ATEV(t) = \frac{1}{N}\sum_{n=1}^{N}([p_1^n(t) - p_2^n(t)]) \tag{6.3}$$

N is the total number of trajectories compared, $x_1^n(t)$ and $y_1^n(t)$ are the grid locations of the reverence trajectories at travel time t, $x_2^n(t)$, $y_2^n(t)$ are the locations of the trajectories to be compared to, and $p_1^n(t)$ and $p_2^n(t)$ are the corresponding pressure locations.
However, the absolute spherical distance can be a poor measure for the comparison of a pair of trajectories. This becomes clear in Figure 6.1, which shows for two situations a pair of trajectories with identical initialization position and time projected on the horizontal plane. In both cases the spherical distance is small, whereas the difference between the two trajectories in case 1 is small, in contrast to case 2 on the right hand side. To avoid misleading interpretations, a sensitivity parameter s is additionally introduced following *Scheele et al.* (1996).
The parameter s is defined as the maximum of two distinct expressions for the difference between the trajectories calculated at different resolutions:

a) The relative spherical distance RSD, which is the absolute spherical distance between the endpoints of the two trajectories (points A and B in Figure 6.1) at time step t, as introduced in equation (6.2), normalized by the mean length of the two trajectories;

$$RSD(t) = \frac{ATEH(t)}{(dist1(t) + dist2(t)) * 0.5} \tag{6.4}$$

with dist1(t) and dist2(t) the length of both trajectories at time step t.
b) The relative length difference RLD is the absolute difference in length between the two trajectories, normalized by the mean length of the two trajectories, whereby length means the distance of the trajectories projected onto the earth's surface.

$$RLD(t) = \frac{ABS(dist1(t) + dist2(t))}{(dist1(t) + dist(2(t)) * 0.5)} \tag{6.5}$$

In general, the value of parameter s indicates the level of agreement between the trajectories.

6.5 The lagrangian transport scheme ATTILA

This section gives a short overview of the lagrangian transport scheme ATTILA, originally developed at the Institute of Atmospheric Physics, DLR, Oberpfaffenhofen, Germany.

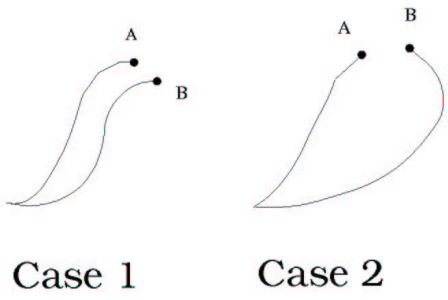

Figure 6.1: Schematic examples of trajectories, starting at the same position and time, with different paths. Although in both cases the endpoints of the two trajectories are close, the paths deviate substantially.

Within the scope of this thesis, ATTILA has been separated from ECHAM4, translated to Fortran90, written in modularized form and coupled via the MESSy interface (section 6.3) to ECHAM5.
Compared to the original version, a few changes have been introduced. The convective tracer transport, which was treated semi-lagrangian, has been replaced by a full-lagrangian convection routine, which changes the position of the air parcels being affected by convective transport. However, the accuracy of this routine has still to be extensively tested and therefore will not be the subject of this thesis. Further developments are the independent choice of the number of air parcels either representing the entire model atmosphere or being initialized at independently selectable points and dates.
The treatment of subscale turbulence and turbulence in the planetary boundary layer has remained unchanged. Therefore, merely a basic description of ATTILA's functionality is given in this section. For a detailed description it is referred to *Reithmeier* (2001) and *Reithmeier and Sausen* (2000).

6.5.1 Atmospheric mode

The model ATTILA has been developed to treat the global-scale transport of passive trace species in the atmosphere within the framework of a general circulation model. The number of air parcels dividing the model atmosphere can either be chosen independently by the users or be linked to the ECHAM5/MESSy resolution. In the latter case, the model atmosphere is divided into about 83000 (at T21 resolution and 19 model levels) or 1400000 (at T63 resolution and 39 layers) air parcels of constant mass. The absolute number of air parcels per grid box is proportional to the mass of each box.
In case of lagrangian tracer transport each trace constituent is represented by a mass mixing ratio in each parcel. However, air parcels can also be transported without having physical properties. In that case, ATTILA acts as a pure forward trajectory model.

Horizontal coordinate system	Latitude/Longitude
Vertical coordinate system	hybrid terrain following and pressure σ-p
Spatial Resolution	depending on ECHAM5/MESSy (T21 - T159)
Time Resolution	depending on ECHAM5/MESSy (T21 - T159)
Integration method	Runge-Kutta 4th order
Horizontal interpolation	linear
Vertical interpolation	cubic-hermite

Table 6.1: Summary of the general features of the lagrangian transport model ATTILA

6.5.2 Trajectory mode

In addition to the *atmospheric mode*, a second mode was added to the original code.
In the so called *trajectory mode*, initialization points (latitude, longitude and pressure height) as well as initialization times can be defined for air parcels being independent of the ECHAM5 resolution. If the users' focus is on the accurate description of a multi-day transport episode from a point source or even a large area source, the *trajectory mode* provides a useful alternative to the *atmospheric mode*, demanding less computer resources. However, in the *trajectory mode* the assumption of having equal mass for each parcel is not valid and ATTILA acts as a pure forward trajectory model.

6.5.3 Advection

At every ECHAM5/MESSy time step the centroid of each parcel, running either in the *atmospheric mode* or in the *trajectory mode*, is advected using the computed three-dimensional wind field. Depending on the spatial resolution of ECHAM5/MESSy, wind data is available about every 40 minutes (T21 with 19 layers) to 3 minutes (T159 with 31 layers).
The trajectory equation (equation (2.1)) is solved by using the fourth-order Runge-Kutta method (see appendix A). In contrast to off-line trajectory models, applying archived data with a temporal resolution of three or six hours, there is no need for temporal interpolation of the wind fields. The horizontal interpolation of the gridded wind data to the positions of the air parcels is linear, in the vertical it is cubic-hermite (see appendix B).
The general features of ATTILA are summarized in Table 6.1.

6.6 ATTILA in ECHAM5/MESSy

6.6.1 Simulation of a Warm Conveyor Belt over the Atlantic Ocean

For the validation of the accurate coupling of ATTILA to ECHAM5/MESSy and the simultaneous evaluation of the transport characteristics, a meteorological situation was selected that may be considered as difficult for trajectory models, namely strong ascent within a Warm Conveyor Belt ahead of a cold front (*Stohl and Trickl*, 1999).
Aircraft measurements over the Atlantic Ocean showed that boundary layer air was uplifted to at least 238 hPa at 0100 UTC on 28 May. The measurements and the synoptic situation during this event have been discussed extensively by *Stohl and Trickl* (1999). A total of 671 48-hour forward trajectories were started at 950 hPa and 850 hPa on a 1° x 1° grid within the region

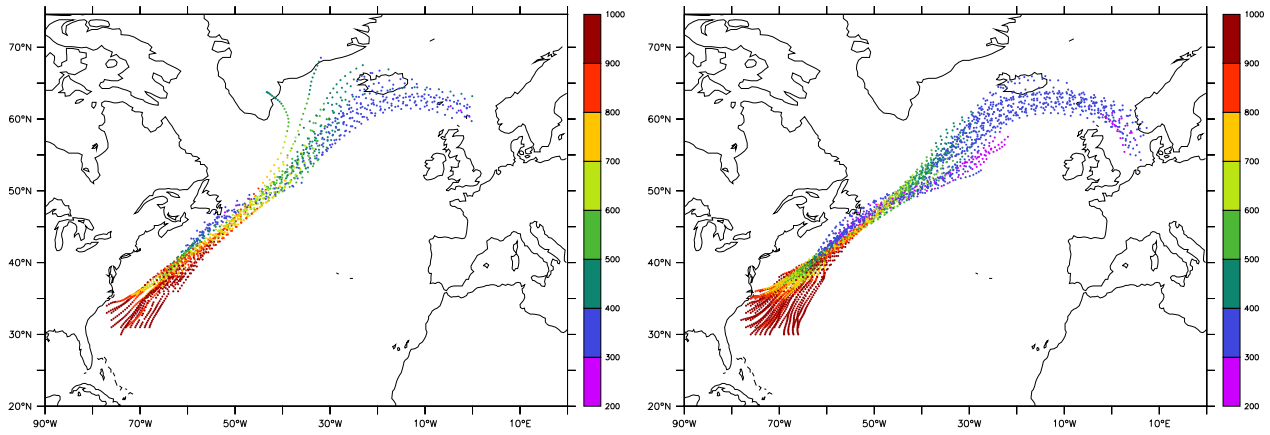

(a) (b)

Figure 6.2: Transport-pressure height spectrum in hPa of the trajectories within the Warm Conveyor Belt calculated by a) ATTILA and b) the FLEXTRA model.

80° W to 60° W and 251° N to 40° N at 1800 UTC on 26 May 1997, covering the entrance region of the Warm Conveyor Belt.

For investigations of the air mass transport with ATTILA, the simulation is compared with the results of the FLEXTRA trajectory model, driven by ECMWF wind analysis with a horizontal resolution of 1° x 1° and 31 vertical layers reaching up to a height of 10 hPa. The temporal resolution of the wind data was 6 hours.

The horizontal resolution of ECHAM5/MESSy was T106 (about 1.125° x 1.125°), and therefore comparable to the ECMWF analyzed wind fields used by the FLEXTRA model. At this relatively high resolution (from a global perspective), the air parcels in ATTILA were advected each 6 minutes by the three-dimensional wind field calculated by the climate-chemistry model ECHAM5/MESSy. The vertical resolution was identical to the ECMWF analysis data.

In Figure 6.2 the results of ATTILA and FLEXTRA are depicted. In both cases, only the trajectories were plotted that ascended more than 600 hPa, the typical ascent of a Warm Conveyor Belt (*Stohl and Trickl*, 1999). The ATTILA model simulated 38, while FLEXTRA simulated 64 trajectories ascending by more than 600 hPa (Table 6.2). Both models suggest the same air travel pathways, connecting the east coast of North America with Northern Europe. Both, the overall average travel distance on the sphere and the overall average pressure range between the starting and the ending points of the ATTILA trajectories (2152 km and 237 hPa) are somewhat less compared to the FLEXTRA trajectories (2337 km and 270 hPa). Since the general motion within the Warm Conveyor Belt is upward, ATTILA appears to simulate weaker ascent than FLEXTRA. While five FLEXTRA trajectories reached 238 hPa, the flight level of the aircraft (see *Stohl and Trickl* (1999)), no ATTILA trajectory reached that pressure height. The 251 hPa level was the maximum level reached by an ATTILA trajectory.

Nevertheless, this comparison clearly shows that synoptic-scale events can be simulated quite accurately with ATTILA. In essence the differences with the FLEXTRA model can be associated to the computed wind fields that drive ATTILA and the FLEXTRA model as well as interpolations in time. While FLEXTRA is an off-line model, driven by ECMWF archived wind data,

	ATTILA	FLEXTRA
average horizontal travel distance (km)	2140	2337
average vertical travel distance (hPa)	237	270
number of traj. ascending > 600 hPa	38	64
number of traj. ascending > 500 hPa	131	184
highest level reached (hPa)	251	225

Table 6.2: Summary of the transport characteristics of the simulation of the Warm Conveyor Belt of ATTILA and FLEXTRA trajectories.

the air parcels in ATTILA are transported by the ECHAM5/MESSy flow, calculated each time step. Even though running in the nudging mode and therefore being relaxed towards an observed state, the calculated ECHAM5/MESSy wind fields cannot be identical to those of the ECMWF analysis. Therefore, the comparison of single trajectories demonstrates differences in the nudged version of ECHAM5/MESSy with the original ECMWF data rather than differences between the results of ATTILA and FLEXTRA.

6.6.2 Indian monsoon trajectories

The second study refers to the Asian monsoon outflow during summer. Investigations of the MINOS campaign with back trajectories (chapter 4) and model simulations (*Lawrence et al.*, 2003; *Roelofs et al.*, 2003) indicate that the upper troposphere was dominated by southeasterly flow originating over India and southeast Asia during the first half of August 2001. Travel times of 2 to 7 days for deep convection from the boundary layer to the upper troposphere over India and furthermore about 8 days from South Asia towards the eastern Mediterranean in the upper troposphere (section 4.5.4), resulting in overall about 10 to 15 days travel time, are in good agreement with the estimated "chemical age" of the Asian monsoon outflow measured during the MINOS campaign over the eastern Mediterranean by *Scheeren et al.* (2003).
This test set consisted of 240 15 day trajectories started on a 1° x 1° grid within the region 70° W to 85° W and 10° N to 24° N twice a day (7 and 19 UTC) close to the surface (900 hPa) during July 2001. The horizontal resolution of ECHAM5/MESSy was T63 with 31 vertical levels. In addition to the validation of the strong vertical transport within the Indian monsoon, the travel times from the Indian boundary layer into the upper-level eastern Mediterranean are investigated and compared to the above mentioned results.
Figure 6.3 shows a selection of the trajectories simulated with ATTILA, initialized in the Indian boundary layer and transported after rapid ascent in the monsoon convection to the upper troposphere towards the eastern Mediterranean. The travel time from the boundary layer to the upper troposphere at about 200 hPa is about 2 to 6 days. After an additional 6 to 8 days the trajectories are transported to the eastern Mediterranean region, resulting in an overall travel time of about 8 to 14 days from the Indian boundary layer into the eastern Mediterranean. This travel time is in good agreement with that found by trajectory calculations with the FLEXTRA model (presented in section 4.5.4) and the estimate of the chemical age of Asian air pollution by *Scheeren et al.* (2003).

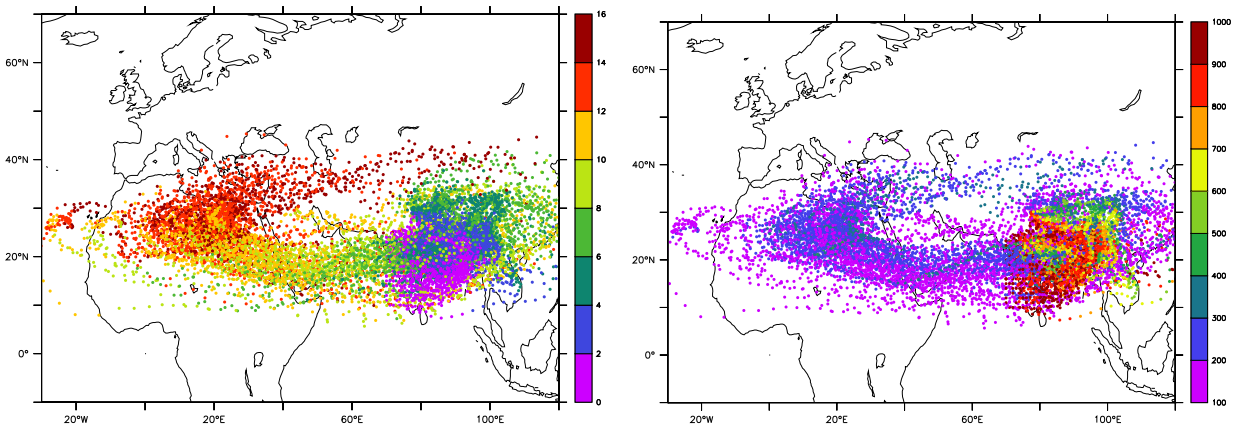

(a) (b)

Figure 6.3: a) Travel-time spectrum in units of days, and b) transport-pressure height spectrum in units of hPa of ATTILA trajectories, initialized in the Indian boundary layer and transported within the Indian monsoon towards the Mediterranean region in the upper tropospheric anticyclonic flow.

6.6.3 Influence of the ECHAM5/MESSy resolution on the ATTILA trajectories

Sections 6.6.1 and 6.6.2 imply that the coupling of the lagrangian transport model ATTILA and ECHAM5/MESSy has been successful. Additionally, the capability of ATTILA in combination with ECHAM5/MESSy to simulate air flows in synoptic-scale weather systems on the time scale of a few days with realistic travel times is demonstrated based on a case study.
Driven by the three-dimensional wind fields, calculated by the chemistry-climate model, the accuracy of the ATTILA transport calculations depends on the quality of the wind fields simulated by ECHAM5/MESSy. Numerical errors, which arise from the finite resolution of the model, will decrease with increased resolution, and consequently an improved performance may be expected. Furthermore, finer wind field structures are simulated by increasing the horizontal resolution, involving a reduction of the interpolation error of the wind field to the actual trajectory positions. *Stohl et al.* (1995) found a large sensitivity to this type of interpolation errors for trajectories in complex flow situations. Since ATTILA is directly coupled to ECHAM5/MESSy, so that no interpolation is done over 3 or 6-hourly wind data, it may be expected that such errors are limited in the setup.
To determine the influence of changes of the horizontal resolution on the transport paths of ATTILA, the calculation of 48-hour forward trajectories was performed four times while running ECHAM5/MESSy at different horizontal resolutions (T159, T106, T63, T42) with grid box sizes between about 83 and 307 km (see Table 6.3) and 31 vertical levels.
For this study the meteorological situation illustrated in Figure 6.4 was chosen. A low pressure trough was located over Central Europe, between the Azores High over the Atlantic Ocean and a high pressure system over Russia. A low pressure system, developing on 16 July over western Britain, moved towards the North Sea on 19 July, generating a strong divergent wind field over the Atlantic, with anticyclonic flow caused by the Azores high and northeastward flow nearby

resolution	degrees	distance
T159	0.75°	83 km
T106	1.11°	124 km
T63	1.88°	209 km
T42	2.77°	307 km

Table 6.3: Approximate grid box sizes of the horizontal resolutions of the different simulations.

within the warm front of the low pressure system.

The simulation started at 00 UTC on 16 July 2001, while the 1296 48-hour forward trajectories were initialized at 900 hPa, 500 hPa and 300 hPa on a 1° x 1° grid within the region 32° to 58° N and 20° to 5° W at 00 UTC on 17 July 2001.

For this study the boundary layer turbulence in ATTILA, simulated by vertical mixing and stochastical repositioning of each air parcel within the layer at each time step (*Reithmeier and Sausen*, 2000), was switched off.

Comparison of the results shows that at each height level all major transport paths are similarly simulated at the four different resolutions. At the lowest level (Figure 6.5) cyclonic flow with vertical transport at about 50° N and mainly anticyclonic flow south of 45° N is discerned. In the following, at the lowest level the flow field north of 45° N and in the middle and upper troposphere north of 48° N is designated as *cyclonic* and south of 45° N respectively 48° N *anticyclonic*. Eastward transport over northern Africa is also simulated nearly equally at all resolutions, whereas the vertical transport differs strongly in the different experiments. Average travel distances, however, both north and south of 45°, differs only slightly (Table 6.4). While the differences in average pressure height are maximum 18 hPa in the anticyclonic circulation, the maximum deviation north of 45° is 30 hPa. Differences in minimum pressure height values in the cyclonic circulation are relatively small (up to 55 hPa), while the maximum difference south of 45° is about 200 hPa. In contrast, maximum pressure height differences of about 14 hPa are obtained for the anticyclonic and about 60 hPa for the cyclonic circulation.

At 500 hPa the influence of the trough on the trajectories is still strong, while south of 48° N the air is transported to the Mediterranean region, with some trajectories descending over the eastern Mediterranean to about 750 hPa (Figure 6.6). However, in contrast to the simulation at T42, T106 and T159 resolution at T63 less upward transport is simulated at about 0° to 10° E and 33° to 36° N, resulting in about 260 km shorter average travel distance than at T42, T106 and T159 resolution. Additionally, the few trajectories in northeasterly direction south of Ireland are simulated at T63 only. The small differences in average travel distance (2 km) and pressure ending height (1 hPa) at T106 and T159 in the cyclonic circulation are remarkable (Table 6.5). In both circulations, minimum pressure height values are simulated at T159, with maximum differences in the anticyclonic circulation of about 180 hPa.

The main travel direction towards the east is maintained at the lower latitudes in the upper troposphere, with associated downward transport over the eastern Mediterranean and the Arabian Peninsula at all resolutions. Nevertheless, the average travel distance at T63 is about 400 km shorter than at other horizontal resolutions. The upper troposphere north of 48° N is dominated by a large cluster of trajectories with center over Ireland, approximately reaching the coast of Norway. Some disagreement in position occurs by the simulation of clusters containing only a few trajectories at T42 and T63 relative to T106 and T159, which move northward after crossing

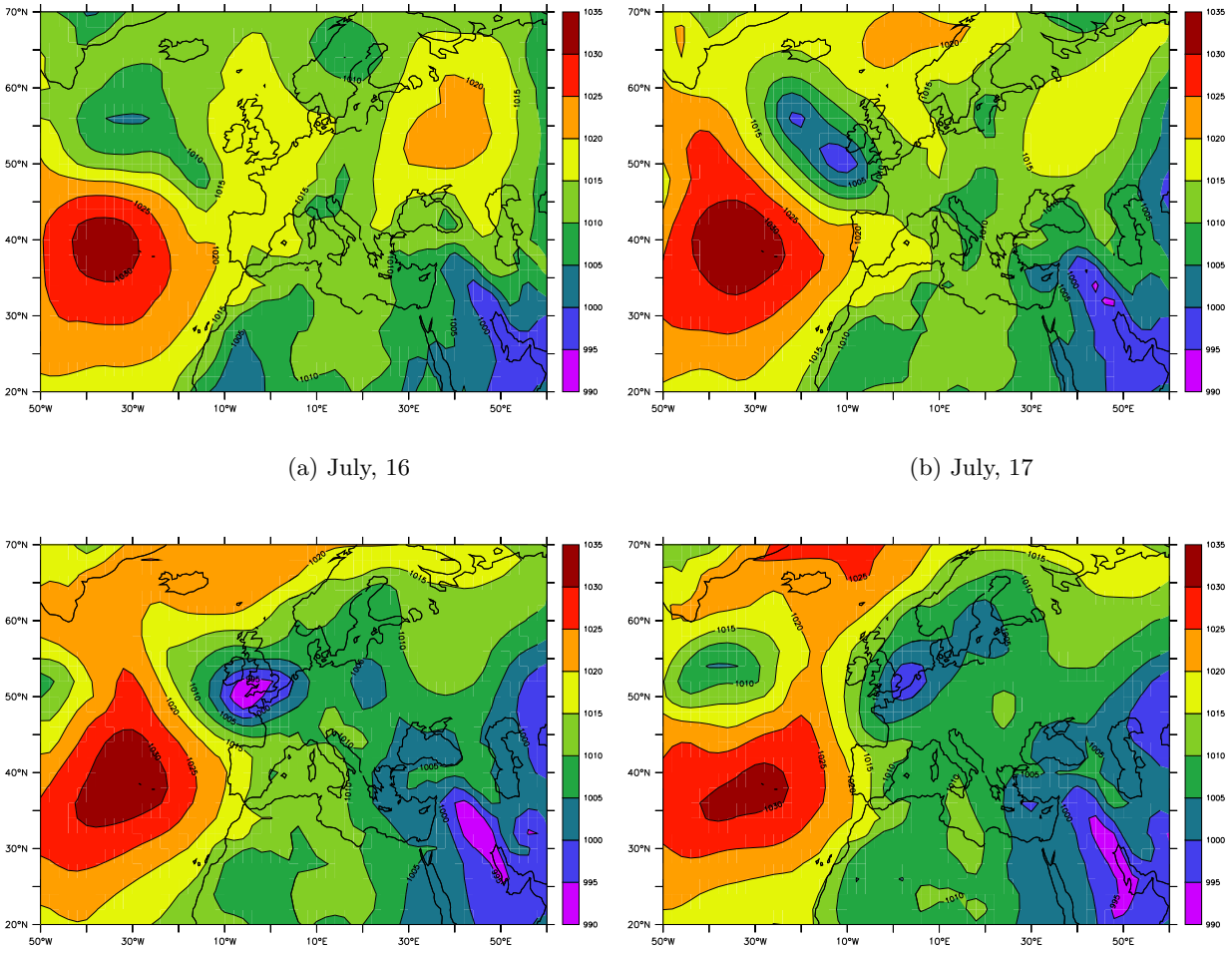

(a) July, 16

(b) July, 17

(c) July, 18

(d) July, 19

Figure 6.4: Surface pressure in hPa on a) July 16, 2001, b) July 17, c) July 18 and d) July 19.

central Europe eastward (Figure 6.7). Relatively small differences with respect to minimum and maximum pressure height values of the trajectories in both circulations compared to the deviations in the boundary layer are associated with lower overall vertical transport in the free and upper troposphere as compared to the surface.

For further analysis, the sensitivity parameter s introduced in Section 6.4 and vertical transport deviations of the trajectories at the different horizontal resolutions after 48 hours, depending on the initialization pressure height, are calculated. To obtain an idea of the absolute deviations of the ending points of the trajectories after 48 hours, the absolute horizontal transport deviations are additionally calculated. The sensitivity parameter s, AVDT and AHDT give information about the differences of a pair of trajectories with identical initialization positions calculated at different horizontal resolutions, while the information gathered from Table 6.4 mostly applies to the trajectory clusters.

For the comparison of the calculated trajectories it is assumed that the transport paths of the air parcels are simulated most accurately at T159. Therefore, the sensitivity parameter s, average horizontal and vertical distances for T42, T63 and T106 are calculated relative to T159 and

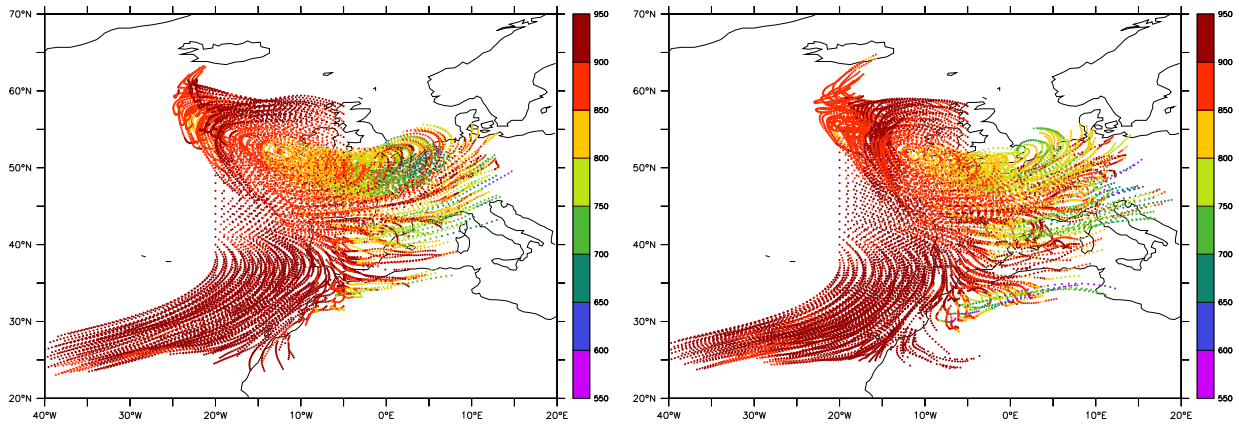

(a) T42 (b) T63

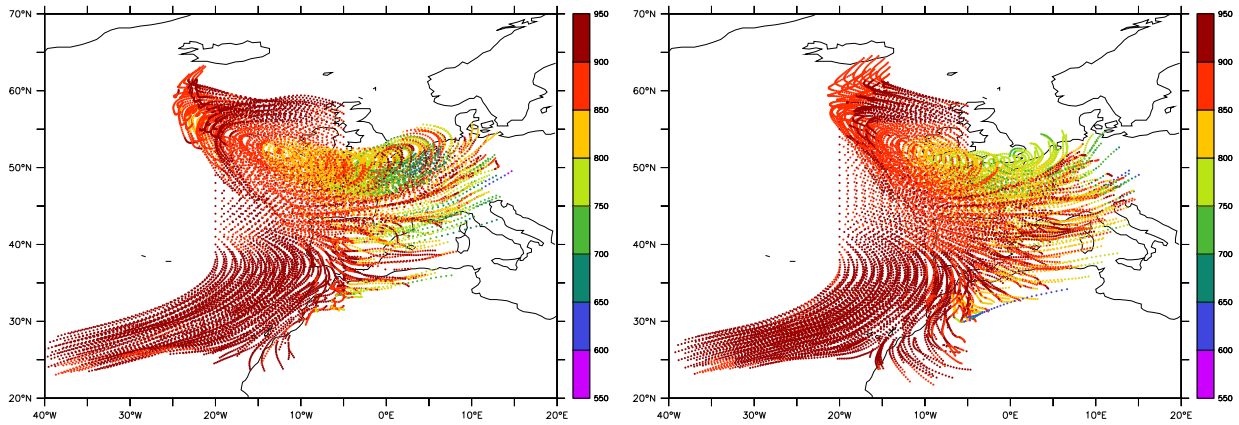

(c) T106 (d) T159

Figure 6.5: Transport-pressure height spectrum in units of hPa of the ATTILA trajectories with 900 hPa initialization height simulated at a) T42, b) T63, c) T106 and d) T159 horizontal resolution.

summarized in Table 6.5. Furthermore, we distinguish between the cyclonic and the anticyclonic air flow. As expected it appears that the trajectories calculated at T106 agree best with those calculated at T159, which is indicated by maximum average values of 0.14 for the sensitivity parameter and average vertical transport deviations of maximum 2 hPa. The average horizontal transport deviations are up to 200 km and therefore within the size range of 1 to 2 grid boxes (see Table 6.3).

The parameter s increases for the T42 and T63 simulations, indicating increasing differences of the trajectories compared to T159. At T42, maximum horizontal transport deviations are close to 900 km after 48 hours. The slightly better agreement between T42 and the T159 reference simulations than between T63 and T159 in the anticyclonic circulation is remarkable. However, differences both in pressure and horizontal deviations are systematically larger than at T106.

Positive average vertical transport deviations of about 30 hPa at T42 and T63 are largest in the cyclonic circulation near the surface, indicating stronger vertical transport than at higher

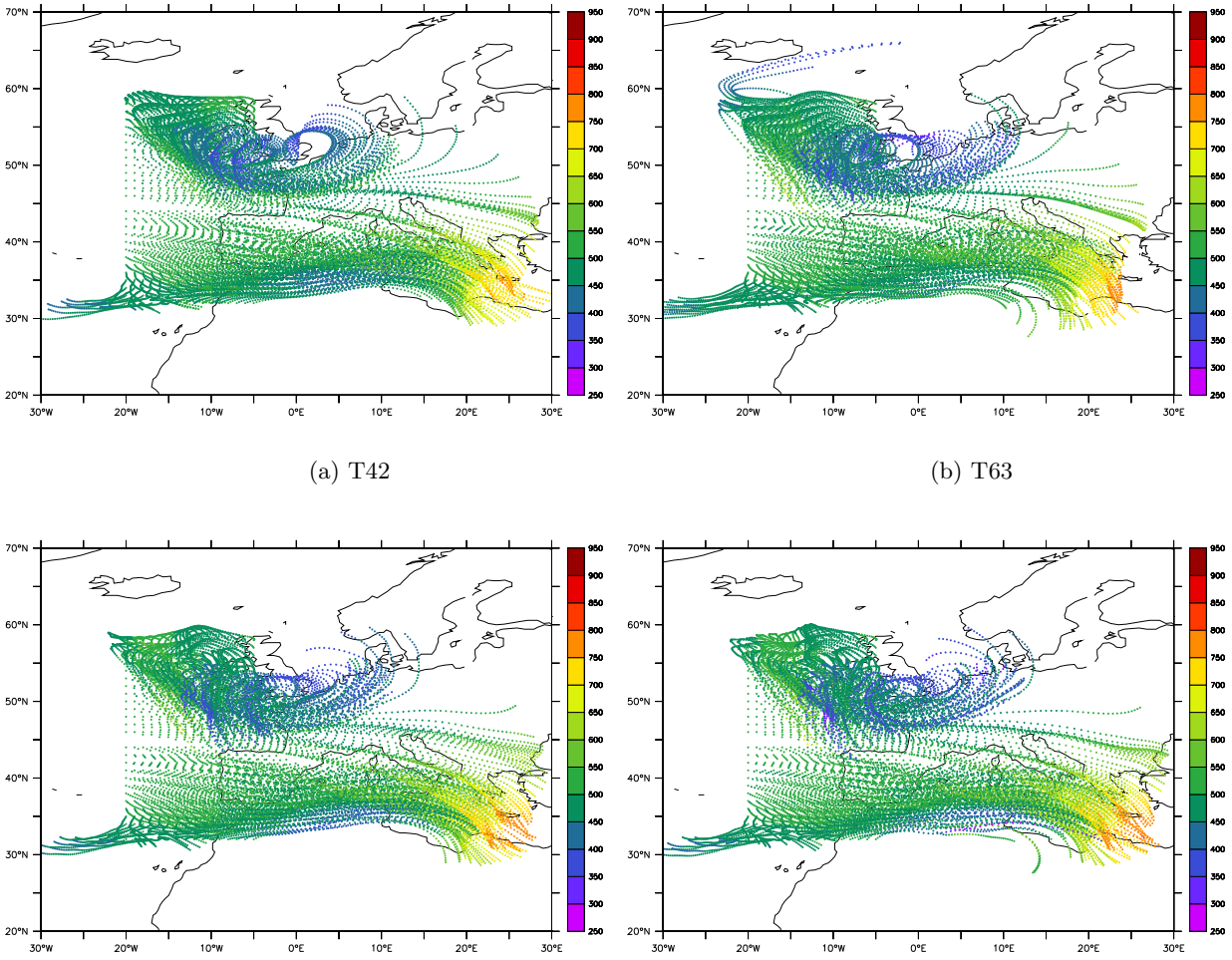

(a) T42 (b) T63

(c) T106 (d) T159

Figure 6.6: Transport-pressure height spectrum in units of hPa of the ATTILA trajectories with 500 hPa initialization height simulated at a) T42, b) T63, c) T106 and d) T159 horizontal resolution.

horizontal resolutions, while in the anticyclonic circulation negative vertical transport deviations imply less vertical transport. The large differences in AVDT and as a consequence in AHDT at low horizontal resolutions are illustrated in Figure 6.8, which shows the vertical velocity in hPa/h at T42 and T106 near the surface. Areas with both upward and downward transport differ in intensity, position and shape depending on the horizontal resolution. At T42, for instance, a large area with upward transport of about 3 hPa/h extends from about 8° W and 47° N eastward across the north of Germany, with an area of maximum vertical velocity in the region of the low pressure system from about 0° to 6° E and 52° N with about 5 hPa/h. At T106 this is different; two areas with maximum upward velocities of about 7 hPa/h over France and the North Sea with a minimum of about only 1 hPa/h between are simulated.
In contrast to the T42 simulation, downward velocities over the southwest of Britain of about 1 hPa/h occur. The differences in the intensity and position of the synoptic weather systems are much more pronounced, with enhanced vertical velocity in the South of Europe and over

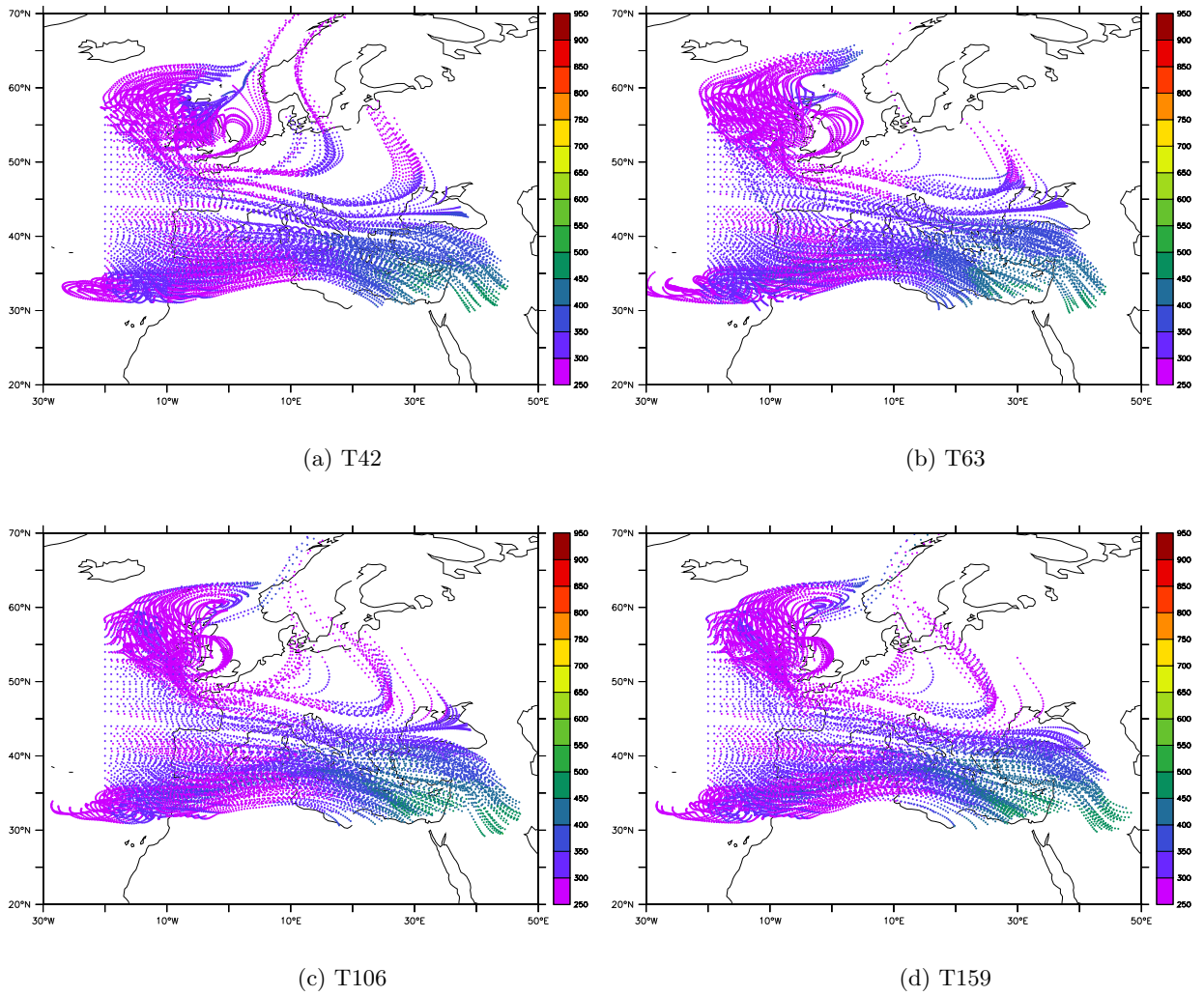

(a) T42

(b) T63

(c) T106

(d) T159

Figure 6.7: Transport-pressure height spectrum in units of hPa of the ATTILA trajectories with 300 hPa initialization height simulated at a) T42, b) T63, c) T106 and d) T159 horizontal resolution.

North Africa. These differences are associated with the structure of the simulated horizontal wind field at the different resolutions, because the vertical velocity is related to the divergence of the horizontal wind. A finer structured horizontal wind field therefore will cause finer structured areas with vertical motions. In general, larger differences near the surface than at 500 hPa at all resolutions indicate the complexity of the wind field at high pressure height (especially in the cyclonic circulation) and the need for relatively high horizontal resolution to resolve fine structures.

Increased AHDT and decreased AVDT values from the middle and to the upper troposphere are associated with lower absolute vertical and higher horizontal velocities.

The temporal development of the sensitivity parameter s for a pair of trajectories illustrates clearly that both at T42 and T63 some trajectories are similarly simulated at T159, while many others differ strongly (Figures 6.9, 6.10 and 6.11). Even though there are some substantial differences at T106, the majority of the trajectories shows minor differences in comparison to

resolution	length	ave. pressure height	max. pressure height	min. pressure height
anticyclonic circulation				
900 hPa				
T159	1912 km	862 hPa	997 hPa	522 hPa
T106	1882 km	860 hPa	999 hPa	572 hPa
T63	1859 km	867 hPa	993 hPa	599 hPa
T42	1792 km	878 hPa	983 hPa	715 hPa
500 hPa				
T159	2781 km	604 hPa	802 hPa	257 hPa
T106	2783 km	605 hPa	807 hPa	371 hPa
T63	2520 km	581 hPa	783 hPa	432 hPa
T42	2804 km	596 hPa	803 hPa	404 hPa
300 hPa				
T159	3505 km	391 hPa	510 hPa	243 hPa
T106	3485 km	390 hPa	506 hPa	249 hPa
T63	3071 km	379 hPa	477 hPa	256 hPa
T42	3436 km	383 hPa	502 hPa	259 hPa
cyclonic circulation				
900 hPa				
T159	1636 km	860 hPa	1005 hPa	665 hPa
T106	1612 km	859 hPa	996 hPa	691 hPa
T63	1667 km	830 hPa	955 hPa	660 hPa
T42	1587 km	831 hPa	941 hPa	715 hPa
500 hPa				
T159	1649 km	481 hPa	662 hPa	324 hPa
T106	1691 km	479 hPa	650 hPa	344 hPa
T63	1742 km	477 hPa	649 hPa	348 hPa
T42	1681 km	468 hPa	622 hPa	372 hPa
300 hPa				
T159	1897 km	300 hPa	429 hPa	239 hPa
T106	1831 km	300 hPa	431 hPa	243 hPa
T63	1845 km	303 hPa	449 hPa	241 hPa
T42	1839 km	289 hPa	391 hPa	245 hPa

Table 6.4: Summary of the travel characteristics at the different horizontal resolutions.

T159.
If information on the path of single trajectories is needed, both, that means high AHDT values in the free troposphere and high AVDT values near the surface at coarse horizontal resolutions after just 48 hours, can cause different results at different horizontal resolutions. One example is the calculation of lagrangian mass fluxes through iso-surfaces (e.g. boundary layer, tropopause), which needs information about the number of crossing trajectories. Another example is the analysis of the air mass origin as well as the chemical composition at locations of e.g. cities, ship tracks and aircraft corridors, thus discrete locations with limited horizontal and vertical dimensions. However, as this study shows, there is on the one hand no significant improvement

resolution	s	ATEH	ATEV	s	ATEH	ATEV
anticyclonic circulation				cyclonic circulation		
900 hPa						
T106	0.10	151 km	1 hPa	0.14	193 km	1 hPa
T63	0.29	482 km	-5 hPa	0.48	635 km	30 hPa
T42	0.24	388 km	-16 hPa	0.56	684 km	29 hPa
500 hPa						
T106	> 0.01	70 km	-1 hPa	0.11	148 km	2 hPa
T63	0.21	374 km	23 hPa	0.29	437 km	4 hPa
T42	0.11	222 km	8 hPa	0.29	449 km	13 hPa
300 hPa						
T106	> 0.01	93 km	2 hPa	0.10	146 km	0 hPa
T63	0.24	554 km	12 hPa	0.40	642 km	-3 hPa
T42	0.18	539 km	8 hPa	0.61	881 km	12 hPa

Table 6.5: Absolute horizontal (AHDT) and vertical (ATEV) transport deviations and the average sensitivity parameter s at T106, T63 and T42 compared to T159 horizontal resolution after 48 hours. Negative values of ATEV indicate higher average pressure ending heights than at T159 horizontal resolution.

by increasing the horizontal resolution from T42 to T63, and on the other hand only small differences between the experiments at T106 and T159.

Summarizing, the horizontal resolution of ECHAM5/MESSy and ATTILA in simulating and investigating synoptic scale events should be carefully selected depending on the application. In case of a preliminary survey of the air flows in a large region, ATTILA in combination with a coarse resolution probably provides much of the necessary information. For analyses that require information on the path of single trajectories (e.g., origin of air masses of locations with discrete positions and small horizontal and vertical dimensioning, calculations of air mass fluxes) it is recommended to run ECHAM5/MESSy with ATTILA at relatively high horizontal resolutions, whereas the differences between T106 and T159 are expected to be small.

6.7 Conclusions

This chapter presents first results of the lagrangian transport model ATTILA being coupled to the chemistry-climate model ECHAM5/MESSy. Comparisons with the results of the simulation of a Warm Conveyor Belt over the North Atlantic Ocean with the off-line trajectory model FLEXTRA indicate the successful coupling of ATTILA to ECHAM5 via the MESSY interface, and show the potential of resolving air flows with ATTILA in synoptic-scale events.
Calculated average transport times in summer in the Asian monsoon convection of about 8 to 14 days from the Indian boundary layer to the upper tropospheric eastern Mediterranean are in good agreement with travel times found with the FLEXTRA model and also with estimations of the chemical age of Asian pollution outflow.
Sensitivity runs by changing the horizontal resolution of ECHAM5/MESSy indicate that, depending on the application, the horizontal resolution of ATTILA and ECHAM5/MESSy should be carefully selected. ATTILA in combination with a relatively coarse horizontal resolution

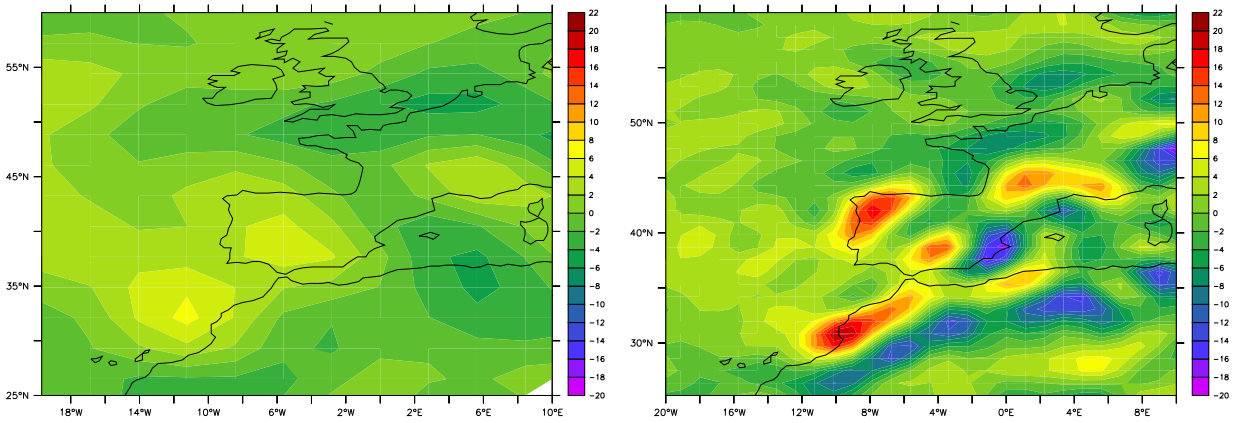

(a) T42 (b) T106

Figure 6.8: Vertical velocity in hPa/h on 18 July 2001 10 UTC at about 850 hPa. Negative values indicate upward, positive values downward motion.

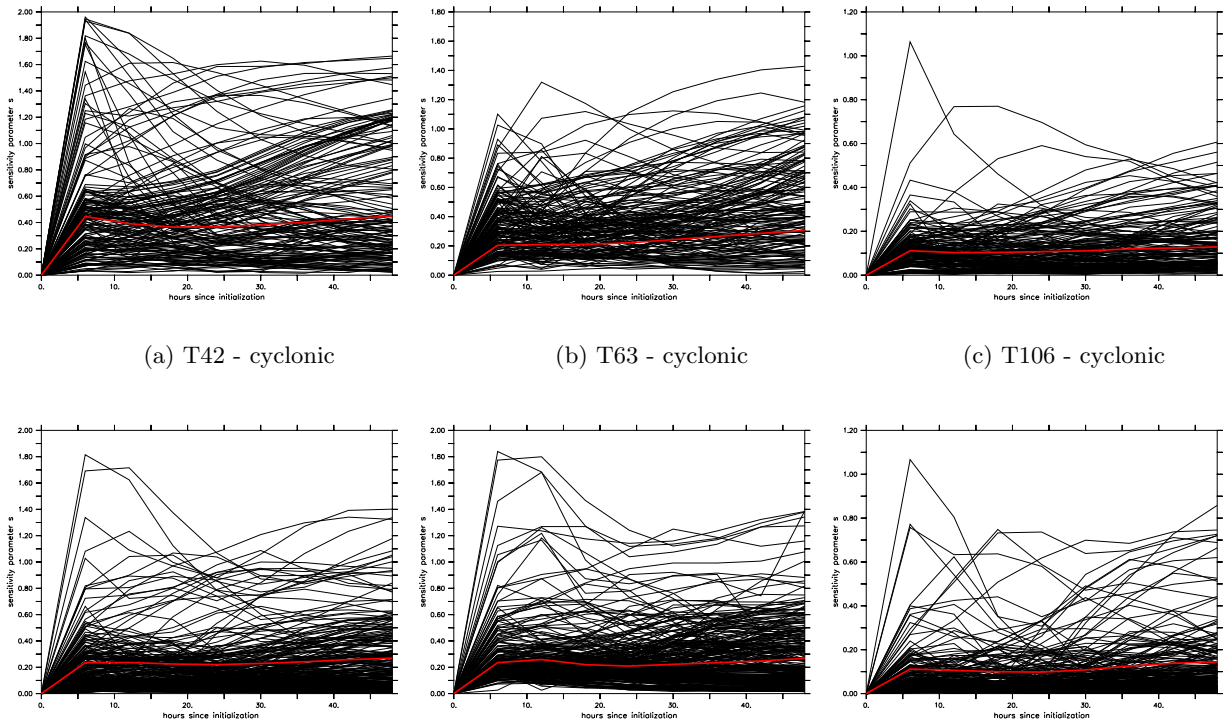

(a) T42 - cyclonic (b) T63 - cyclonic (c) T106 - cyclonic

(d) T42 - anticyclonic (e) T63 - anticyclonic (f) T106 - anticyclonic

Figure 6.9: Temporal development of the sensitivity parameter s at 900 hPa initialization height. The red line denotes the mean.

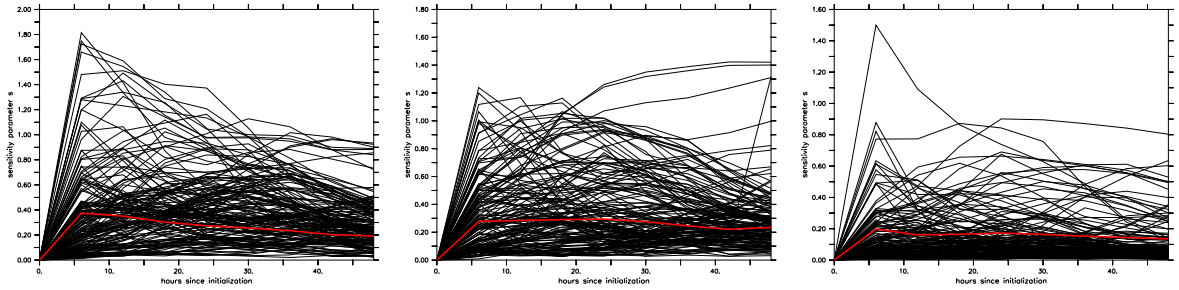

(a) T42 - cyclonic (b) T63 - cyclonic (c) T106 - cyclonic

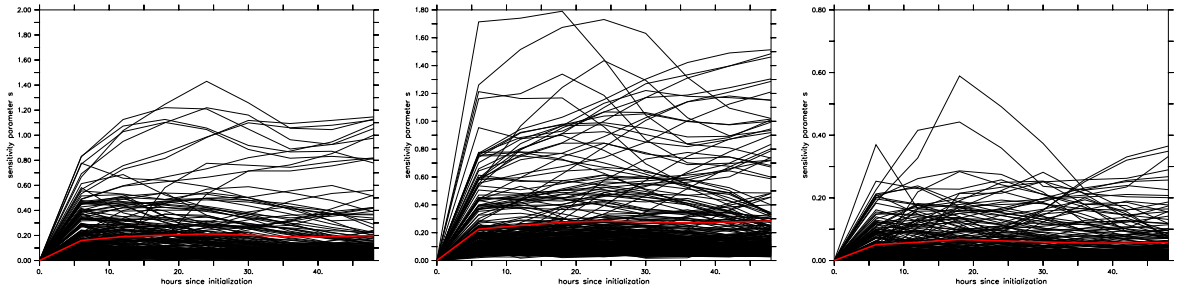

(d) T42 - anticyclonic (e) T63 - anticyclonic (f) T106 - anticyclonic

Figure 6.10: Temporal development of the sensitivity parameter s at 500 hPa initialization height. The red line denotes the mean.

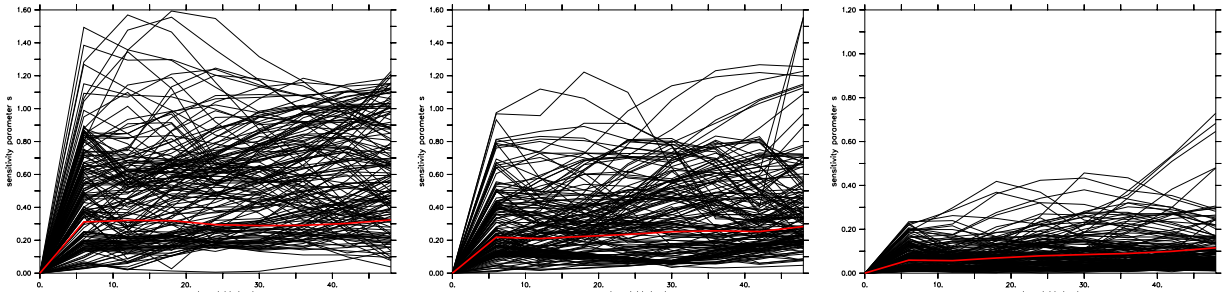

(a) T42 - cyclonic (b) T63 - cyclonic (c) T106 - cyclonic

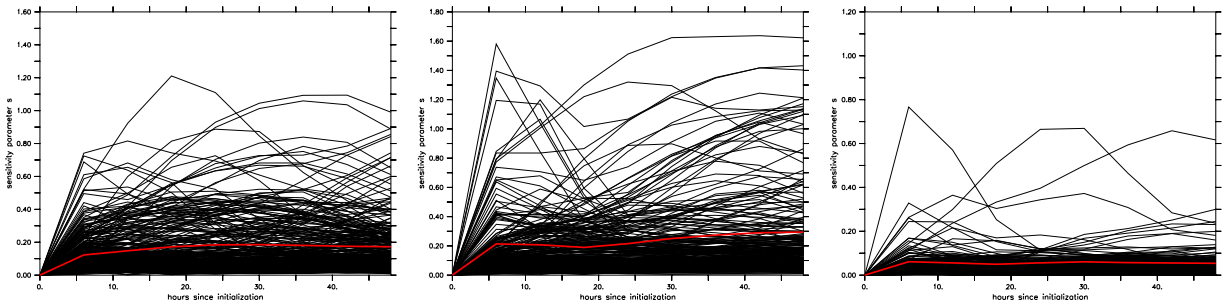

(d) T42 - anticyclonic (e) T63 - anticyclonic (f) T106 - anticyclonic

Figure 6.11: Temporal development of the sensitivity parameter s at 300 hPa initialization height. The red line denotes the mean.

provides much information about the general circulation, both on global and on synoptic scales. For all analyses that require information about single trajectories (e.g., origin of air masses with discrete positions and small horizontal and vertical dimensioning, calculations of mass fluxes) it is recommended to run ECHAM5/MESSy with ATTILA at relatively high horizontal resolutions, whereas the differences between T106 and T159 are expected to be small on time scales of several days.

Chapter 7

Analysis of cross-tropopause transport with ATTILA

Abstract

For the period May to August 2001, mass flux calculations have been performed with the lagrangian transport scheme ATTILA and the chemical-general circulation model ECHAM5/MESSy. It is shown that an extended region from the eastern Mediterranean to the Caspian Sea with enhanced cross-tropopause transport develops in June. This is caused by the intensification of the Arabian and South Asian upper-level anticyclones in summer, associated relatively with high probabilities of clear-air turbulence, confirming the assumption of mixing of tropospheric and stratospheric air near the tropopause during summer in the eastern Mediterranean (chapter 5). Investigation of the residence time on parcels often crossing the tropopause shows that only about 7% of the air resides more than one day and about 4% more than 5 days in its destination sphere. Nevertheless, average residence times of about 5 to 35 days, related to about 4% of the total mass fluxes, suggest the occurrence of deep transport events and enhanced cross-tropopause mixing.

7.1 Introduction

By tracking air parcel transport pathways, the lagrangian approach presented in chapter 6 can be used to calculate mass fluxes across the tropopause, as shown qualitatively in chapter 5. Many estimates of cross-tropopause fluxes are based on hemispheric-scale budgets (*Appenzeller et al.*, 1996b) or on Eulerian diagnostics with the method introduced by *Wei* (1987). However, the Eulerian diagnostics are relatively inaccurate, because of numerical (*Wirth*, 1995*a*; *Wirth and Egger*, 1999; *Gettelman and Sobel*, 2000) and conceptual problems (*Stohl*, 2001). Air parcels, crossing the tropopause twice within a short period are counted both as mass flux from the stratosphere to the troposphere and in the opposite direction, but are in fact not relevant for the total mass exchange. The *Wei* (1987) method is rather inaccurate, especially in quantifying stratosphere-troposphere and troposphere-stratosphere transport, and deriving only the net mass flux.

Although net cross-tropopause fluxes, averaged over extended temporal and spatial scales, may be sufficiently accurate, estimates for instantaneous local cross-tropopause fluxes are quite uncer-

tain (*Kowol-Santen et al.*, 2000), as they are highly sensitive to input data errors such as those that are invariably present in assimilated datasets (*Gettelman and Sobel*, 2000).

In contrast, the lagrangian approach is almost free of numerical problems (*Wirth and Egger*, 1999) and enables the consideration of cross-tropopause transport depth and residence time in either troposphere or stratosphere. For instance, air that returns to the stratosphere after residing only a short time in the troposphere, probably has little opportunity to mix with tropospheric air (*Stohl*, 2001). In addition to climatologies of global cross-tropopause exchange (e.g., *Sprenger and Wernli*, 2003)), individual exchange processes can be resolved and associated to synoptic or mesoscale weather systems, revealing details of the different types of air flows (*Wernli and Davies*, 1997; *Wirth and Egger*, 1999; *Stohl*, 2001; *Wernli and Bourqui*, 2002).
As shown in a qualitative sense in chapter 5 by analyses of forward trajectories for August 2001, the eastern Mediterranean seems to be a region with enhanced cross-tropopause transport relative to the surrounding area during summer. Large-scale synoptic flow systems, the Polar Front Jet and the Arabian and South Asian heat lows, the latter two being quasi-permanent only during summer, form a jet streak, which enters the region at the Subtropical Jet Stream associated with deep tropopause folds. As a result of horizontal and vertical wind shear along that jet streak, clear-air turbulence causes mixing of tropospheric and stratospheric air near the tropopause, mainly at the cyclonic side of the jet axis.
After validation of the successful coupling of ATTILA to ECHAM5/MESSy (chapter 6), here the hypothesis of enhanced cross-tropopause transport over the eastern Mediterranean is quantitatively investigated. The period comprises May to August 2001. The horizontal resolution of ECHAM5/MESSy was T63 with 39 vertical layers and a vertical resolution of about 40 hPa around the tropopause.
After a short description of the method to calculate mass fluxes with a lagrangian model in section 7.2, the idea and the definition of "residence time" is presented in section 7.3. In section 7.4 the monthly averaged upward and downward mass fluxes in the area of interest are presented, followed by an analysis of the relationship of the cross-tropopause fluxes with the upper-level circulation in section 7.5. After discussion of the residence times in troposphere and stratosphere depending on the geographical position of tropopause crossing in section 7.6, the chapter concludes by summarizing the most important statements in section 7.7.

7.2 Calculation of mass fluxes

The model atmosphere in the simulations was divided into 746496 air parcels with a mass of about $6.9{\cdot}10^{12}$ kg[3]. By following each parcel, the air mass flux F_{GB} across an iso-surface per area and time period can be calculated by the number of air parcels N_{AP} crossing that iso-surface multiplied with the mass m_{AP} per air parcel, the inverse of the time step *dtime* and the inverse of the area of that grid box A_{GB}.

$$F_{GB} = \frac{N_{AP} \cdot m_{AP}}{dtime \cdot A_{GB}} \tag{7.1}$$

[3]The mass m_{AP} of an air parcel is calculated by the absolute mass of the atmosphere divided by the number of air parcels. At T63 horizontal resolution $m_{AP} \approx 5.12 \cdot 10^{18}\ kg/\ 746496 \approx 6.87 \cdot 10^{12}\ kg$

7.3 Residence time criterion

The residence time criterion is introduced mainly to eliminate air parcels returning to the stratosphere after residing only a short time in the troposphere or vice versa, assuming that these parcels have little opportunity to mix with ambient air (*Stohl*, 2001). Additionally, numerical errors by calculating the dynamical tropopause height and the air parcel position, which could artificially enhance the mass transport across the tropopause, are excluded.
In this study, cross-tropopause mass fluxes have been calculated for threshold residence times $\tau \geq 24$ and 96 hours following *Wernli and Bourqui* (2002), who designated the 96-hour transport events as "almost irreversible".

7.4 Monthly averaged mass fluxes

Figures 7.1 to 7.3 show the averaged up- and downward mass fluxes across the 3.5 PVU isosurface over the eastern Mediterranean and Caspian Sea at T63 horizontal resolution for the period of May to August 2001. The fluxes are calculated without any residence time limit, with a minimum residence time of $\tau \geq 24$ hours and additionally with a threshold value of $\tau \geq 96$ hours.
Firstly, the geographical distribution of enhanced upward mass fluxes with $\tau \geq 24$ and 96 hours in the eastern Mediterranean in August depicted in Figure 7.4c and Figure 7.4d matches well with the locations of transition from the troposphere to the stratosphere in Figure 5.1, confirming the results of the quantitative investigation of cross-tropopause transport with the FLEXTRA model presented in chapter 5. Additionally, the calculated mass fluxes with $\tau \geq 24$ and 96 hours in the region extending from the eastern Mediterranean to the Caspian Sea for June, July and August are of same magnitude as the mass fluxes presented in the northern hemispheric climatology of cross-tropopause exchange by *Sprenger and Wernli* (2003).
By comparison of the monthly average up- and downward mass fluxes across the dynamical tropopause without a residence times limit in Figures 7.1a and 7.1b to Figures 7.4a and 7.4b, a substantial increase in air crossing the tropopause from May to June, July and August over the eastern Mediterranean appears. While both upward and downward mass fluxes in May are about 400 - 1800 kg s^{-1} km^{-2}, about 2000 to 4000 kg s^{-1} km^{-2} in June, 2000 to 3600 kg s^{-1} km^{-2} in July and about 3000 kg s^{-1} km^{-2} in August are transported from the stratosphere to the troposphere and in the opposite direction. In fact, not only the eastern Mediterranean but a large area up to the Caspian Sea is characterized by enhanced cross-tropopause transport during May, June, July and August. In May, strongest mass fluxes appear in the area over the southeastern Mediterranean reaching to the southwestern part of the Caspian Sea.

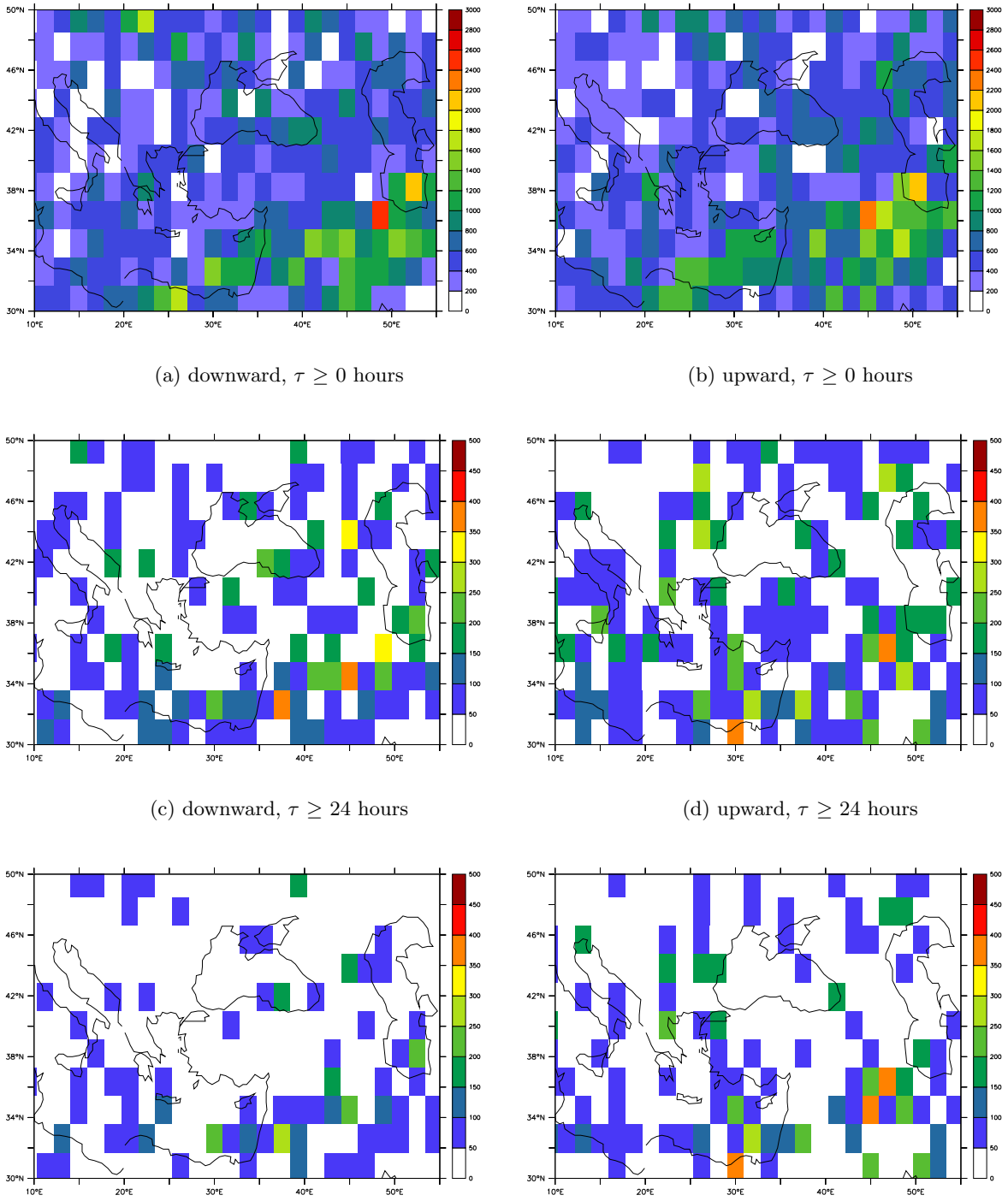

(a) downward, $\tau \geq 0$ hours

(b) upward, $\tau \geq 0$ hours

(c) downward, $\tau \geq 24$ hours

(d) upward, $\tau \geq 24$ hours

(e) downward, $\tau \geq 96$ hours

(f) upward, $\tau \geq 96$ hours

Figure 7.1: Average a) downward, b) upward mass flux without a residence time criterion, c) downward, d) upward mass flux with a residence time $\tau \geq 24$ hours, e) downward and f) upward mass flux with a residence time $\tau \geq 96$ hours in May 2001 at T63 horizontal resolution. Units are kg s^{-1} km^{-2}.

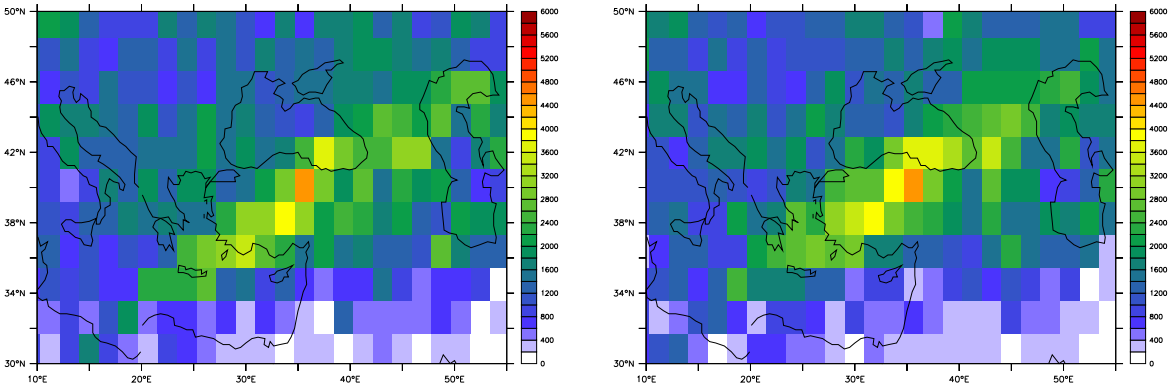

(a) downward, $\tau \geq 0$ hours

(b) upward, $\tau \geq 0$ hours

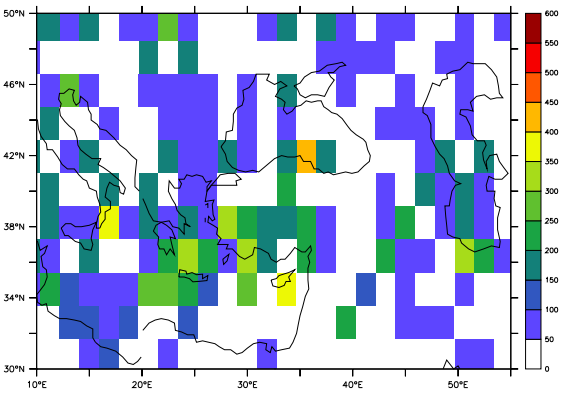

(c) downward, $\tau \geq 24$ hours

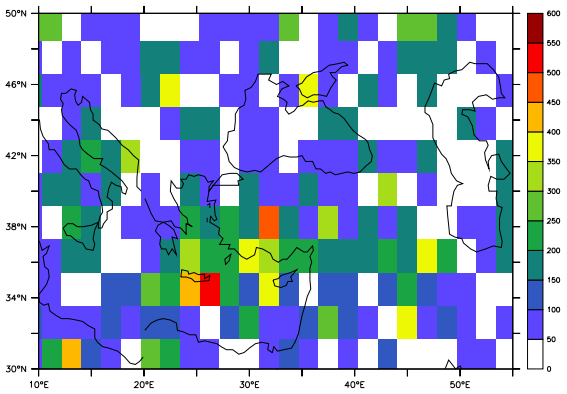

(d) upward, $\tau \geq 24$ hours

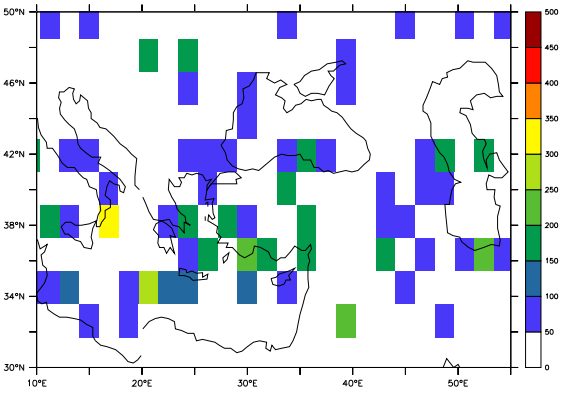

(e) downward, $\tau \geq 96$ hours

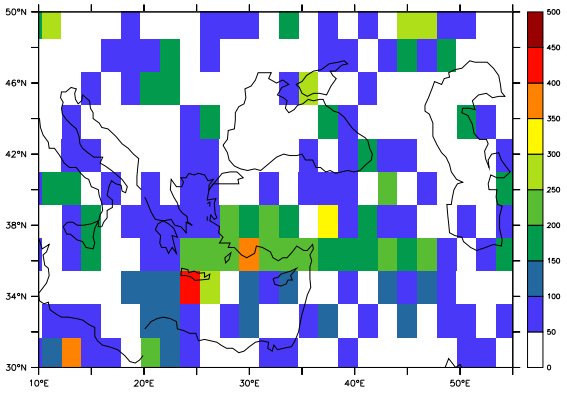

(f) upward, $\tau \geq 96$ hours

Figure 7.2: Average a) downward, b) upward mass flux without a residence time criterion, c) downward, d) upward mass flux with a residence time $\tau \geq 24$ hours, e) downward and f) upward mass flux with a residence time $\tau \geq 96$ hours in June 2001 at T63 horizontal resolution. Units are kg s^{-1} km^{-2}.

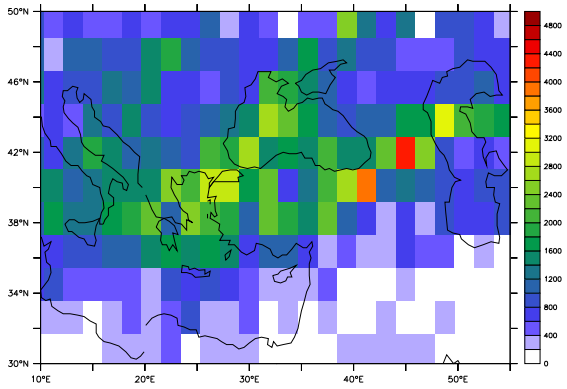

(a) downward, $\tau \geq 0$ hours

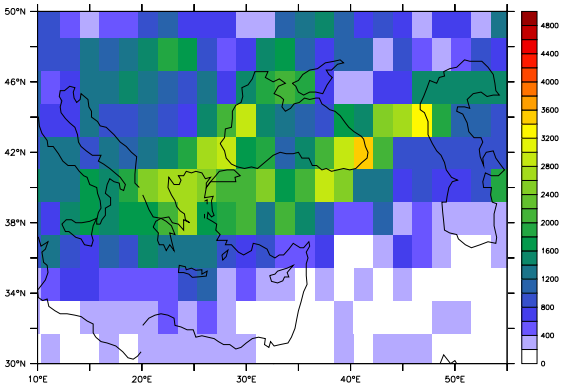

(b) upward, $\tau \geq 0$ hours

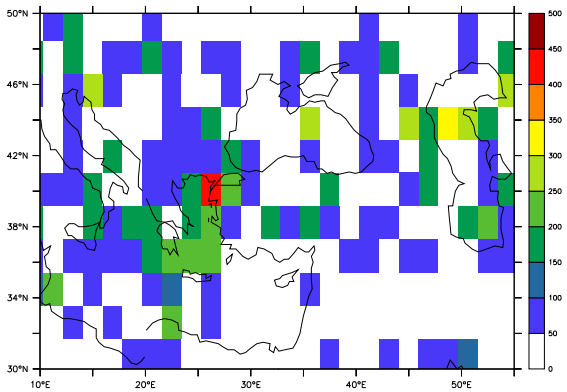

(c) downward, $\tau \geq 24$ hours

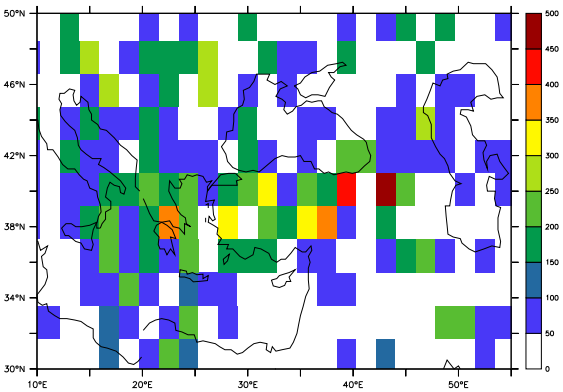

(d) upward, $\tau \geq 24$ hours

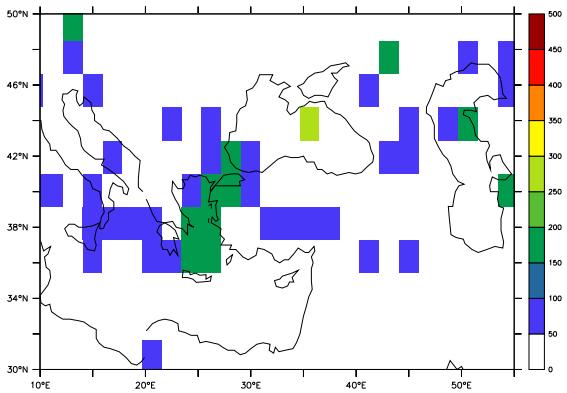

(e) downward, $\tau \geq 96$ hours

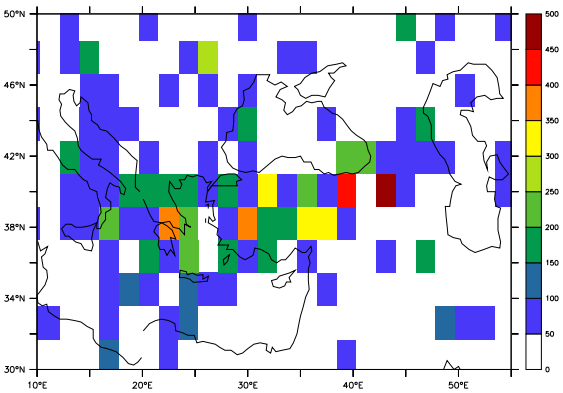

(f) upward, $\tau \geq 96$ hours

Figure 7.3: Average a) downward, b) upward mass flux without a residence time criterion, c) downward, d) upward mass flux with a residence time $\tau \geq 24$ hours, e) downward and f) upward mass flux with a residence time $\tau \geq 96$ hours in July 2001 at T63 horizontal resolution. Units are kg s^{-1} km^{-2}.

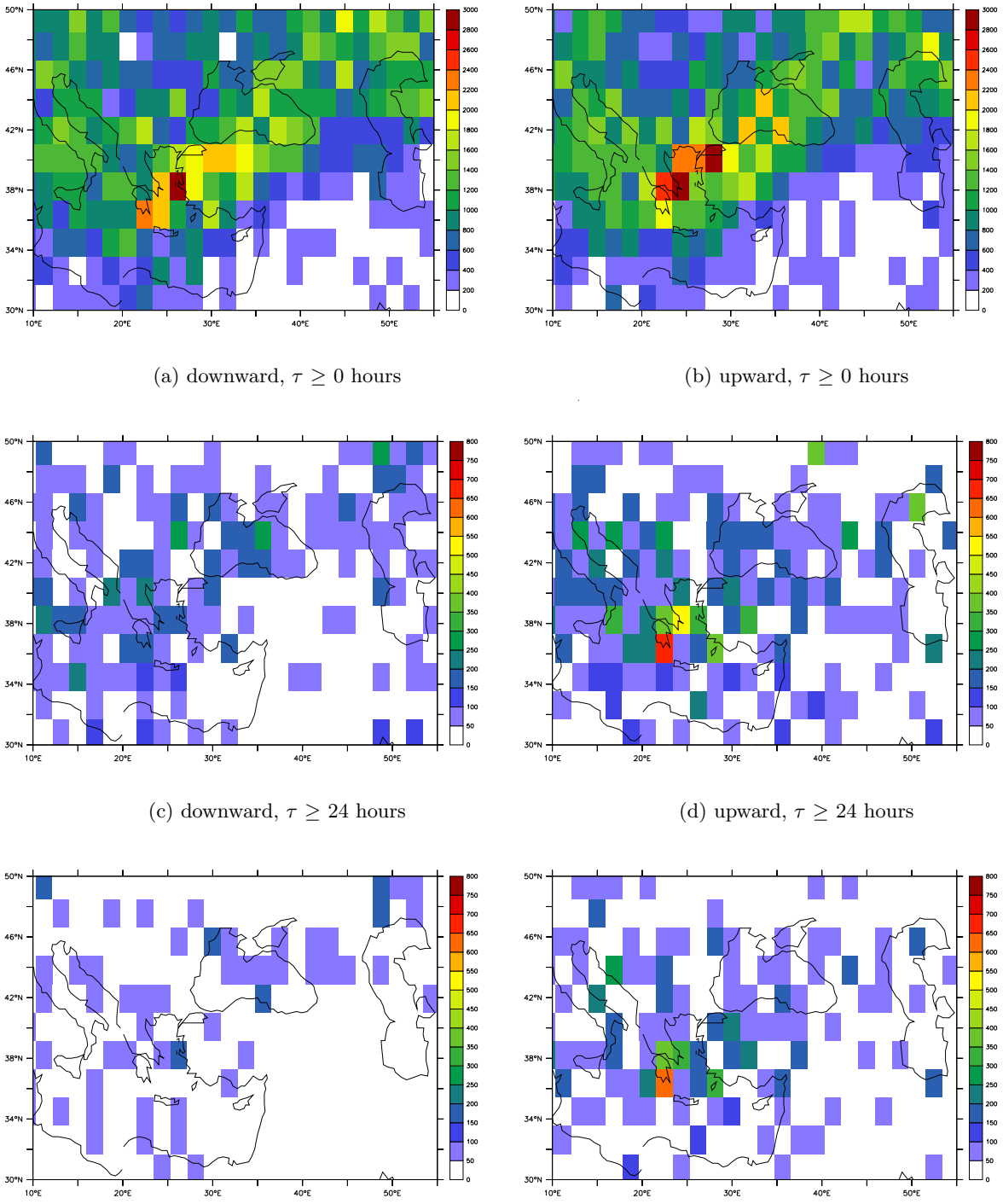

(a) downward, $\tau \geq 0$ hours

(b) upward, $\tau \geq 0$ hours

(c) downward, $\tau \geq 24$ hours

(d) upward, $\tau \geq 24$ hours

(e) downward, $\tau \geq 96$ hours

(f) upward, $\tau \geq 96$ hours

Figure 7.4: Average a) downward, b) upward mass flux without a residence time criterion, c) downward, d) upward mass flux with a residence time $\tau \geq 24$ hours, e) downward and f) upward mass flux with a residence time $\tau \geq 96$ hours in August 2001 at T63 horizontal resolution. Units are kg s^{-1} km^{-2}.

Eliminating all air parcels with a residence time less than $\tau = 24$ hours, more pronounced locations with notable cross-tropopause transport appear. Additionally, the magnitude of the mass fluxes decreases significantly, as can be seen by comparison of Figures 7.1c and 7.1d to Figures 7.4c and 7.4d. While in May maximum values are about 300 kg s^{-1} km^{-2} in the eastern Mediterranean, maximum downward fluxes of about 450 kg s^{-1} km^{-2} and upward fluxes of 550 kg s^{-1} km^{-2} in June and July and 700 kg s^{-1} km^{-2} in August are calculated.
Further increasing the residence time to $\tau \geq 96$ hours additionally reduces the extent of the areas with notable cross-tropopause transport, while the mass being transported across the 3.5 PVU iso-surface changes only slightly. In May, the area from the southeastern Mediterranean to Iraq seems to be a preferred region for "almost irreversible" events. In June, this area is stretched and shifted toward higher latitudes with enhanced upward fluxes in a band extending from the eastern Mediterranean to the Caspian Sea and enhanced downward fluxes over the eastern Mediterranean and western Turkey and additionally over eastern Turkey, Azerbaijan, southeast Georgia and northern Iran. In July and August, the situation is very comparable to June. An area with downward fluxes over the eastern Mediterranean and a band extending from southern Italy to Central Turkey with high upward mass fluxes appears, whereas in comparison to the situation in June the areas are shifted toward the northeast.

7.5 Association of cross-tropopause fluxes with upper-level circulation

The northeastward displacement of the area with enhanced mass fluxes across the 3.5 PVU iso-surface coincides with a similar displacement of the upper tropospheric flow regime. Figure 7.5 shows the mean circulation in May, June, July and August at about 200 hPa. While the upper-level anticyclone over South Asia is only weakly developed, the anticyclone over the Arabian Peninsula has not been developed at all in May. As a consequence, the area of convergence of air in the frontal zone with air transported by the upper-level anticyclonic circulation is located over the northern Arabian Peninsula, accelerating the horizontal wind and increasing horizontal and vertical wind shear as discussed in chapter 5. Figure 7.6a depicts the associated turbulence index with highest values in the area of convergence. TI index values are calculated with equation 5.1 and the wind field simulated by ECHAM5/MESSy. The displacement of the sun towards higher latitudes, along with the Asian monsoon onset in June, intensifies the upper-level Arabian and South Asian anticyclones and shifts the area of convergence towards the eastern Mediterranean area (Figure 7.5b). This large-scale synoptic flow system is maintained during July and August, whereas the area of strongest convergence and TI values slightly change due to the meandering Polar Front Jet (Figures 7.6c and 7.6d).
Comparison of the mean TI index in August calculated with the ECHAM5/MESSY wind field (Figure 7.6d) with the TI values derived from the ECMWF analyses being depicted in Figure 5.4 shows minor deviations in geographical distribution and intensity. However, considering the different horizontal resolutions of the wind fields (ECMWF: 1° x 1°, ECHAM5/MESSy: $\approx$ 1.9 ° x 1.9 °), areas with maximum TI values reaching from the eastern Mediterranean to the Caspian Sea correspond rather well.

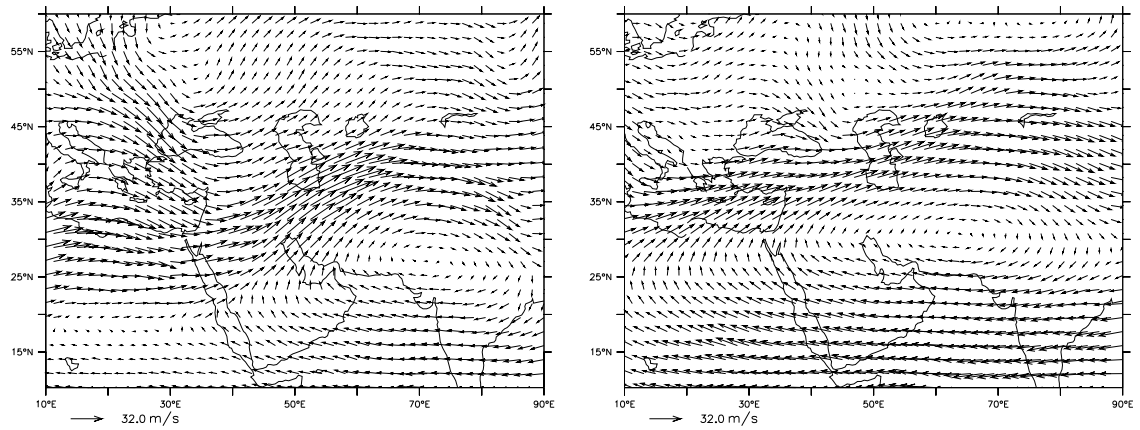

(a) May

(b) June

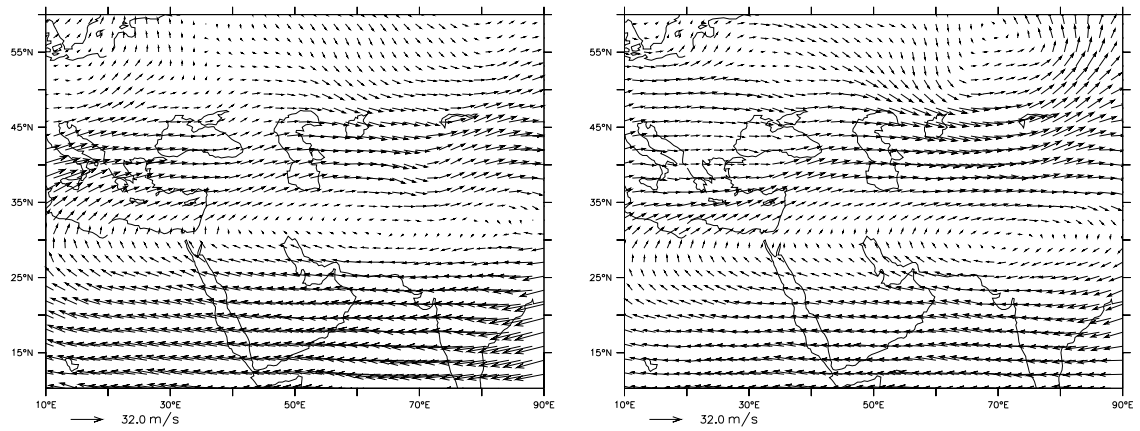

(c) July

(d) August

Figure 7.5: Mean upper-level circulation at about 200 hPa in a) second half of May, b) June, c) July and d) August

7.6 Residence time

As apparent from comparisons of the geographical distribution of areas with cross-tropopause transport, and also from the magnitude of the fluxes depicted in Figures 7.1 to 7.4, the exchange of air masses across the tropopause in the band extending from the eastern Mediterranean to the Caspian Sea is largely confined to the tropopause region. Transport that persist on time scales of more than 1 day make up only about 6% of the total downward and about 8% of the total upward fluxes, which is less than the about 25% calculated with the FLEXTRA trajectory model (see section 5.2). The differences between the two models can be explained by the availibility of the data driving the models: while an ATTILA time step was 15 minutes, the temporal resolution of the ECMWF analysis data for the FLEXTRA model was 6 hours. Increasing the residence time to $\tau \geq 96$ hours, the fluxes calculated with ATTILA decrease to about 2% of the total downward and about 6% of the total upward fluxes, in fair agreement with the 1-2% estimated

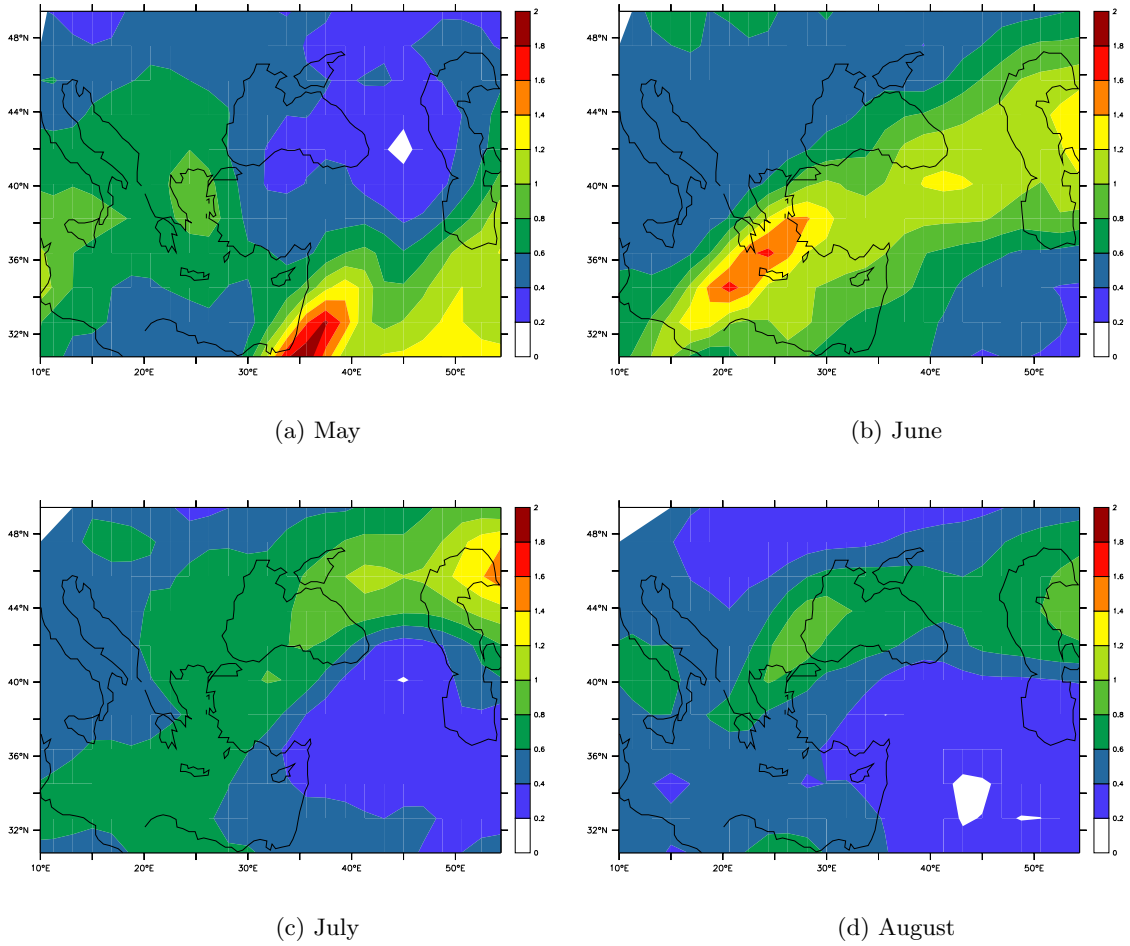

(a) May (b) June

(c) July (d) August

Figure 7.6: Mean turbulence index in 10^{-7} sec^{-2} at about 200 hPa in a) second half of May, b) June, c) July and d) August

by *James et al.* (2003) investigating a 15 year climatology of cross-tropopause transport. The minor decrease of the total upward flux as compared to the downward flux as a function of residence time, is related to the lower static stability and consequential stronger mixing from the troposphere. This causes, for example, the transport of polluted boundary layer air across the tropopause (see e.g. Asian monsoon trajectories in section 6.6.2).

The mean residence times in troposphere and stratosphere averaged over June, July and August 2001 after crossing the dynamical tropopause until returning to the sphere of origin, depending on the geographical position where the cross-tropopause transport has occurred, are depicted in Figure 7.7. It shows, that the $\sim$ 8% upward transported air across the tropopause in the band extending from the eastern Mediterranean to the Caspian Sea, resides about 5 to 15 days in the stratosphere. The residence time of the $\sim$ 6% of the total downward transported air is similar. By elimination of all air parcels with a residence time less than 5 days, the mean residence times during summer 2001 increases to 5-30 days in the stratosphere, depending on the geographical position, with an average of about 15 days. The residence time in the troposphere is slightly larger with values between 5 and 35 days with an average value of about 23 days.

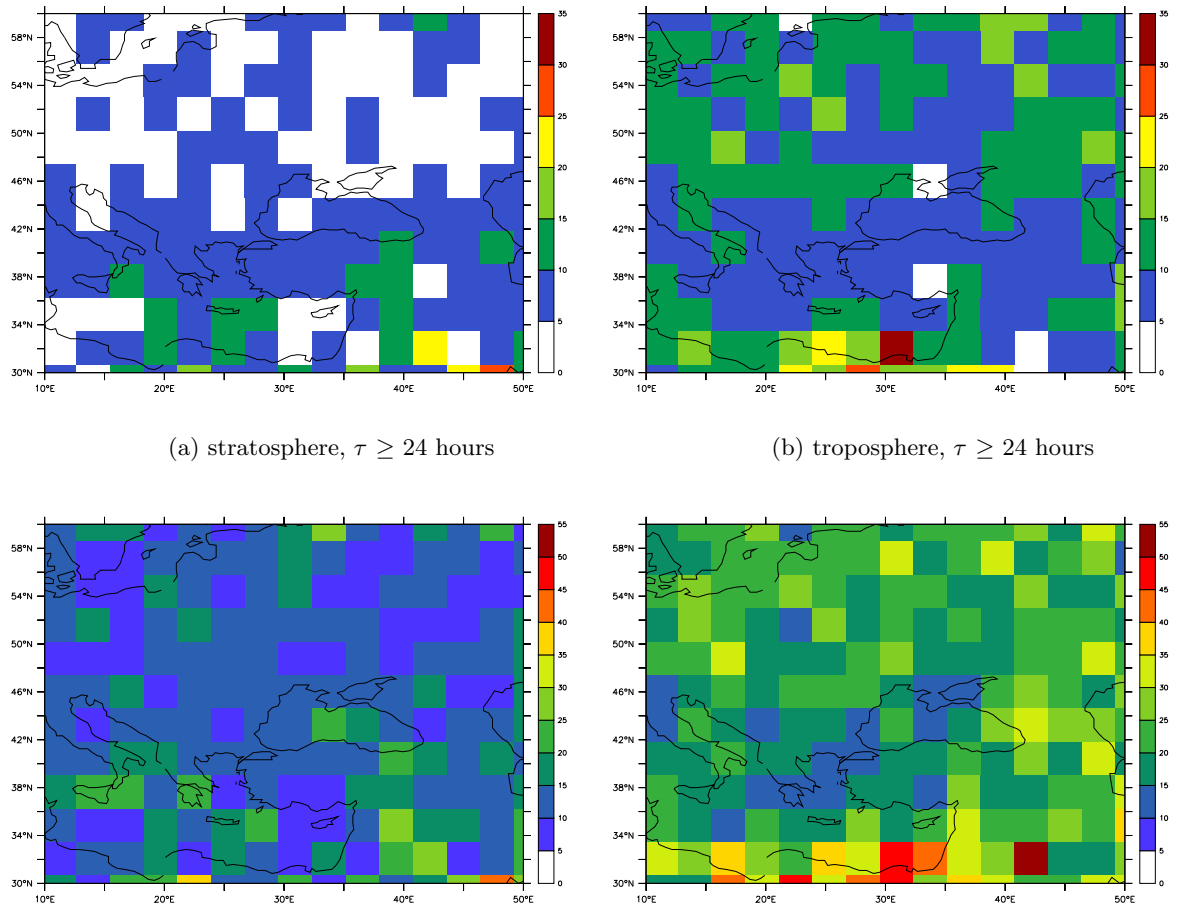

(a) stratosphere, $\tau \geq 24$ hours

(b) troposphere, $\tau \geq 24$ hours

(c) stratosphere, $\tau \geq 96$ hours

(d) troposphere, $\tau \geq 96$ hours

Figure 7.7: Mean residence time in units of days in the stratosphere (a and c) and in the troposphere (b and d) in dependence of the geographical position of the cross-tropopause transport under consideration of $\tau \geq 24$ hours and $\tau \geq 96$ hours.

7.7 Conclusions

In this chapter mass flux calculations across the 3.5 PVU iso-surface during the period from May to August 2001 over the eastern Mediterranean are presented. While in May enhanced cross-tropopause transport appears over the Arabian Peninsula, a large band from the eastern Mediterranean to the Caspian Sea with enhanced cross-tropopause transport develops in June, and is shifted toward higher latitudes in July and August. This shifting is associated with the development and the intensification of the Arabian and South Asian upper-level anticyclones and consequently with the areas of maximum clear-air turbulence, confirming the hypothesis of mixing of tropospheric and stratospheric air near the tropopause during summer over the eastern Mediterranean. Ultimately, this is a consequence of large-scale synoptic flow systems as suggested in chapter 5. Investigation of the residence time of the air in the stratosphere and in the troposphere shows that only about 7% of the air resides more than one day and about 4% more than 5 days in its destination sphere. On the other hand, average residence times of about

5 to 35 days in the troposphere and the stratosphere suggest the occurrence of deep transport events and an important potential to mix and interact. In the context of increasing emissions, especially in developing countries like India, this will likely gain importance in the near-term future.

Chapter 8

Summary and Outlook

In this thesis the large-scale transport of air over the eastern Mediterranean region during summer 2001, with a focus on August during the Mediterranean Intensive Oxidant Study (MINOS) measurement campaign, was investigated from a lagrangian perspective. The models used for the investigations are the off-line trajectory model FLEXTRA and the lagrangian transport scheme ATTILA. The latter has been developed at the Institute of Atmospheric Physics, DLR, Oberpfaffenhofen, Germany, and coupled to the chemistry-climate model ECHAM5/MESSy.

To analyze the origin of air masses chemically sampled by the DLR Falcon aircraft during MINOS, being a major objective of the campaign, back trajectories with initialization points along the flight tracks were calculated. With reference to initialization height and origin, the trajectories were categorized into different clusters. Assigning measured trace gas concentration of ozone, nitrogen oxide, total reactive oxidized nitrogen (NO_y), formaldehyde, methanol, acetonitrile, acetone, peroxyacetyl nitrate (PAN), carbon dioxide, carbon monoxide and methane to each back trajectory, the chemical composition of each cluster was calculated.

In the boundary layer significantly higher concentrations were observed in air masses originating from eastern Europe compared to air masses from western Europe. In particular, enhanced levels of acetonitrile, as well as methanol, acetone and CO indicate a strong contribution from biomass burning. In the middle atmosphere (4-8 km) air masses generally originated from the North Atlantic/North American area. Trace gas concentrations were significantly lower than in the lower 4 km of the atmosphere. At the highest levels (8-12 km) air masses from two different origins were differentiated: North Atlantic/North American and South Asia. Air masses from North Atlantic/North American included a significant contribution from the stratosphere, resulting in higher values of O_3 and NO_y, while South Asian air masses were characterized by lower O_3 and NO_y values, and enhanced CO, CH_4 and HCHO levels. The analysis of trajectories, being initialized in the Asian boundary layer and transported from the surface by strong convection in the Indian monsoon, indicated Asian emissions in the upper troposphere over the eastern Mediterranean.

Investigation of the potential vorticity along trajectories in August 2001 indicated enhanced cross-tropopause transport in the upper eastern Mediterranean region relative to the surrounding regions. Being associated with the convergence of air transported by the upper-level anticyclone over the Arabian and Asian heat lows as well as the Polar Front Jet toward the eastern Mediterranean, a jet streak with an entrance over the region within the Subtropical Jet Stream is formed. At the cyclonic side of this jet streak the tropopause descents to lower height levels, depending on the wind speed within the jet. As a result of horizontal and vertical wind

shear along that jet streak, clear-air turbulence causes mixing of tropospheric and stratospheric air near the tropopause, mainly at the cyclonic side of the jet axis. Analyses of the potential temperature along the trajectory paths and also of the residence times in stratosphere or troposphere after crossing the tropopause, indicate that mixing of air masses is largely confined to the tropopause region, whereas deep transport of tropospheric air into the stratosphere or vice versa does not seem to occur at this locations. Ultimately, this results from the interplay of large-scale synoptic flow systems, the Polar Front Jet and the Arabian and Asian heat lows, the latter two being quasi-permanent only during summer. Turbulent mixing of air near the tropopause was suggested to play an important role in cross-tropopause transport during summer.

Lagrangian calculations of mass fluxes across the tropopause with ATTILA and ECHAM5/MESSy for the period of May to August 2001 confirm the hypothesized contribution of turbulent mixing of tropospheric and stratospheric air during summer over the eastern Mediterranean as a result of large-scale synoptic disturbances. While in May enhanced cross-tropopause transport appears over the southeastern Mediterranean to the southwestern part of the Caspian Sea, this large band is shifted toward higher latitudes in June, July and August. This shifting is associated with the development and the intensification of the Arabian and South Asian upper-level anticyclones and also with the areas of strongest clear-air turbulence. Investigation of the residence time shows that merely about 7% of the air resides more than one day and about 4% more than 5 days in its destination sphere. Average residence times of air crossing the tropopause over the eastern Mediterranean of about 5 to 30 days in the troposphere and the stratosphere suggest the occurrence of deep transport events, and the important potential of tropospheric and stratospheric air to mix and interact chemically.

This doctoral thesis describes the transport of polluted air masses from many source regions in the northern hemisphere in summer to the eastern Mediterranean, where a large quasi-permanent area with enhanced cross-tropopause transport is located in association with the South Asian monsoon. Even though the total mass of air crossing the tropopause in this area is only a few percent, further investigations of the influence of increasing emissions, with special attention for developing countries in Asia, and the possible consequences for the Mediterranean and global climate, are needed.

Presently, ATTILA is applied as a forward trajectory model driven by the three-dimensional wind field, being calculated each time step by the chemistry-climate model ECHAM5/MESSy. In the near-term future, the coupling of chemical tracers and aerosols with ATTILA is planned, providing a powerful tool for the analysis of measurement campaigns and even for atmospheric chemical forecasts.

Appendix A

Fourth order Runge-Kutta method

[3] To calculate the position $\vec{r}$(t+Δt) of an air parcel at time step t+Δt in ATTILA, the fourth order Runge-Kutta method is used, which is generally described in *Press et al.* (1990).
In the present case, it involves to calculate flow fields, whereas $\vec{r_1}$=$\vec{r}$(t) is the current position of an air parcel, $\vec{u}$($\vec{r}$,t) is the by ECHAM5/MESSy calculated wind field and δt = 0 in ATTILA.

$$
\begin{aligned}
\vec{u_1} &= \vec{u}(\vec{r_1}, t) \\
\vec{u_2} &= \vec{u}(\vec{r_2}, t + \delta t/2) \\
\vec{u_3} &= \vec{u}(\vec{r_3}, t + \delta t/2) \\
\vec{u_4} &= \vec{u}(\vec{r_4}, t + \delta t) \\
with & \\
\vec{r_2} &= \vec{r_1} + \vec{u_1} \cdot \Delta t/2 \\
\vec{r_3} &= \vec{r_1} + \vec{u_2} \cdot \Delta t/2 \\
\vec{r_4} &= \vec{r_1} + \vec{u_3} \cdot \Delta t \\
u^{\vec{RK4}} &= \frac{1}{6} \cdot (\vec{u_1} + 2 \cdot (\vec{u_2} + \vec{u_3}) + \vec{u_4})
\end{aligned}
$$

The new position can therefore be calculated with

$$\vec{r}(t + \Delta t) = \vec{r}(t) + u^{\vec{RK4}} \cdot \Delta t$$

In Figure A.1 this calculation is depicted for a 1-dimensional problem.
The Runge-Kutta method is a fourth-order method. The formula for the *real* position $\vec{r_T}$(t+Δt) with δt=Δt and the wind field $\vec{u}$, being a continuous flow field, looks as follows:

$$r\vec{_T}(t + \Delta t) = \vec{r}(t) + u^{\vec{RK4}} \cdot \Delta t + O(\Delta t^5),$$

For a non-continuous wind field on a discrete grid this formula is invalid, because the wind field has to be interpolated for the calculation of $\vec{u_1}$, ..., $\vec{u_4}$.
In ATTILA no temporal interpolation (δt = 0) is done , because the time steps of ECHAM5/MESSy

[3] adopted from *Reithmeier* (2001)

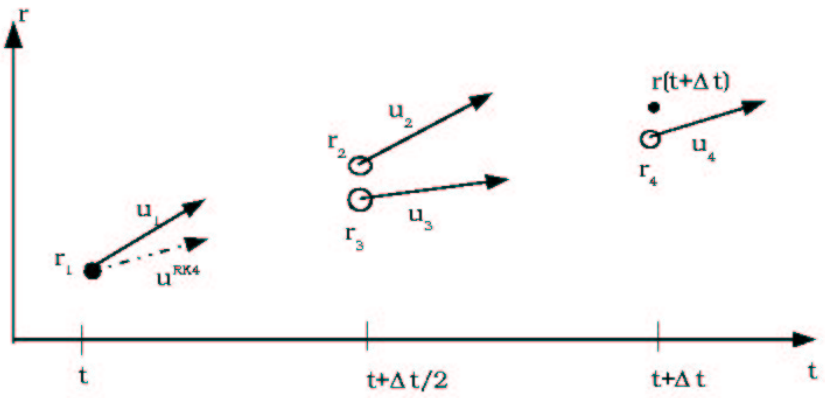

Figure A.1: Fourth order Runge-Kutta method

are very short, while horizontal interpolation is linear and vertical cubic hermite.

Appendix B

Cubic hermite interpolation

[4] The vertical interpolation of the wind field in ATTILA is cubic hermite. A detailed introduction into the theoretical basics is given by *Mennicken and Wagenführer* (1977), for instance.
The problem is as follows: find for two values $x_1 < x_2$ and a function f(x) a third order polynomial P(X), so that

$$P(x_i) = f(x_i) \quad and \quad P'(x_i) = f'(x_i) \quad with \quad i = 1, 2$$

A polynomial P(X) complying with the criterion above is

$$\begin{aligned} P(X) &= \sum_{i=1}^{4} a_i \alpha^{4-i} \\ with & \\ \alpha &= \frac{x_2 - x_1}{X - x_1} \\ a_4 &= f(x_1) \\ a_3 &= f'(x_1) \cdot (x_2 - x_1) \\ a_2 &= -f'(x_2) \cdot (x_2 - x_1) + 3 \cdot f(x_2) - 2 \cdot a_3 - 3 \cdot a_4 \\ a_1 &= f(x_2) - a_2 - a_3 - a_4 \end{aligned}$$

In ATTILA, x corresponds to the vertical coordinate η and f to the vertical profile of a component of the wind field $\vec{u}$. In contrast to the problem above, the vertical wind is not continouos, but known at discrete model levels η_i. For that case, the gradient of $\vec{u}$ is estimated with finite differences at the center of the model levels.
To calculate the vertical position η_0 of an air parcels with a known vertical wind field $\vec{u}(\eta_i)$ following algorithm is used in ATTILA:

- Appointment of the 4 adjacent model levels η_1, ..., η_4 with

  $$\eta_1 \leq \eta_2 \leq \eta_0 \leq \eta_3 \leq \eta_4$$

  If the air parcels is in the lowest or highest model level, $\eta_1 = \eta_2$ and $\eta_3 = \eta_4$ is set.

[4] adopted from *Reithmeier* (2001)

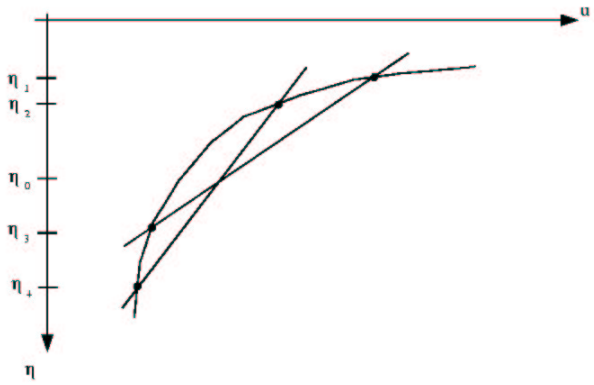

Figure B.1: Cubic hertime interpolation

- Estimation of the gradients Δ_i at η_i (i = 2, 3) with

$$\Delta_2 = \frac{\eta_3 - \eta_1}{u_3 - u_1} \qquad and \qquad \Delta_3 = \frac{\eta_4 - \eta_2}{u_4 - u_2}$$

  with u_i=u(η_i),i=1,....,4 (see Figure B.1).

- Calculation of the coefficients of the polynomial P:

$$\begin{aligned} a_4 &= u_2 \\ a_3 &= \Delta_2 \cdot (\eta_3 - \eta_2) \\ a_2 &= -\Delta_3 \cdot (\eta_3 - \eta_2) + 3 \cdot u_3 - 2 \cdot a_3 - 3 \cdot a_4 \\ a_4 &= u_3 - a_2 - a_3 - a_4 \end{aligned}$$

- Calculation of the polynomial

$$\begin{aligned} P(X) &= \sum_{i=1}^{4} a_i \alpha^{4-i} \\ with & \\ \alpha &= \frac{\eta - \eta_1}{\eta_3 - \eta_2} \end{aligned}$$

  at position η_0.
  Finally, the interpolated wind $u_{interpolated}$ at η_0 is

$$u_{interpolated} = P(\eta_0)$$

List of Acronyms and Abbreviations

AHDT	absolute horizontal transport deviation
AVDT	absolute vertical transport deviation
ATTILA	Atmospheric Tracer Transport in a Lagrangian Model
CAT	clear-air turbulence
CO	carbon monoxide
CO_2	carbon dioxide
CH_3CN	acetonitrile
CH_3COCH_3	acetone
CH_3OH	methanol
CH_4	methane
DKRZ	Deutsches Klimarechenzentrum (Hamburg), German Climate Computing Centre
DLR	Deutsche Luft- und Raumfahrt
ECHAM4	European community Hamburg climate model version 4
ECHAM5	European community Hamburg climate model version 5
ECMWF	European Centre for Medium-Range Weather Forecasts
GCM	General Circulation Model
HCHO	formaldehyde
ITCZ	Intertropical Convergence Zone
MESSy	Modular Earth Submodel System
MINOS	Mediterranean Intensive Oxidant Study
NAO	North Atlantic Oscillation
NAONA	North Atlantic Ocean /North America
NO	nitrogen oxide
NO_y	reactive nitrogen
O_3	ozone
PAN	peroxyacetyl nitrate
PFJ	Polar Front Jet
PV	Potential Vorticity
PVU	Potential Vorticity Units
RLD	relative length difference
RSD	relative spherical distance
STJ	Subtropical Jet
TEJ	Tropical Easterly Jet
TI	Turbulence Index
WMO	World Meteorological Organization

List of Tables

List of Figures

Bibliography

Appenzeller, C., J. R. Holton, and K. H. Rosenlof, Seasonal variation of mass transport across the tropopause, *J. Geophys. Res.*, *101*, 15071–15078, 1996b.

Baede, A. P. M., Climate Change 2001: The Scientific Basis : Contribution of Working Group I to the Third Assessment Report of the Intergovernmental Panel on Climate Change, edited by J. T. Houghton *et al.*, 2001, Cambrige University Press, 2001.

Bamber, D., P. Healey, B. Jones, S. Penkett, A. Tuck, and G. Vaughan, Vertical profiles of tropospheric gases: chemical consequences of stratospheric intrusions, *Atmos. Environ.*, *18*, 1759–1766, 1984.

Baray, J.-L., V. Daniel, G. Ancellet, and B. Legras, Planetary-scale tropopause folds in the southern subtropics, *Geophys. Res. Lett.*, *27*, 353–356, 2000.

Belman, S., The fluorimetric determination of formaldehyde, *Analytica Chimica Acta*, *29*, 120–126, 1963.

Bertin, F., B. Campistron, J. L. Caccia, and R. Wilson, Mixing processes in a tropopause folding observed by a network of st radar and lidar, *Annales Geophysicae*, *19*, 1–11, 2001.

Board, A.S., H.E. Fuelberg, G.L. Gregory, B.G. Heikes, M.G. Schultz, D.R. Blake, J.E. Dibb, S.T. Sandholm, and R.W. Talbot, Chemical characteristics of air from different source regions during the Pacific Exploratory Mission-Tropics A (PEM-Tropics A), *J. Geophys. Res.*, *104*(D13), 16181–16196, 1999.

Bolle, H-J, Mediterranean climate, 2003, Springer, 2003.

Byers, H. R., *General Meteorology*, McGraw-Hill, New York, U.S.A, 1974.

Chen, P., Isentropic cross-tropopause mass exchange in the extratropics, *J. Geophys. Res.*, *100*, 16661–16673, 1995.

Chiapello, I., G. Bergametti, B. Chatenet, P. Bousquet, F. Dulac, and E. Santos Soares, Origins of African dust transported over the northeast tropical Atlantic, *J. Geophys. Res.*, *102*, 13701–13709, 1997.

Cubasch, U., K. Hasselmann, H. Hock, E. Maierreimer, U. Mikoljewicz, B. D. Santer, and R. Sausen, Time-dependent greenhouse warming computations with a coupled ocean-atmosphere model, *Climate Dyn.*, *8*, 55–69, 1992.

D'Abreton, P. C., and P. D. Tyson, Three-dimensional kinematic trajectory modeling of water vapour transport over Southern Africa, *Water SA*, *22*, 297–306, 1996.

Danielsen, E. F., Stratospheric-tropospheric exchange based on radioactivity, ozone and potential vorticity, *J. Atmos. Sci.* , pp. 25502–25518, 1968.

Doty, K.G., and D.J Perkey, Sensitivity of trajectory calculations to the temporal frequency of wind data, *Mon. Wea. Rev.* , *121*, 387–401, 1993.

Dutton, J. A., *The Ceaseless Wind. An Introduction to the Theory of Atmospheric Motion*, Dover, New York, 1986.

Ellrod, G., and D. Knapp, An Objective Clear-Air Turbulence Forecasting Technique: Verification and Operational Use, *Weather and Forecasting*, *7*(1), 1992.

Feichter, J., U. Lohmann, and I. Schult, The atmospheric sulfur cycle in ECHAM-4 and its impact on the shortwave radiation, *Climate Dyn.*, *13*(4), 235–246, 1997.

Fischer, H., F. Wienhold, P. Hoor, O. Bujok, C. Schiller, P. Siegmund, M. Ambaum, H. Scheeren, and J. Lelieveld, Tracer correlations in the northern high latitude lowermost stratosphere: Influence of cross-tropopause mass exchange, *Geophys. Res. Lett.*, *27*, 92–100, 2000.

Folkins, I., M. Loewenstein, J. Podolske, S. J. Oltmans, and M. Profitt, A barrier to vertical mixing at 14 km in the tropics: Evidence from ozonesondes and aircraft measurements, *J. Geophys. Res.*, *104*(D18), 22095–22102, 1999.

Gettelman, A., and A. H. Sobel, Direct diagnoses of stratosphere-troposphere exchange, *J. Atmos. Sci.* , *57*, 3–16, 2000.

Hintsa, E.J., and et al., Troposphere-to-Stratosphere Transport in the Lowermost Stratosphere From Measurements of H2O, CO2, N2O and O3, *Geophys. Res. Lett.*, *25*, 2655–2658, 1998.

Hoell, J. M., D. D. Davis, S. C. Liu, R. E. Newell, H. Akimoto, R. J. Mcneal, and R. J. Bendura, The Pacific Exploratory Mission West phase B: february-march, 1994, *J. Geophys. Res.*, pp. 28223–28239, 1997.

Hoerling, M., T. Schaak, and A. Lenzen, Global objective tropopause analysis, *Mon. Wea. Rev.*, *119*, 1816–1839, 1991.

Holton, J., P. Haynes, M. McIntyre, A. Douglass, R. Rood, and L. Pfister, Stratosphere-Troposphere Exchange, *Rev. Geophys.*, *33*, 403–439, 1995.

Holzinger, R., C. Warneke, A. Jordanm, A. Hansel, W. Lindinger, D.H. Scharffe, G. Schade, and P.J. Crutzen, Biomass burning as a source of Formaldehyde, Acetaldehyde, Methanol, Acetone, Acetonitrile, and Hydrogen Cyanide, *Geophys. Res. Lett.*, *26*(8), 1161, 1999.

James, P., A. Stohl, C. Forster, S. Eckhardt, P. Seibert, and A. Frank, A 15-year climatology of stratosphere-troposphere exchange with a Lagrangian particle dispersion model: 2. Mean climate and seasonal variability, *J. Geophys. Res.*, *108*(D12), doi:10.1029/2002JD002639, 2003.

Jöckel, P., and R. Sander, Technical Note: The Modular Earth Submodel System MESSy - a new approach towards Earth System Modeling, *Atmos. Chem. Phys. Discuss.*, 2004, submitted.

Jeuken, A. B. M., P. C. Siegmund, L. C. Heijboer, J. Feichter, and L. Bengtson, On the potential of assimilating meteorological analysis in a climate model for the purpose of model validation, *J. Geophys. Res.*, *101*, 16939–16950, 1996.

Kjellström, E., J. Feichter, R. Sausen, and R. Hein, The contribution of aircraft emissions to the atmospheric sulfur budget, *Atmos. Environ.*, *33*(21), 3455–3465, 1999a.

Kjellström, E., J. Feichter, and G. Hoffman, Transport of SF6 and (CO2)-C-14 in the atmospheric general circulation model ECHAM4, *Tellus*, *52*(Series B), 1–18, 1999b.

Kormann, R., H. Fischer, M. de Reus, M. Lawrence, Ch. Brühl, R. von Kuhlmann, R. Holzinger, J. Williams, J. Lelieveld, C. Warneke, J. de Gouw, J. Heland, H. Ziereis, and H. Schlager, Formaldehyde over the eastern Mediterranean during MINOS: Comparison of airborne in-situ measurements with 3D-model results, *Atmos. Chem. Phys.*, *3*, 1303–1331, 2003.

Kouvarakis, K., K. Tsigaridis, M. Kanakidou, and N. Mihalopoulos, Temporal variations of surface regional background ozone over Crete Island in the southeast Mediterranean, *J. Geophys. Res.*, *105*(D4), 4399–4407, 2000.

Kowol-Santen, J., and G. Ancellet, Mesoscale analysis of transport across the subtropical tropopause, *J. Geophys. Res.*, 2000.

Kowol-Santen, J., H. Elbern, and A. Ebel, Estimation of cross-tropopause airmass fluxes at midlatitudes: Comparison of different numerical methods and meteorological situations, *Mon. Wea. Rev.* , *128*, 4045–4057, 2000.

Kuo, Y.H., M. Skumanich, P.L. Haagenson, and J.S. Chang, The accuracy of trajectory models as revealed by the observing system simulation experiments, *Mon. Wea. Rev.* , *113*(11), 1852–1867, 1985.

Lamarque, J.-F., and P. G. Hess, Cross-tropopause mass exchange and potential vorticity budget in a simulated tropopause folding, *J. Atmos. Sci.* , *51*, 2246–2269, 1994.

Langford, A. O., C. D. Masters, M. H. Proffitt, E.-Y. Hsie, and A. F. Tuck, Ozone measurements in a tropopause fold associated with a cut-off low system, *Geophys. Res. Lett.*, *23*(18), 2501–2504, 1996.

Lawrence, M. G., P. J. Rasch, R. von Kuhlmann, J. Williams, H. Fischer, M. de Reus, J. Lelieveld, P. J. Crutzen, H. Huntrieser, J. Heland, A. Stohl, C. Forster, M. Schultz, P. Stier, and R. Dickerson, Chemical weather forecasting as a tool for field campaign planning: Predictions and observations of large-scale features during INDOEX, MINOS, and CONTRACE, *Atmos. Chem. Phys.*, *3*, 267–289, 2003.

Lelieveld, J., B. Bregman, F. Arnold, V. Buerger, P. J. Crutzen, H. Fischer, A. Waibel, P. Siegmund, and P. F. J. van Velthoven, Chemical perturbation of the lowermost stratosphere through exchange with the troposphere, *J. Geophys. Res.*, *24*(5), 603–606, 1997.

Lelieveld, J., H. Berresheim, S. Borrmann, P.J. Crutzen, F. Dentener, H. Fischer, J. Feichter, P.J. Flatau, J. Heland, R. Holzinger, R. Korrmann, M.G. Lawrence, Z. Levin, K. Markowicz, N. Mihalopoulos, A. Minikin, V. Ramanathan, M. de Reus, G.J. Roelofs, H.A. Scheeren,

J. Sciare, H. Schlager, M. Schultz, P. Siegmund, B. Steil, E.G. Stephanou, P. Stier, M. Traub, C. Warneke, J. Williams, and H. Ziereis, Global air pollution crossroads over the Mediterranean, *Science*, *298*, 794–799, 2002.

Lindinger, W., A. Hansel, and A. Jordan, On-line monitoring of volatile organic compounds at pptv levels by means of Proton-Transfer-Reaction Mass Spectrometry (PTR-MS) Medical applications, food control and environmental research, *Int. J. Mass Spectrom.*, *173*, 1998.

Lohmann, U., and J. Feichter, Impact of sulfate aerosols on albedo and lifetime of clouds: A sensitivity study with the ECHAM4 GCM, *J. Geophys. Res.*, *102*(D12), 13685–13700, 1997.

Meloen, J., *Simulation and Diagnosis of Stratosphere-Troposphere Exchange*, Ph.D. dissertation, Technische Universiteit Eindhoven, 2002.

Mennicken, R., and E. Wagenführer, *Numerische Mathematik 2*, rororo vieweg, Rowohlt Taschenbuch Verlag GmbH, Reinbek bei Hamburg, 1977.

Merril, J.T., R. Bleck, and L. Avila, Modeling atmospheric tracer transport to the Marshall islands, *J. Geophys. Res.*, *90*(12927–12936), 1985.

Moody, J.L., S.J. Oltmans, H. Levy II, and J.T. Mertill, Transport climatology of tropospheric ozone: Bermuda, 1988-1991, *J. Geophys. Res.*, *100*(D4), 7179–7191, 1995.

Overeem, A., Verification of clear-air turbulence forecasts, *report, Koninklijk Nederlands Meteorologisch Instituut, De Bilt*, 2002.

Parrish, D. D., J. S. Holloway, M. Trainer, P. C. Murphy, G. L. Forbes, and F. C. Fehsenfeld, Export of North American ozone pollution to the North Atlantic Ocean, *Science*, *259*, 1436–1439, 1993.

Petterssen, S., Weather Analysis and Forecasting, pp. 221–223, 1940, McGraw-Hill, New York, 1940.

Pflügler, U., M. Roos, and I. Jacobsen, Trajektorienberechnung auf Basis des neuen Wettervorhersagesystems des Deutschen Wetterdienstes und ihre Anwendung für die Ausbreitungsrechnung, *Deutscher Wetterdienst*, 1990.

Pochanart, P., H. Akimoto, S. Maksyutov, and J. Staehelin, Surface ozone at the Swiss Alpine site Arosa: the hemispheric background and the influence of large-scale anthropogenic emissions, *Atmos. Environ.*, *35*, 5553–5566, 2001.

Ponater, M., W. König, R. Sausen, and F. Sielmann, Circulation regime fluctuations and their effect on intraseasonal variability in the ECHAM climate model, *Tellus*, *46*(Series A), 265–285, 1994.

Press, W.H., B.P. Flannery, S.A. Teukolsky, and W.T. Vetterling, *Numerical Recipes - The Art of Scientific Computing (FORTRAN Version)*, Cambridge University Press, Cambridge, 1990.

Price, J. D., and G. Vaughan, On the potential for stratosphere-troposphere exchange in cut-off low systems, *Quart. J. Roy. Met. Soc.*, *119*, 343–365, 1993.

Ramaswamy, V., M. Schwarzkopf, and K. Shine, Radiative forcing of climate from halocarbon-induced global stratospheric ozone loss, *Nature*, *355*, 810–812, 1992.

Ray, E. A., F. L. Moore, J. W. Elkins, G. S. Dutton, D. W. Fahey, H. Vömel, S. J. Oltmans, and K. H Rosenlof, Transport into the Northern Hemisphere lowermost stratosphere revealed by in situ tracer measurements, *J. Geophys. Res.*, *104*(D21), 26565–26580, 1999.

Reed, R., A study of a characteristic type of upper level frontogenesis, *J. Meteor.*, *12*, 226–237, 1955.

Reithmeier, C, *Untersuchungen zum globalen Spurenstofftransport und Stratosphaeren-Troposphaeren-Austausch mit dem Lagrangeschen Modell ECHAM4/ATTILA*, Ph.D. dissertation, Ludwig-Maximilians-Universität München, 2001.

Reithmeier, C., and R. Sausen, ATTILA - Atmospheric Tracer Transport in a Lagrangian Model, *Report no.141*, Institute of Atmospheric Physics - DLR, Oberpfaffenhofen, 2000.

Roeckner, E., K. Arpe, L. Bengtsson, M. Christoph, M. Claussen, L. Dümenil, M. Esch, M. Giorgetta, U. Schlese, and U. Schulzweida, The atmospheric general circulation model ECHAM-4: Model description and simulation of present-day climate, *Report No. 218 ISSN 0937–1060*, Max Planck Institute for Meteorology, Hamburg, 1996.

Roeckner, E., J. M. Oberhuber, A. Bacher, M. Christoph, and I. Kirchner, ENSO variability and atmospheric response in a global coupled atmosphere ocean GCM, *Climate Dyn.*, *12*, 737–754, 1996b.

Roeckner, E., L. Bengtsson, J. Feichter, J. Lelieveld, and H. Rodhe, Transient climate change simulations with a coupled atmosphere-ocean GCM including the tropospheric sulfur cycle, *J. Climate*, *12*(10), 3004–3032, 1999.

Roeckner, E., G. Bäuml, L. Bonaventura, R. Brokopf, M. Esch M. andGiorgetta, S. Hagemann, I. Kirchner, L. Kornblueh, E. Manzini, A. Rhodin, U. Schlese, U. Schulzweida, and A. Tompkins, The atmospheric general circulation model ECHAM5 part 1, model description, *Report No.349*, Max Planck Institute for Meteorology, Hamburg, Germany, 2003.

Roelofs, G. J., and J. Lelieveld, Distribution and budget of O3 in the troposphere calculated with a chemistry-climate model, *J. Geophys. Res.*, *100*(D10), 20983–20998, 1995.

Roelofs, G. J., and J. Lelieveld, Tropospheric ozone simulation with a chemistry-general circulation model: Influence of higher hydrocarbon chemistry, *J. Geophys. Res.*, *105*(D18), 22697–22712, 2000.

Roelofs, G.-J., H. A. Scheeren, T. Kentarchos, and J. Lelieveld, Distribution and origin of ozone in the eastern Mediterranean free troposphere, *Atmos. Chem. Phys.*, *3*, 1199–1210, 2003.

Rolph, G.D., and R.R. Draxler, Sensitivity of 3-dimensional trajectories to the spatial and temporal densities of the wind-field, *J. Applied Met.*, *29*, 1043–1054, 1990.

Sausen, R., B. Feneberg, and M. Ponater, Climatic impact of aircraft induced ozone changes, *Geophys. Res. Lett.*, *24*, 1203–1206, 1997.

Scheele, M. P., P. C. Siegmund, and P. F. J. van Velthoven, Sensitivity of trajectories to data resolution and its dependence on the starting point: in or outside a tropopause fold, *Meteorol. Appl.*, *3*, 267–273, 1996.

Scheeren, B., J. Lelieveld, J. Williams, G.-J. Roelofs, H. Fischer, M. de Reus, J. de Gouw, C. Warneke, R. Holzinger, H. Schlager, T. Klüpfel, M. Boldel, C. van der Veen, and M. Lawrence, The impact of monsoon outflow from South-East Asia in the upper troposphere over the eastern Mediterranean, *Atmos. Chem. Phys.*, *3*, 1589–1608, 2003.

Schlager, H., P. Konopka, P. Schulte, U. Schumann, H. Ziereis, F. Arnold, M. Klemm, D. Hagen, P. Whitefield, and J. Ovarlez, In situ observations of air traffic emission signatures in the North Atlantic flight corridor, *J. Geophys. Res.*, *102*, 10779–10750, 1997.

Seibert, P., Convergence and accuracy of numerical methods for trajectory calculations, *J. Applied Met.*, *32*, 558–566, 1993.

Shapiro, M., The roll of turbulent heat flux in the generation of potential vorticity in the vicinity of upper level jet stream systems, *Mon. Wea. Rev.* , *102*, 892–906, 1976.

Shapiro, M., Further evidence of the mesoscale and turbulent structure of upper level jet stream-frontal zone systems, *Mon. Wea. Rev.* , *106*, 1001–1011, 1978.

Sprenger, M., and H. Wernli, A northern hemispheric climatology of cross-tropopause exchange for the ERA15 time period (1979-1993), *J. Geophys. Res.*, *108*(D12), doi:10.1029/2002JD002636, 2003.

Steinacker, R., Airmass and frontal movement around the Alps, *Rivista di Meteorologia Aeronautica*, *44*, 85–93, 1984.

Stohl, A., Trajectory statistics - a new method to establish source-receptor relationships of air pollutants and its application to the transport of particulate sulfate in Europe, *Atmos. Environ.*, *30*, 579–587, 1996.

Stohl, A., Computation, Accuracy and Applications of Trajectories - A Review and Bibliography, *Atmos. Environ.*, *32*(6), 947–996, 1998a.

Stohl, A., A 1-year Lagrangian climatology of airstreams in the Northern Hemisphere troposphere and lowermost stratosphere, *J. Geophys. Res.*, *106*, 7263–7279, 2001.

Stohl, A., and P. Seibert, Accuracy of trajectories as determined from the conservation of meteorological tracers, *Quart. J. Roy. Met. Soc.*, *125*, 1465–1485, 1998.

Stohl, A., and P. Seibert, Accuracy of trajectories as determined from the conservation of meteorological tracers, *Quart. J. Roy. Met. Soc.*, *124*, 1465–1484, 1998b.

Stohl, A., and T. Trickl, A textbook example of longrange transport: Simultaneous observation of ozone maxima of stratospheric and North American origin in the free troposphere over Europe, *J. Geophys. Res.*, *104*, 30445–30462, 1999.

Stohl, A., G. Wotawa, P. Seibert, and H. Kromp-Kolb, Interpolation errors in wind fields as a function of spatial and temporal resolution and their impact on different types of kinematic trajectories, *J. Ap. Me.*, *34*, 2149–2165, 1995.

Stohl, A., L. Haimberger, M. P. Scheele, and H. Wernli, An intercomparison of results from three trajectory models, *Meteorol. Appl.*, *8*, 127–135, 2001.

Stohl, A., S. Eckhardt, C. Forster, P. James, and N. Spichtinger, On the pathways and timescales of intercontinental air pollution transport, *J. Geophys. Res.*, *107*(D23), doi:10.1029/2001JD001396, 2002.

Stohl, A., P. Bonasoni, P. Cristofanelli, W. Collins, J. Feichter, A. Frank, C. Forster, E. Gerasopoulos, H. Gäggeler, P. James, T. Kentarchos, H. Kromp-Kolb, B. Krüger, C. Land, J. Meloen, A. Papayannis, A. Priller, P. Seibert, M. Sprenger, G. J. Roelofs, H. E. Scheel, C. Schnabel, P. Siegmund, L. Tobler, T. Trickl, H. Wernil, V. Wirth, P. Zanis, and C. Zerefos, Stratosphere-troposphere exchange: A review, and what we have learned from STACCATO, *J. Geophys. Res.*, *108*(D12), doi:10.1029/2002JD002490, 2003.

Timmreck, C., H. Graf, and J. Feichter, Simulation of Mt. Pinatubo volcanic aerosol with the Hamburg climate model ECHAM4, *Theor. Appl. Climatol.*, *62*(3–4), 85–108, 1999.

Toumi, O., R. Turco, J. Jordan, J. Goodman, and G. Ferry, Physical Processes in Polar Stratospheric Ice Clouds, *Nature*, *372*, 348–351, 1994.

Vaughan, G., *Stratosphere-troposphere exchange of ozone*, edited by I. S. A. Isaksen, D. Reidel, Norwell, Mass., 1988.

Vaughan, G., and C. Timmis, Transport into the troposphere in a tropopause fold, *Quart. J. Roy. Met. Soc.*, *120*, 1085–1103, 1994.

Walmsley, J.L., and J. Mailhot, On the numerical accuracy of trajectory models for long-range transport of atmospheric pollutants, *Atmos.-Ocean*, *21*, 14–39, 1983.

Ward, M.N, Provisionally corrected surface wind data, worldwide ocean-atmosphere surface fields and Sahelian rainfall variability, *J.Climate*, *5*, 454–475, 1992.

Wei, M. Y., A new formulation of the exchange of mass and trace constituents between the stratosphere and troposphere, *J. Atmos. Sci.* , *44*, 3079–3086, 1987.

Wernli, H., and M. Bourqui, A Lagrangian "1-year climatology" of (deep) cross-tropopause exchange in the extratropical Northern Hemisphere, *J. Geophys. Res.*, *107*(D2), doi:10.1029/2001JD000812, 2002.

Wernli, H., and H.C. Davies, A langrangian-based analysis of extratropical cyclones. I: The method and some applications, *Quart. J. Roy. Met. Soc.*, *123*, 467–489, 1997.

Wienhold, F.G., H. Fischer, P. Hoor, V. Wagner, R. Königstedt, G.W. Harris, J. Anders, R. Grisar, M. Knothe, W.J. Riedel, F.J. Lübken, and T. Schilling, TRISTAR - a tracer in situ TDLAS for atmospheric research, *Appl. Phys. B.*, *67*, 411–417, 1998.

Williamson, D. L., and P. J. Rasch, Two-Dimensional Semi-Lagrangian Transport with Shape-Preserving Interpolation, *Mon. Wea. Rev.* , *117*, 102–129, 1989.

Wirth, V., Comments on "A New Formulation of the Exchange of Mass and Trace Constituents between the Stratosphere and Troposphere", *J. Atmos. Sci.* , *52*, 2491–2493, 1995*a*.

Wirth, V., Diabatic heating in an axisymmetric cut-off cyclone and related stratosphere-troposphere exchange, *Quart. J. Roy. Met. Soc.*, *121*, 127–147, 1995*b*.

Wirth, V., and J. Egger, Diagnosing extratropical synoptic-scale stratosphere-troposphere exchange: A case study, *Quart. J. Roy. Met. Soc.*, *125*, 635–655, 1999.

WMO, *A three-dimensional science*, vol. WMO Bull, (Oct), 134–138 pp., World Meteorological Organization, 1957.

WMO, *Atmospheric Ozone 1985: Global ozone research and monitoring report*, vol. WMO No.16, World Meteorological Organization, Geneva,Switzerland, 1986.

WMO, *Scientific Assesment of Ozone Depletion:1994*, vol. WMO No.37, World Meteorological Organization, Geneva,Switzerland, 1995.

Zahn, A., and et al., Identification of extratropical two-way troposphere-stratosphere mixing based on CARIBIC measurements of O3, CO and ultrafine particles, *J. Geophys. Res.*, *105*, 1527–1535, 2000.

Ziereis, H., H. Schlager, P. Schulte, P. van Velthoven, and F. Slemr, Distributions of NO, NOx, and NOy in the upper troposphere and lower stratosphere between 28 and 61°N during POLINAT 2, *J. Geophys. Res.*, *105*, 3653–3664, 2000.

Zierl, B., and V. Wirth, The influence of radiation on tropopause behaviour and stratosphere-troposphere exchange in an upper tropospheric anticyclone, *J. Geophys. Res.*, (102), 1997.